nature chemistry

SUPPLEMENTARY INFORMATION

https://doi.org/10.1038/s41557-019-0251-8

In the format provided by the authors and unedited.

Autonomous dynamic control of DNA nanostructure self-assembly

Leopold N. Green[1,2,9], Hari K. K. Subramanian[3,9], Vahid Mardanlou[4], Jongmin Kim[5,6], Rizal F. Hariadi[7] and Elisa Franco[3,8]*

[1]Bioengineering, University of California, Riverside, CA, USA. [2]Bioengineering, California Institute of Technology, Pasadena, CA, USA. [3]Mechanical Engineering, University of California, Riverside, CA, USA. [4]Electrical and Computer Engineering, University of California, Riverside, CA, USA. [5]Wyss Institute for Biologically Inspired Engineering, Harvard University, Boston, MA, USA. [6]Integrative Biosciences and Biotechnology, Pohang University of Science and Technology, Pohang, Gyeongbuk, Republic of Korea. [7]Department of Physics and the Biodesign Institute, Arizona State University, Tempe, AZ, USA. [8]Present address: Samueli School of Engineering, University of California, Los Angeles, CA, USA. [9]These authors contributed equally: Leopold N. Green, Hari K. K. Subramanian. *e-mail: efranco@seas.ucla.edu

Supplementary Information file
Autonomous dynamic control of DNA nanostructure self-assembly

Leopold N. Green[1,2,†], Hari K. K. Subramanian[3,†], Vahid Mardanlou[4], Jongmin Kim[5,6], Rizal F. Hariadi[5], and Elisa Franco[3,8,*]

[1] *Bioengineering, University of California, Riverside, Riverside, CA, USA*

[2] *Bioengineering, California Institute of Technology, Pasadena, CA, USA*

[3] *Mechanical Engineering, University of California, Riverside, CA, USA*

[4] *Electrical and Computer Engineering, University of California, Riverside, CA, USA*

[5] *Wyss Institute for Biologically Inspired Engineering, Harvard University, Boston, MA, USA*

[6] *Integrative Biosciences and Biotechnology, Pohang University of Science and Technology, Pohang, Gyeongbuk 37673, Republic of Korea*

[7] *Department of Physics and the Biodesign Institute, Arizona State University, Tempe, AZ, USA*

[8] *Present address: Samueli School of Engineering, University of California, Los Angeles, CA, USA*

[*] *To whom correspondence should be addressed; E-mail: efranco@seas.ucla.edu*

[†] *These authors contributed equally*

Contents

1 DNA Sequences

Oligonucleotides were purchased from Integrated DNA Technologies (Coralville, IA, USA). Sequences S1, S2 NoTH, S3 Cy3, S4, and S5, are taken from [19]. DNA sequences for the synthetic oscillator system were taken from [11] (Table 5). All other sequences were designed using Nupack [28] or DNA Design [2].

Tile, invader, and anti-invader sequences:

Name	*Tile with 5-base sticky ends*
S1	5'- CTC AGT GGA CAG CCG TTC TGG AGC GTT GGA CGA AAC T
S2 7bTH	5'-**TGG TAT T**GT CTG GTA GAG CAC CAC TGA GAG GTA
S2 5bTH	5'-**GTA TT**G TCT GGT AGA GCA CCA CTG AGA GGT A
S2 3bTH	5'-**ATT** GTC TGG TAG AGC ACC ACT GAG AGG TA
S2 NoTH	5'-GTC TGG TAG AGC ACC ACT GAG AGG TA
S2 3'-5bTH	5'-GTC TGG TAG AGC ACC ACT GAG AGG TA**T GGT ATT**
S3 Cy3	5'-T Cy3/CCA GAA CGG CTG TGG CTA AAC AGT AAC CGA AGC ACC AAC GCT
S3 Cy5	5'-T Cy5/CCA GAA CGG CTG TGG CTA AAC AGT AAC CGA AGC ACC AAC GCT
S4	5'- CAG ACA GTT TCG TGG TCA TCG TAC CT
S5	5'-CGA TGA CCT GCT TCG GTT ACT GTT TAG CCT GCT CTA C
Invader 7bTH	5'- ACC AGA CAA TAC CAA TCC GC
Truncated Invader 7bTH	5- AATACCATTT/3Bio/
Anti-Invader 7bTH	5'- GCG GAT TGG TAT TGT CTG GT
Invader 3'-7bTH	5'- GTC CGC AAT ACC ATA CCT CT
Anti-Invader 3'-7bTH	5'- AGA GGT ATG GTA TTG CGG AC

Table 1: *Sequences for tiles with 5-base long sticky ends, invaders, anti-invaders, and all their variants. Bold sequences indicate toehold domains. Expected secondary structures and interactions among tiles, invaders, and anti-invaders are shown in Figs. 1 A1-A4, 2, 3 A, 4 A and 5.*

Name	*Tile with 7-base sticky ends*
7b S1	5'- TCA GTG GAC AGC CGT TCT GGA GCG TTG GAC GAA AC
7b S2	5'- **TGG TAT TT**G TCT GGT AGA GCA CCA CTG AGA GGT AC
7b S3	5'- T Cy3/CCA GAA CGG CTG TGG CTA AAC AGT AAC CGA AGC ACC AAC GCT
7b S4	5'- CCA GAC AGT TTC GTG GTC ATC GTA CCT C
7b S5	5'- GAT GAC CTG CTT CGG TTA CTG TTT AGC CTG CTC TA
7b Invader	5'- CCA GAC AAA TAC CAA TCC GC
7b Anti-Invader	5'- GCG GAT TGG TAT TTG TCT GG

Table 2: *Sequences for tiles with 7-base long sticky ends, invaders and anti-invaders. Bold sequences indicate toehold domains. Strand interactions are shown in Fig. 1 B, 2 B, 3 B, and 4 B.*

Name	*Tile with 8-base sticky ends*
8b S1	5'- AGT GGA CAG CCG TTC TGG AGC GTT GGA CGA AAC T
8b S2	5'- **TGT AAT A**TC GTG CCC GAG CAC CAC TGA GAG GTA
8b S3	5'-T Cy3/CCA GAA CGG CTG TGG CTA AAC AGT AAC CGA AGC ACC AAC GCT
8b S4	5'- GGG CAC GAA GTT TCG TGG TCA TCG TAC CTC TC
8b S5	5'- CGA TGA CCT GCT TCG GTT ACT GTT TAG CCT GCT C
8b SE4-TAMRA	5-TAMRA-GGGCACGAAGTTTCGTGGTCATCGTACCTCTC
8b SE3-NoDye	5- CCAGAACGGCTGTGGCTAAACAGTAACCGAAGCACCAACGCT
8b Invader	5'- GGG CAC GAT ATT ACA CTA AGG
8B Anti-Invader	5'- CCT TAG TGT AAT ATC GTG CCC

Table 3: *Sequences for tiles with 8-base long sticky ends, invaders and anti-invaders. Bold sequences indicate toehold domains. Strand interactions are shown in Fig. 1 C, 2 C, 3 C, and 4 C. Variants 8b SE4-TAMRA and 8b SE3-NoDye were used exclusively in oscillator experiments R3.*

Name	*Insulator system producing invader for 8-base sticky end tile*
8b Ins-nt	5'- CAT TAG TGT CGT TCG TTC ACA GTA ATA CGA CTC ACT ATA GGG CAC GAT ATT ACA CTA AGG AGT GAC AAA GTC ACA AA
8b Ins-t	5'- TTT GTG ACT TTG TCA CTC CTT AGT GTA ATA TCG TGC CCT ATA GTG AGT CG
RNA invader	GGG CAC GAU AUU ACA CUA AGG AGU GAC AAA GUC ACA AA
dI1	5'-GTG TGT AGT AGT AGT TCA TTA GTG TCG TTC GTT CAC AG
A1	5'-TAT TAC TGT GAA CGA ACG ACA CTA ATG AAC TAC TAC

Table 4: *DNA sequences for the insulator gene used to couple oscillator and nanotubes, together with its activator and inhibitor (which are the same as for switch 21 of the oscillator). The genelet includes a 3' end hairpin sequence to reduce transcription elongation; thus, the RNA invader includes a hairpin sequence (underlined). Fig. 6 shows the interactions among insulator components (activation and inhibition), production of RNA invader, invasion of tiles and RNase H-mediated reactivation of tiles.*

Name	*Oscillator*
T12-t	5'- TTT CTG ACT TTG TCA GTA TTA GTG TGT AGT AGT AGT TCA TTA GTG TCG TTC GTT CTT TGT TTC TCC CTA TAG TGA GTC G
T12-nt	5'-AAG CAA GGG TAA GAT GGA ATG ATA ATA CGA CTC ACT ATA GGG AGA AAC AAA GAA CGA ACG ACA CTA ATG AAC TAC TAC TAC ACA CTA ATA CTG ACA AAG TCA GAA A
T21-t	5'-TTT CTG ACT TTG TCA GTA TTA TCA TTC CAT CTT ACC CTT GCT TCA ATC CGT TTT ACT CTC CCT ATA GTG AGT CG
T21-nt	5'-Tye665/CAT TAG TGT CGT TCG TTC ACA GTA ATA CGA CTC ACT ATA GGG AGA GTA AAA CGG ATT GAA GCA AGG GTA AGA TGG AAT GAT AAT ACT GAC AAA GTC AGA AA
dI1	5'-GTG TGT AGT AGT AGT TCA TTA GTG TCG TTC GTT CAC AG
A1	5'-TAT TAC TGT GAA CGA ACG ACA CTA ATG AAC TAC TAC
A2	5'-TAT TAT CAT TCC ATC TTA CCC TTG CTT CAA TCC GT

Table 5: *DNA sequences for oscillator used to control the growth and decay of DNA nanotubes. Sequences are taken from [11, 6]. Gene sequences include a 3' end hairpin domain to reduce transcription elongation. Target strand interactions are shown in Fig. 8 and 9; a schematic of the oscillator reactions is shown in Fig. 7.*

2 Expected secondary structure and reaction schemes

2.1 DAE-E Tiles and nanotubes

2.1.1 Tile variants with external toehold

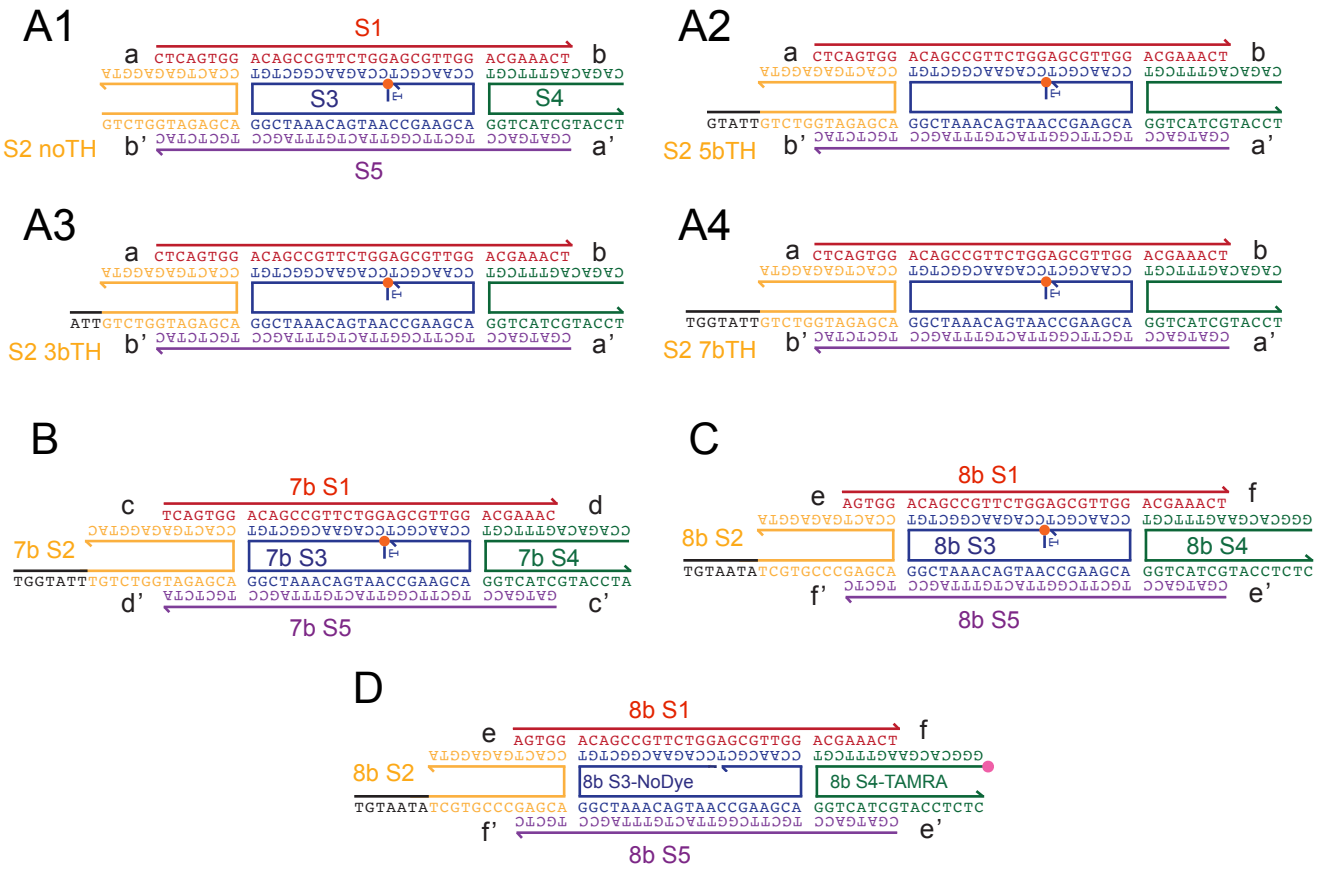

Figure 1: Tile variants with external toehold *A1-A4: Strand interactions in tiles with 5 base-long sticky ends. B: Tile with 7 base-long sticky ends. C: Tile with 8-base long sticky ends. D: Tile variant used in Round 3 of the oscillator experiments.*

2.2 Invasion reaction

Fig. 2 illustrates the interaction of an invader strand binding to the toehold and displacing the sticky end of two hybridized tiles. (1) The example two-tile complex contains a free toehold region indicated by the black overhang domain of the complex. (2) The complementary domain of the free invader strand initiates tile displacement by interacting with the free toehold region of the tile-tile complex. (3) The invader strand completes hybridization with the toeholded sticky end of the tile. To be stable, inter-tile bonds require cooperative binding of both sticky ends; thus the second sticky end is expected to unbind. This process causes nanotubes to disassemble.

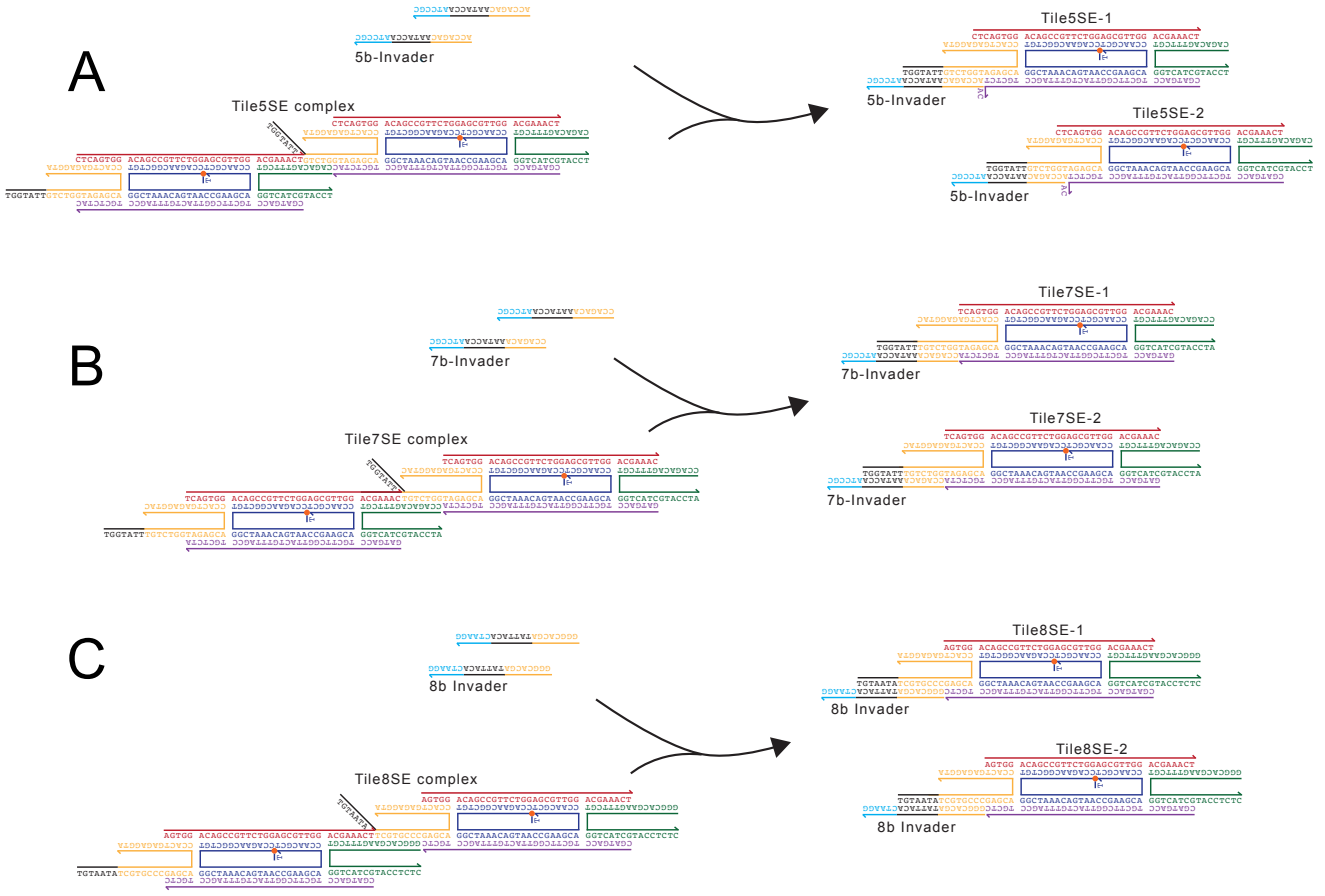

Figure 2: Illustration of invasion reaction *A: Invasion in 5 base-long sticky end tiles. B: Invasion in 7 base-long sticky end tiles. C: Invasion in 8 base-long sticky end tiles.*

2.3 Anti-invasion reaction

The mechanism of tube invasion has been designed to be reversible: by including a toehold on the invader strand, it is possible to displace it from tiles using a complementary anti-invader strand. By displacing and titrating the invader, the anti-invader restores the ability of tiles to nucleate and polymerize. This reaction is shown in Fig. 3 using two invaded tiles; displacement of the invader promotes inter-tile bond formation. (Stable bonds are formed only when both sticky ends bind to a nucleated site or growing lattice/tube)

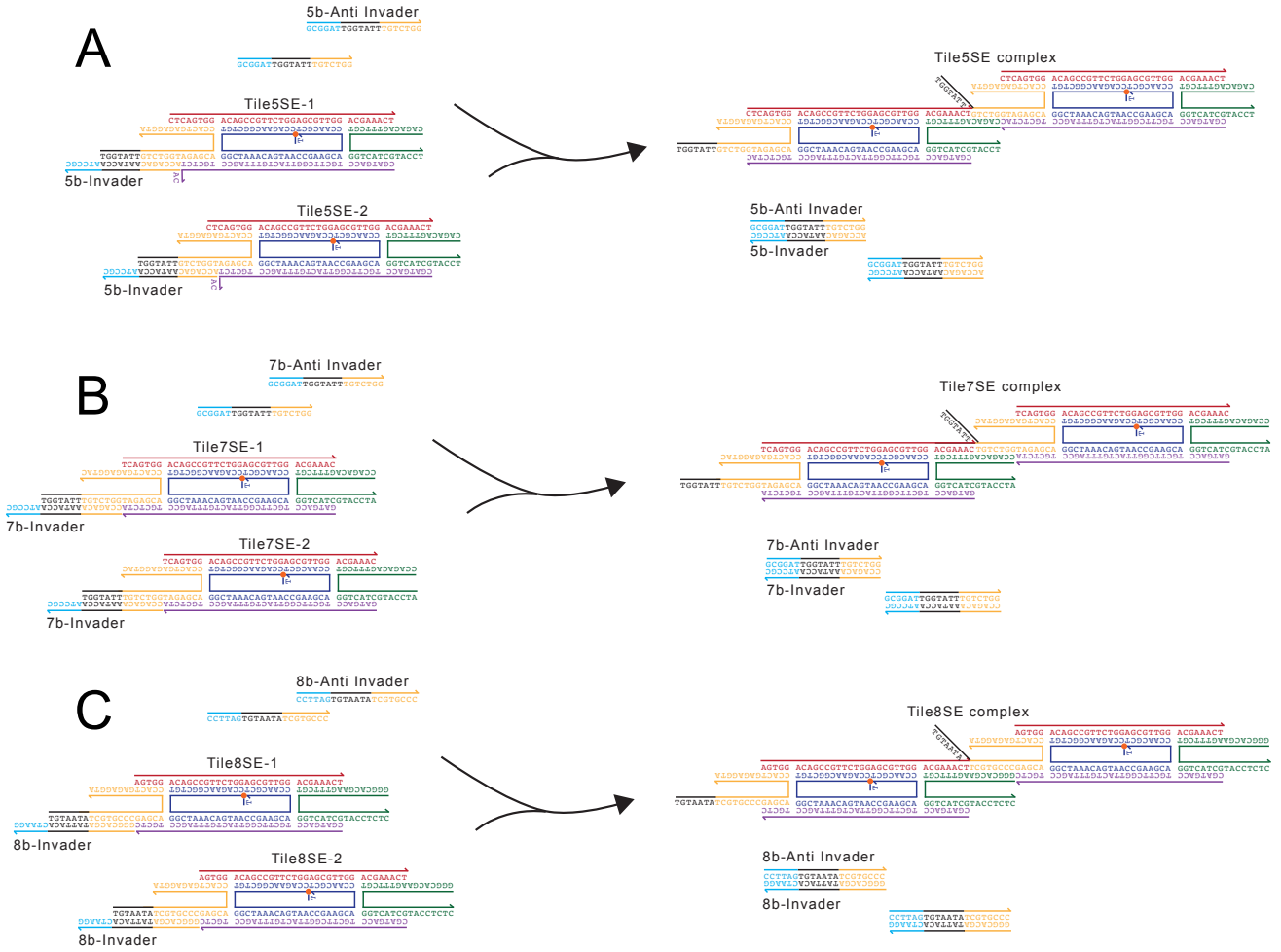

Figure 3: Illustration of anti-invasion reaction *A: Anti-invasion in 5 base-long sticky end tiles. B: Anti-invasion in 7 base-long sticky end tiles. C: Anti-invasion in 8 base-long sticky end tiles.*

2.3.1 Side reactions

The anti-invader strand is complementary to one of the sticky end domains in strand S4. This undesirable bond is presumably weak in 5 base-long sticky ends but is expected to be more stable in 7 and 8 base-long sticky end tiles. It is plausible that this interaction may contribute to the creation of a population of partially inactive tiles, and reduce nanotube polymerization rate; this hypothesis seems to be validated by experimental results on anti-invasion of 8 base-long sticky end tiles shown in Fig. 36.

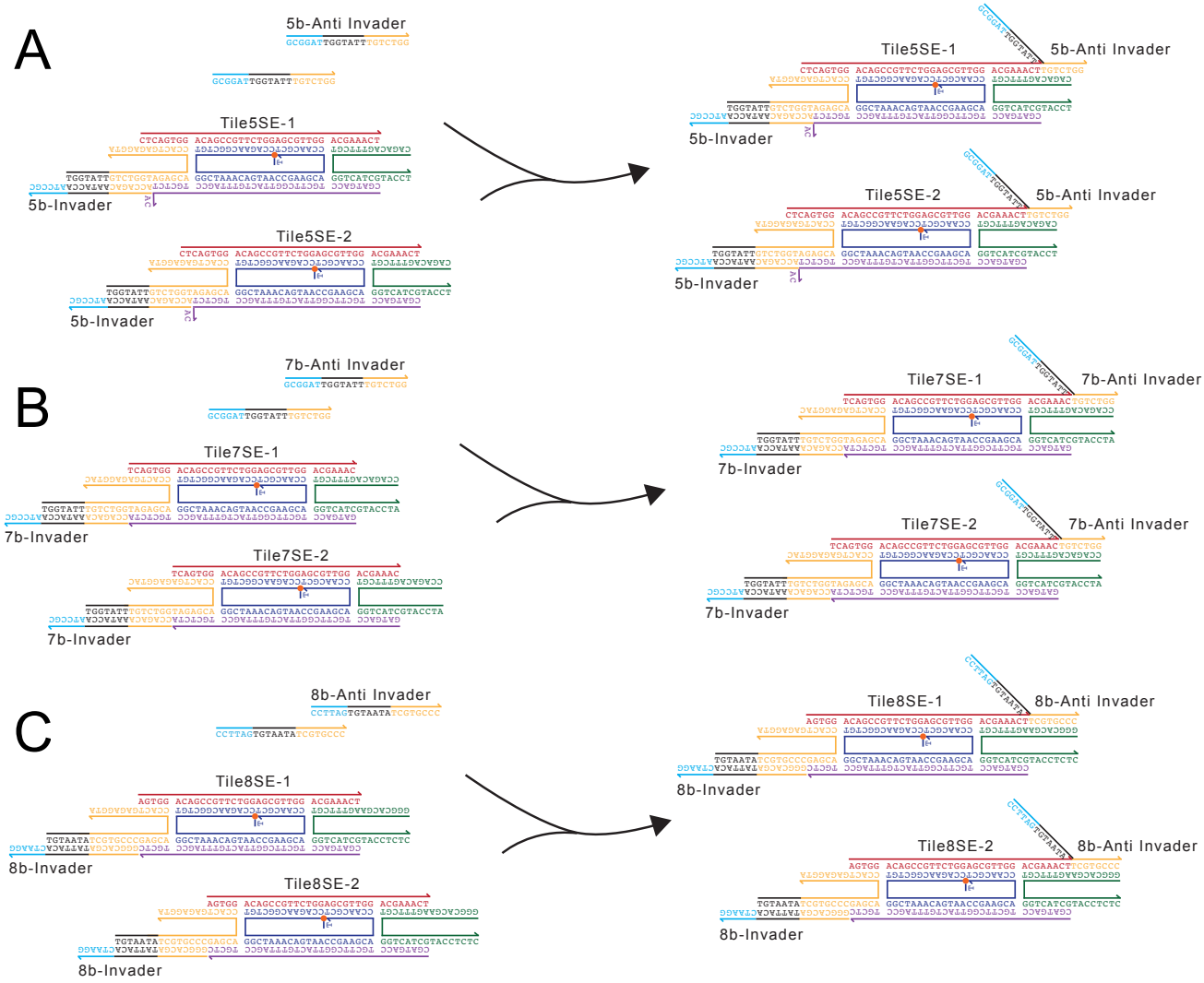

Figure 4: Anti-invader can bind to strand S4 *A: Interaction in 5 base-long sticky end tiles is limited to 5 bases, and is therefore likely unstable. B: Interaction in 7 base-long sticky end tiles. C: Interaction in 8 base-long sticky end tiles.*

2.4 Comparison of tiles assembling into nanotubes with external or internal toehold

Tiles can be designed with a toehold that is exposed externally or internally (Fig. 5). This is possible because depending on the number of bases separating the location of the toehold and the crossover point, one could predict the angle at which the toehold exits the tile plane. This, in turn, tells us the side of the tile/lattice in which toeholds will exit. Toeholds exposed internally are located at the 3' end of strand S2, and are expected to be accessible mainly at the nanotube ends, thus allowing invasion reactions to be localized primarily at the ends. In contrast, external toeholds promote disassembly that is distributed throughout the nanotube (Fig. 5 C). Control experiments verifying that toehold position determines whether it protrudes externally or internally are in Section 4.2.

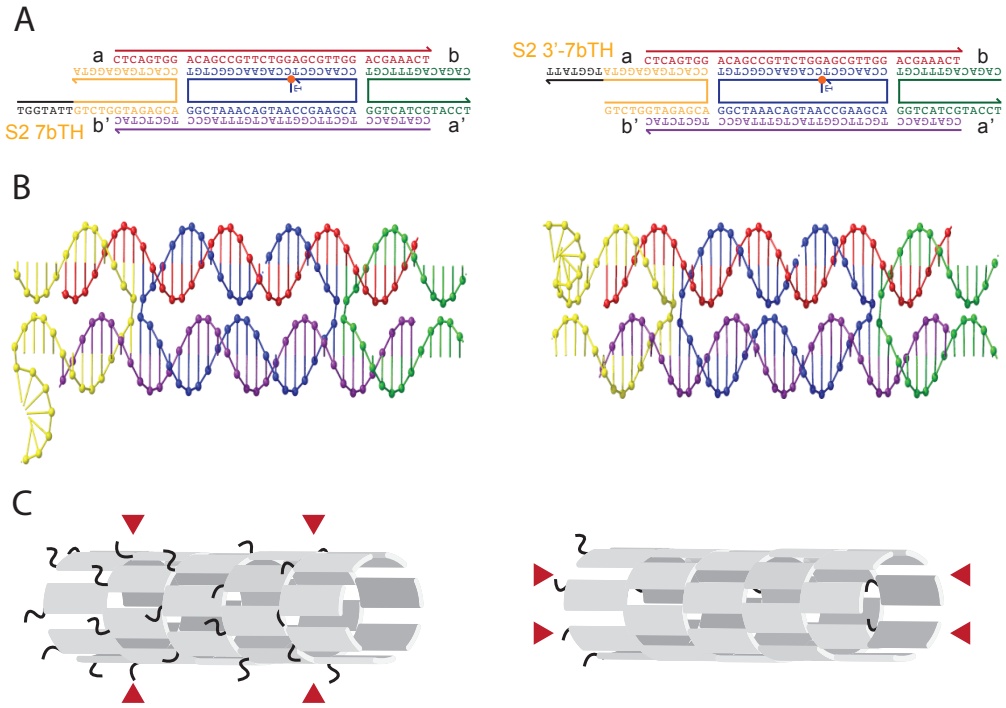

Figure 5: Tiles resulting in nanotubes with external and internal toehold *These tiles have 5 base-long sticky ends. A - Left: To obtain a nanotube with toeholds facing the external surface of the nanotube, we located the toehold on the 5' end of strand S2. Right: Nanotubes with internal toehold can be obtained by placing the toehold on the 3' end of strand S2. B: Rendering of the tiles obtained with the 3D CAD software and molecular modeling program Nanoengineer [1]. C: Nanotubes with external toehold can be invaded at all points on the lattice where the toehold is exposed; in contrast, nanotubes with internal toeholds can be invaded primarily at the ends. Example time-lapse movies supporting our expectation are available online.*

2.5 Reactions for transcriptional control of nanotube breakage and reassembly

We designed a synthetic gene to transcribe RNA invader. Transcription is operated by T7 RNA polymerase. To modulate the invader transcription rate, the gene can be activated or repressed by strand displacement of a portion of its template strand, which includes the T7 promoter region [6].

We use RNase H to reverse the breakage process driven by the RNA invader binding to the tiles. RNase H degrades RNA in an RNA-DNA duplex, restoring the ability of tiles to nucleate and assemble.

Fig. 6 A illustrates the reactions of invader transcription by T7 RNAP and the mechanism of inhibition of the genelet. Fig. 6 B is a schematic of tile invasion via RNA invader. Fig. 6 C illustrates RNase H-mediated degradation of invader which promotes reassembly.

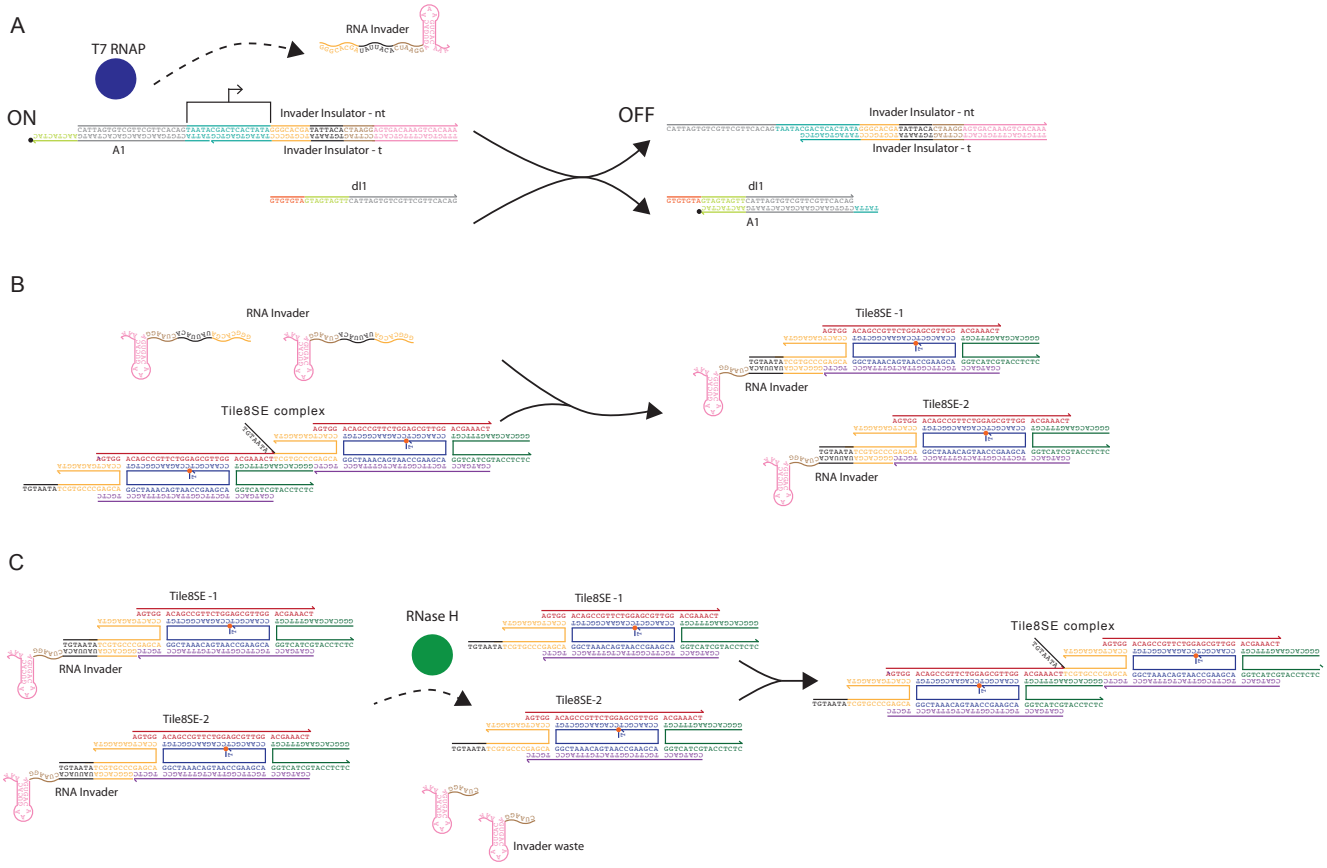

Figure 6: Enzyme-driven invasion and anti-invasion reactions *A: A synthetic gene (Invader Insulator) is used to transcribe the species RNA invader. The gene can be turned off by displacement of the activator strand A1 [11] using an inhibitor strand dI1. (Species A1 and dI1 are the same used in the transcriptional oscillator described in Section 2.6, Figs. 8 and 9). B: Invasion reaction mediated by the RNA invader. C: RNA invader bound to tiles is degraded by RNase H, which results in the release of the sticky end domain. Tiles can therefore reassemble.*

2.6 Reactions designed to direct tube breakage and reassembly using an autonomous molecular oscillator

For the readers' convenience we report detailed strand interactions for the oscillator system used to direct nanotube assembly and disassembly; figures 7, 8 and 9 are adapted from [11, 6, 25]. Fig. 10 summarizes the architecture used to interconnect the oscillator and the nanotubes, which builds on results obtained in [6]. This is done using an insulating gene, which decouples the sequences of the

insulator and the sequence of the RNA invader, and additionally reduces consumption of oscillator components (RNA transcription works as an amplification mechanism). This architecture, however, cannot mitigate consumption of RNase H, which degrades RNA invader bound to the tiles, creating an additional load on the oscillator system. To compensate for this consumption, the oscillator was tuned in a regime where RNase H is abundant; this topic is discussed further in Section 4.13.

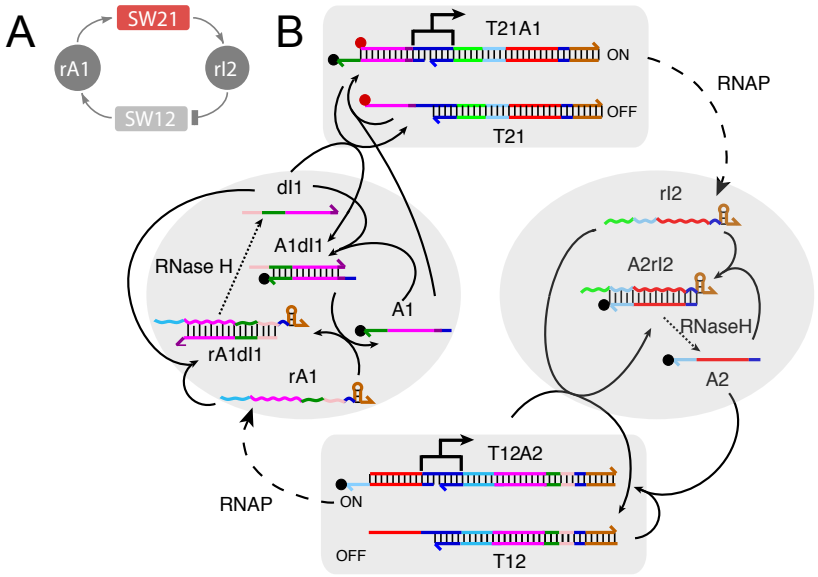

Figure 7: Topology of the oscillator and its biochemical reactions. *A: Topology of the synthetic molecular oscillator used in our experiments: two artificial genetic switches (SW12 and SW21) are mutually interconnected through their RNA transcripts (rA1 and rI2) forming a negative feedback loop. B: Reactions occurring in the system. Functionally distinct domains (toeholds, regulatory domains, spacers, promoter and hairpin regions) are colored consistently with strand schematics in Figs. 8 and 9. Red and black dots on gene T21 and activator A1 are fluorophore-quencher pairs used as reporters on the active/inactive state of the switch. Solid arrows indicate reactions between oligonucleotides; dashed arrows indicate enzymatic reactions (transcription and degradation). Figure is adapted from [11, 6, 25].*

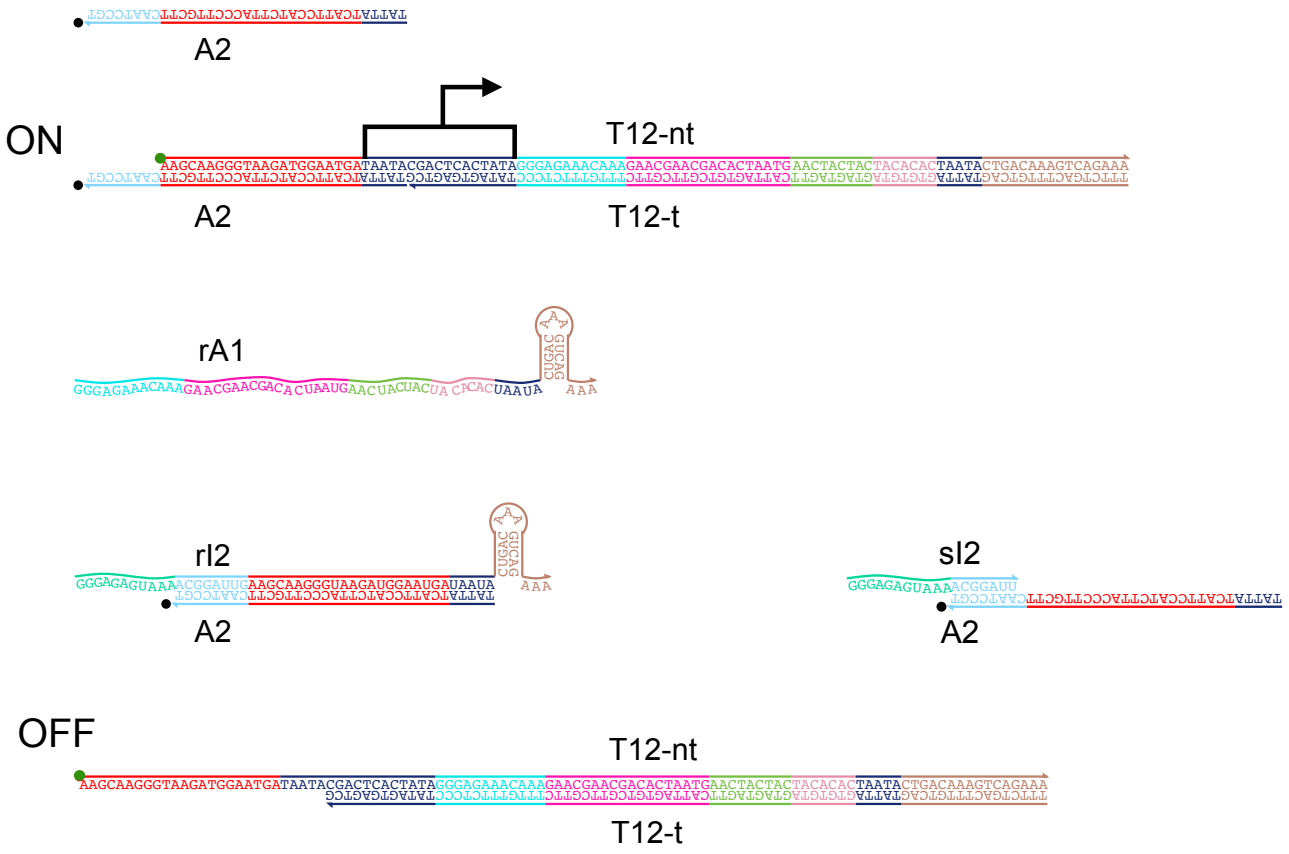

Figure 8: Switch 12 strands and their domain interactions. *This figures shows strands components of SW12 and their interactions, with functional domains in different colors. The mathematical model of the oscillator includes all complexes shown in this figure, including complex sI2·A2 which is the result of interactions between A2 and products of incomplete degradation of RNase H which can reach up to 7 bases [11, 18].*

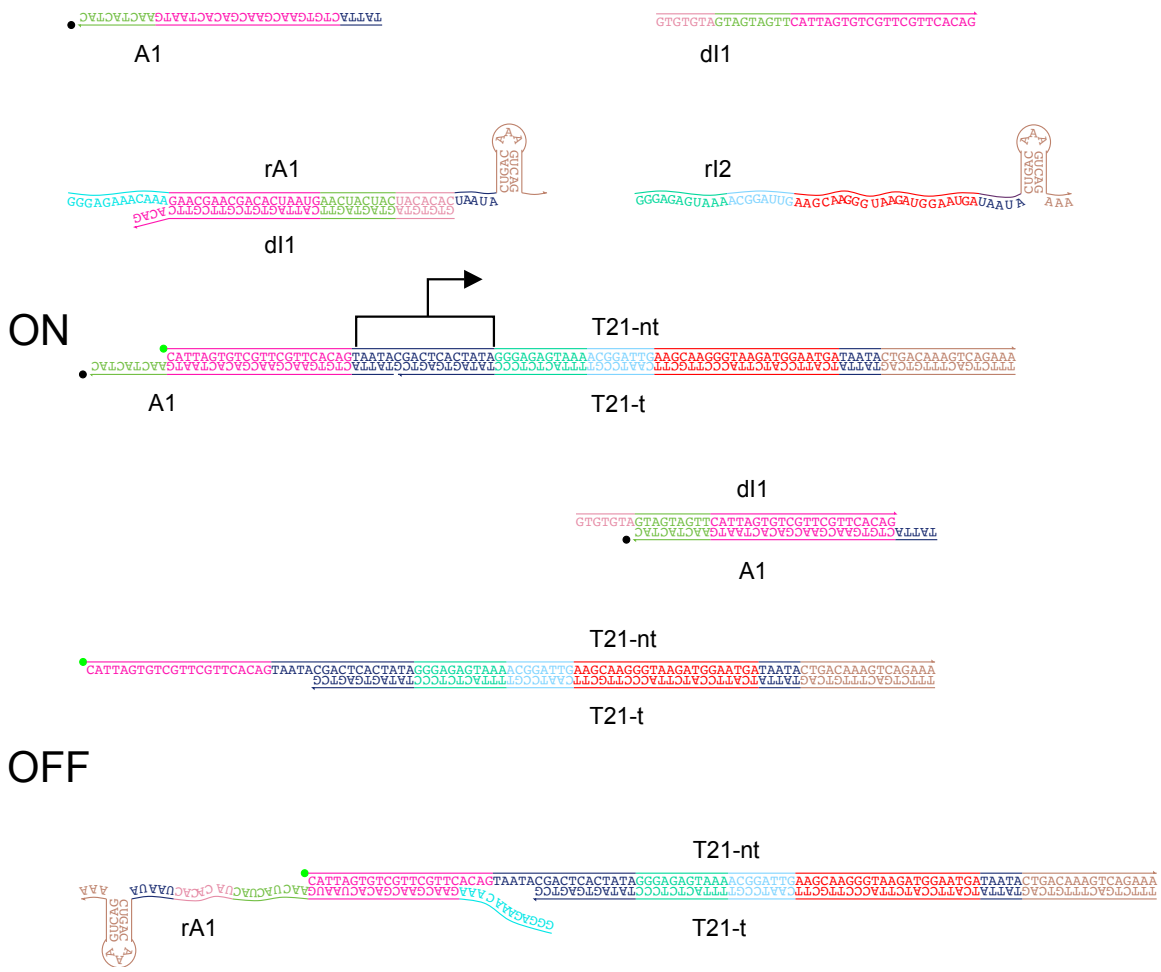

Figure 9: Switch 21 strands and their domain interactions. *As Fig. 8, we show sequences for SW21 with functional domains in different colors. The mathematical model of the oscillator includes all complexes shown in this figure.*

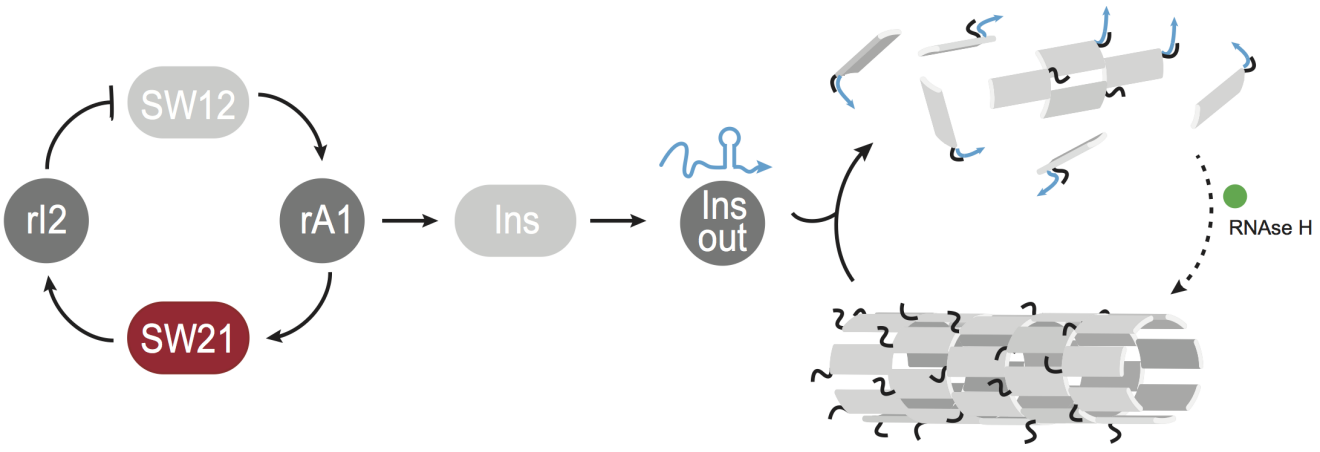

Figure 10: The oscillator was used to direct nanotube assembly and disassembly using an insulator gene. *This scheme summarizes the topology of interconnection of the oscillator and the nanotubes. The insulator gene (Fig. 6) was designed to be activated and inactivated by strands A1 and dI1 of the oscillator, and its transcript is an RNA invader. Tile reactivation is promoted by RNase H degradation. Strands and reactions for the transcriptional insulator, invasion, and RNase H anti-invasion are shown in Fig. 6.*

3 Methods

3.1 Sample preparation

Lyophilized DNA oligonucleotides were purchased from Integrated DNA Technologies (Coralville, IA), resuspended in water, quantitated by UV absorbance at 260 nm using a Thermo Scientific Nanodrop 2000c Spectrophotometer, and stored at -20°C. All samples were stored or mixed using DNA Lo-bind tubes (# 022431021).

Nanotubes were annealed at either 1 or 5 μM tile concentration by mixing each tile strand at 1 or 5 μM (final concentration), in either of the following buffer mixes: 1) Tris-Acetate-EDTA (TAE) and 12.4mM $MgCl_2$, or 2) 1X transcription buffer (New England Biolabs, #B9012S). Nanopure water was added to achieve the appropriate concentration of components. Nanotubes were annealed using an Eppendorf Mastercycler PCR machine by heating the sample to 90°C, and cooling it to 25°C over a 6 hour period.

The position of the toehold in nanotubes was characterized by binding of streptavidin to the toeholds. Streptavidin-cy3 was purchased from Biolegend (Cat# 405215). A biotinylated strand (Truncated Invader 5'T, Table 1) was used to bridge streptavidin to the 5 base sticky end nanotubes.

Genelets for transcriptional control of nanotube assembly were individually annealed in 1x transcription buffer (New England Biolabs, #B9012S) using an Eppendorf Mastercycler PCR machine by heating the sample to 90°C, and cooling it to 25°C over a 1.5 hour period.

3.2 Transcription

Transcription mix was prepared mixing reagents for the following overall final concentrations: 1x transcription buffer (New England Biolabs, #B9012S), 5.5 mM each rNTP (Epicentre Biotechnologies, Cat. n. RN02825), 30 mM $MgCl_2$ and 0.015 U/μL yeast inorganic pyrophosphatase (New England Biolabs, #M2403L).

T7 RNAP was purchased from Cellscript (200 U/μL, # C-T7300K). RNase H was purchased from Thermofisher (Cat. n. EN0202) or Promega (Cat. n. M4285), which was used only for experiment round 3 with the oscillator.

3.3 Fluorescence microscopy

Nanotube samples were imaged using an inverted microscope (Nikon Eclipse TI-E) with 60X/1.40 NA oil immersion objectives. Samples containing nanotubes were imaged at 50 nM tile concentration in corresponding experimental buffer conditions (either 1x TAE and 12.4mM $MgCl_2$, or 1x transcription buffer). Samples were placed on Fischerbrand microscope cover glass (# 12-545E No. 1, thickness=0.13 to 0.17mm; size: 50 x 22mm); VWR Micro Slides (Plain, Selected, Pre-cleaned, 25 x 75 mm, 1.0mm thick, # 48300-025) were placed gently on the cover glass. Nanotubes labeled with Cy3 fluorescent molecule were imaged using Cy3 filter cube (Semrock Brightline - Cy3-404C-NTE-ZERO). Exposure time was set to 90ms.

3.4 Fluorescence microscopy data processing

Fluorescence microscopy images were processed using ImageJ plugin Skeletonize to collect nanotube length distributions. Branching or looping nanotubes were eliminated from the length dataset using an in-house MATLAB script. Pixels were converted to μm using conversion factor 1 pixel = 0.11 μm. Due to camera resolution limitations, tubes lengths less than 0.33 μm were also eliminated from tube length distributions.

Nanotube length distributions measured in fluorescence microscopy experiments are shown as violin plots in Section 4. These plots were prepared using `distributionPlot`, a MATLAB File Exchange

script; in each violin plot, length data are plotted as a histogram normalized individually to have a maximum width of 0.8.

3.5 Atomic Force Microscopy

AFM images were obtained in tapping mode with a Digital Instruments Multimode AFM, equipped with a Nanoscope III controller. Sharp Nitride Lever (SNL) tips from Bruker with a nominal spring constant of 0.24 N/m were used for imaging, with a drive frequency of 9-10 kHz. Samples were imaged using 1X TAE and 12.5 mM $MgCl_2$ buffer.

3.6 Gel electrophoresis

A 0.5% high-melt agarose gel (made using Bio-Rad Certified Megabase Agarose, #1613108) was prepared in 1x TBE and 12.4 mM $MgCl_2$ by heating 0.5 g of Agarose in 100 mL of the buffer. Once the agarose was fully dissolved, the mixture was allowed to cool and before the mixture solidified, it was poured into the gel cast (Owl Easycast B1 gel system, 9 x 11 cm -Thermo Scientific). DNA nanotubes, labeled with Cy3, at 1 μM tile concentration, and 2 μL total volume were loaded into the wells of the agarose gel. The samples were loaded with Bromophenol blue as a tracking dye. The gel wells were sealed using thin films of solid agarose affixed on top of the wells using molten agarose, to reduce the loss of nanotubes that stay in the wells till the end of the run. The gel was run at room temperature using an Owl Easycast B1 gel system (9 x 11 cm -Thermo Scientific) at 60 V for 3.5 hours. Gel images were taken using a BioRad ChemiDoc MP gel imaging system with a Cy3 filter.

3.7 Bulk fluorimetry

Bulk fluorescence experiments were performed using a Horiba Jobin Yvon Fluorlog 3 spectrofluorimeter. Samples were placed in 60 μL quartz cuvettes purchased from Starna (#16.45F-Q-3/Z15), and incubated in the sample chamber at 37°C. The desired temperature was maintained using a water bath thermostat. To avoid evaporation, the sample was covered with 50 μL of hexadecane (MP Biomedical, LLC # 0219521880). Fluorescence emission of reporters was measured over three separate experiments and averaged accordingly.

In experiments including the molecular oscillator, excitation/emission for dye TYE665 (strand T21, Table 5) were set at 645 nm/665 nm according to the recommendation of the supplier IDT DNA.

In fluorimetry experiments involving TAMRA-labeled 8 base sticky end tiles, excitation/emission for TAMRA was set to 559 nm/583 nm according to the recommendation of the supplier IDT DNA.

3.8 Bulk fluorimetry data processing

Fluorescence measurements on the oscillator (Section 4.13), which track the on/off state of fluorescently labeled synthetic genes over time, were normalized and converted to concentrations using the following general formula:

$$C(t) = C_{tot}\frac{F(t) - F_{\min}}{F_{\max} - F_{\min}},$$

where $C(t)$ is the concentration at time sample t, C_{tot} is the (nominal) total concentration of the component being tracked, $F(t)$ is the recorded fluorescence, and $F_{\min}$ and $F_{\max}$ are respectively minimum and maximum fluorescence values corresponding to fully quenched or free labeled strand. For instance, $F_{\min}$ is the fluorescence of a fully quenched genelet when its quencher-carrying activator is bound to the promoter (active), while $F_{\max}$ is the fluorescence of the gene when no activator is present (inactive). The ratio $R = F_{\min}/F_{\max}$ should be independent of specific strand concentration and lamp intensity. However, $F_{\min}$ and $F_{\max}$ in some cases were not available simultaneously, therefore

the normalization above was done as:

$$C(t) = C_{tot}\frac{F(t)/F_{\max} - R}{1 - R},$$

and R was measured in separate experiments off line, from a calibration sample reproducing the buffer mix conditions of the experiment to be normalized. For the oscillator switch SW21, the signal of the reporter dye is directly proportional to the concentration of inactive switch. We therefore further processed the oscillator switch SW21 reporter signal to represent the *active* state of the switch:

$$C_{active}(t) = C_{tot} - C(t).$$

Fluorescence measurements of nanotube invasion and anti-invasion reactions (Section 4.11.3) were normalized using the fluorescence measured in a control sample including only free monomers (partially blunt ended tiles which cannot polymerize) as the maximum achievable fluorescence F_{max}. Since there could be bleaching of the fluorophore over long periods of time, the average fluorescence value of first one hour in the control sample was assumed as the maximum achievable value. The normalized fluorescence was thus computed as:

$$F_N(t) = F(t)\frac{100}{F_{max}}.$$

3.9 Time-lapse videos of nanotubes invasion and anti-invasion

Time-lapse videos of assembly and disassembly of nanotubes were captured using an inverted fluorescence microscope (Nikon Eclipse TI-E) with a 60X/1.40 NA oil immersion objectives. In general, 20 μL of annealed Cy3-labeled nanotube sample (50 nM, diluted by 20-fold from the annealed sample) in 1x TAE/12.5 mM $MgCl_2$ was first mixed with equal volume of methyl cellulose (0.6% w/v in 1x TAE/12.5 mM MgCl2) and loaded on to capillary (Vitrotubes; # 3520) for imaging. Bovine Serum Albumin (BSA) was added to all samples to a final concentration of 1 mg/mL. For invasion reaction, just before the addition of methyl cellulose, 3 μL (1 μM) invader strand was added to the tube sample and mixed. For anti-invasion reaction sample, 3 μL (1 μM) invader strand was added to 20 μL of annealed nanotube sample was let to sit at room temperature for 6 minutes, then 6 μL (10 μM) anti-invader was added, mixed. After this equal volume of methyl cellulose (0.6% w/v in 1x TAE/12.5 mM MgCl2) was added. The nanotube-methyl cellulose mix was then loaded into a capillary, which was affixed to VWR Micro Slides (Plain, Selected, Pre-cleaned, 25 x 75 mm, 1.0 mm thick) using scotch tape. After loading the sample, the ends of the capillary were sealed using small amounts of petroleum jelly. The sample was placed on the microscope in such a way that the capillary side would be facing the objective. The best imaging region is close to the surface of the capillary, near the objective, where tubes are pushed close to the surface. Time-lapse videos were captured using the proprietary Nikon Imaging software (Nikon Elements 4.12) at the rate 1 frame per 30 seconds. The exposure time for each frame was 200 ms.

4 Overview of experimental results

4.1 Nanotube growth is not significantly affected by the presence of external toehold domain

The addition of a 7 base toehold in strand S2 of 5 base sticky end tiles (Fig. 1 A4) does not affect the growth pattern of assembling nanotubes. The measured mean length is consistent with results published by [4]. Nanotube growth was tested as a function of the toeholded tile percentage, defined as the relative concentration of toeholded S2 strand and non-toeholded S2 strand in the annealing mix. We measured growth in three different assays: 1) tiles without toeholded S2 strand, 2) 50% and 3) 100% concentration of toeholded S2 strand. Length was measured at room temperature (25°C) using fluorescence microscopy (Methods Section 3.3) after a 6 hour anneal (Methods Section 3.1). Each assay was conducted with triplicate experiments. Nanotube length violin plots for each assay, together with the resulting mean and standard deviation of the mean are shown in Figures 11, 12 and 13. Means for the three different assays are compared in Figure 14.

4.1.1 Growth of nanotubes in the absence of toeholded tiles

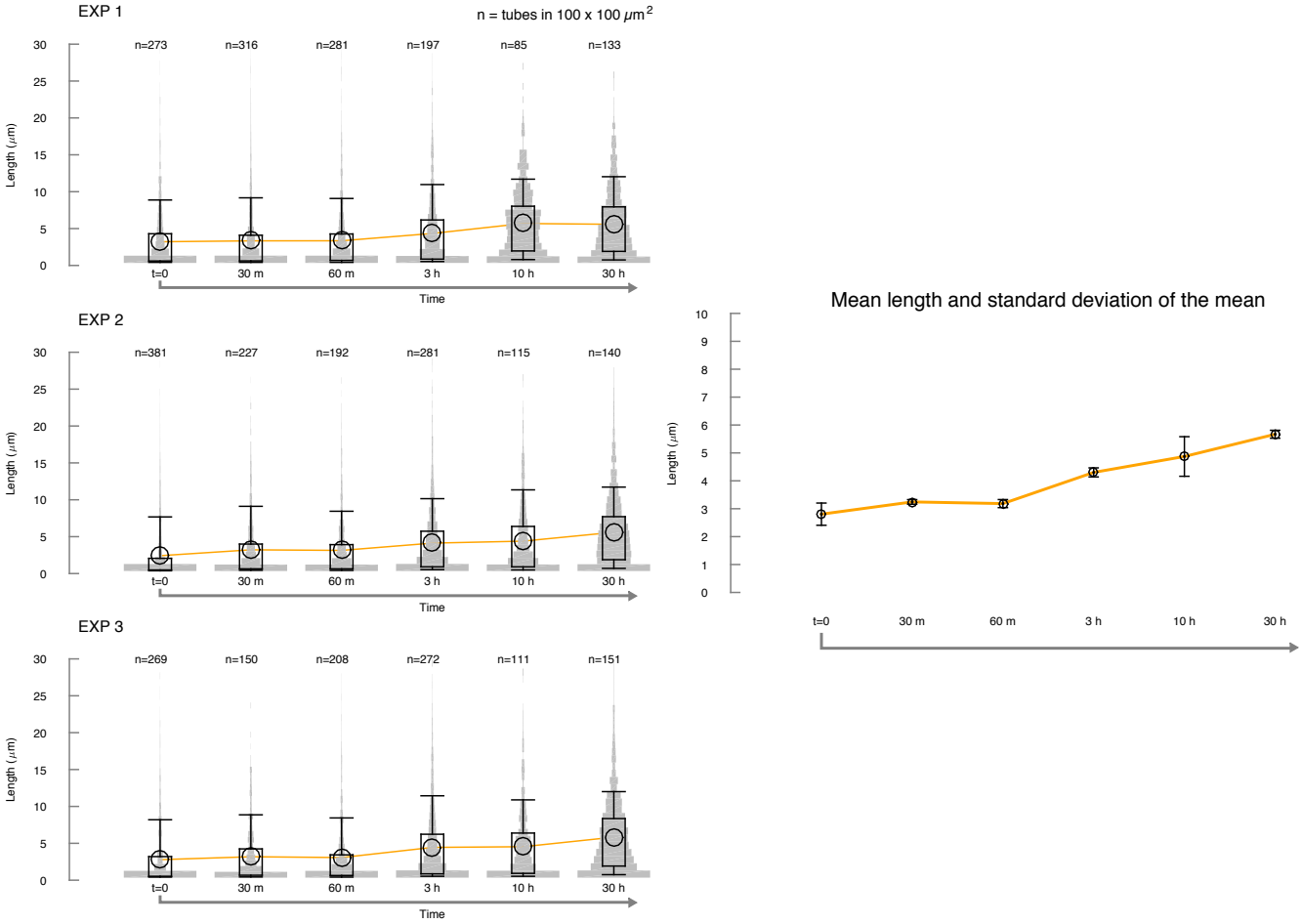

Figure 11: Growth of nanotubes in the absence of toehold domain *Nanotube length was measured over 30 hours (after annealing) from fluorescence microscopy images. Left: Violin plots of each experiment repeat. Right: mean and standard deviation of the mean of length over the three experiments to the left.*

4.1.2 Growth of nanotubes with 50% toeholded tiles

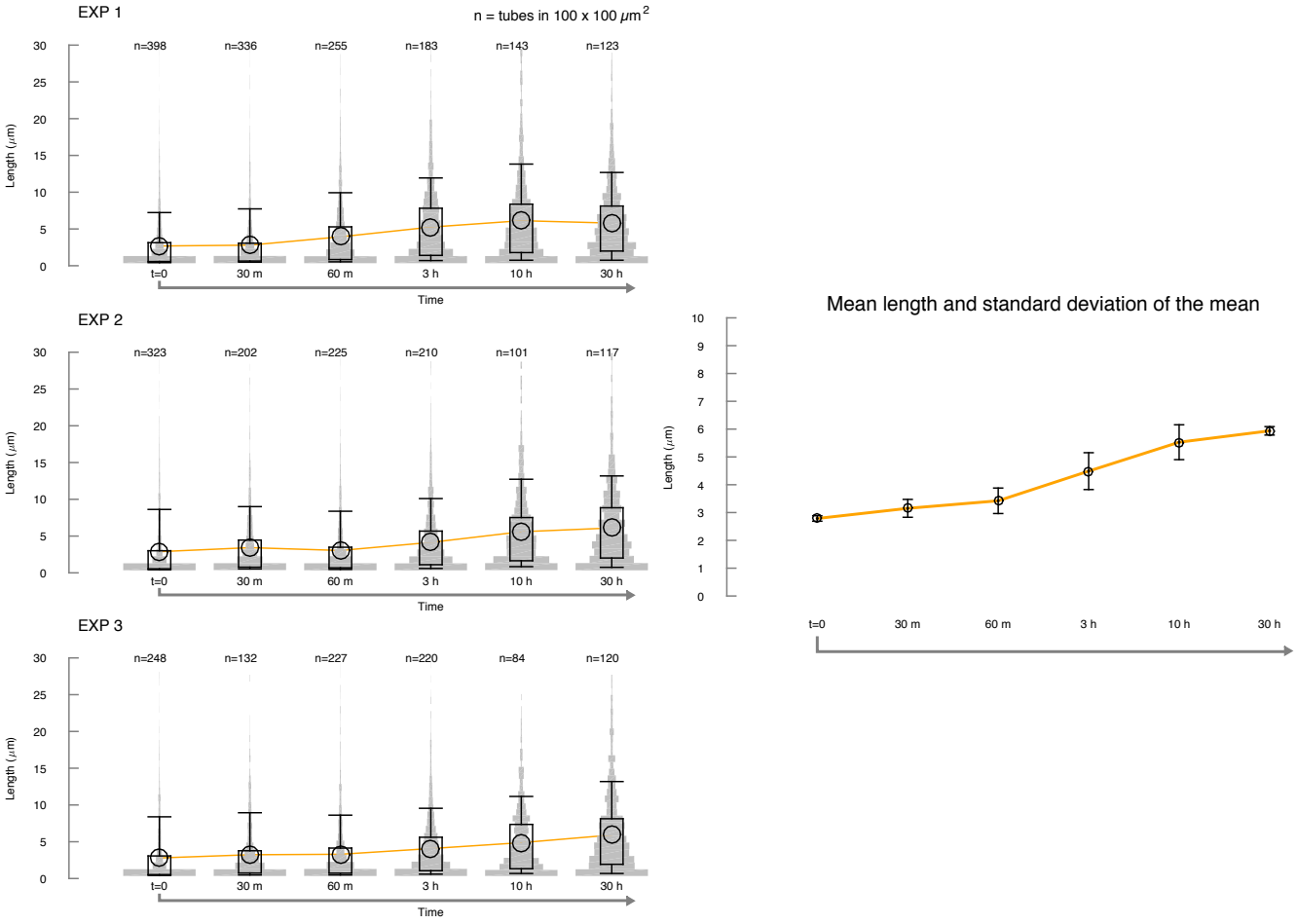

Figure 12: Growth of nanotubes annealed from tile sample where 50% of tiles include a toehold domain *Nanotube length was measured over 30 hours (after annealing) from fluorescence microscopy images. Left: Violin plots of each experiment repeat. Right: mean and standard deviation of the mean of length over the three experiments to the left.*

4.1.3 Growth of nanotubes with 100% toeholded tiles

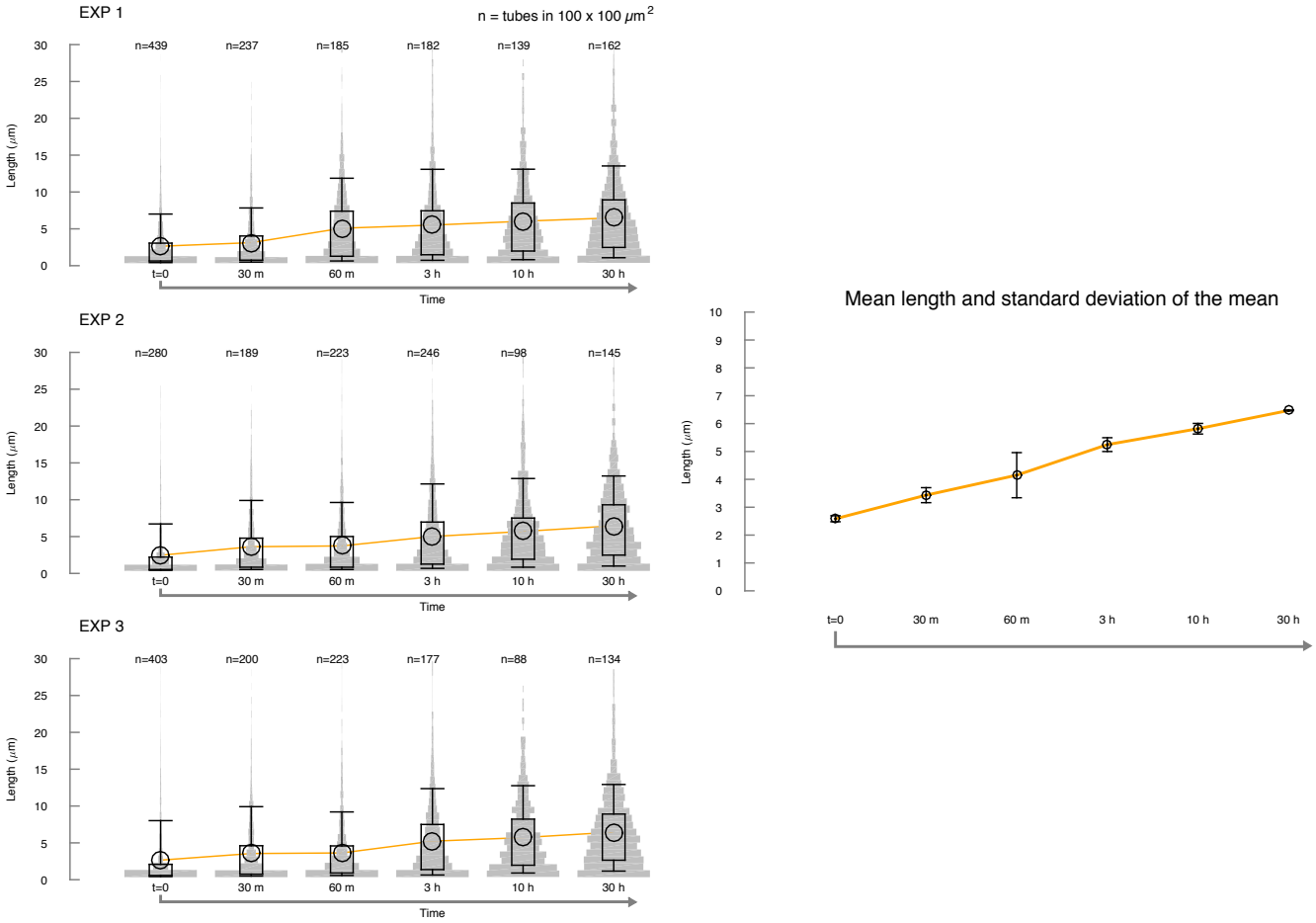

Figure 13: Growth of nanotubes annealed from tile sample where 100% of tiles include a toehold domain *Nanotube length was measured over 30 hours (after annealing) from fluorescence microscopy images. Left: Violin plots of each experiment repeat. Right: mean and standard deviation of the mean of length over the three experiments to the left.*

4.1.4 Comparison of mean nanotube length during growth experiments with different percentage of toeholded tile

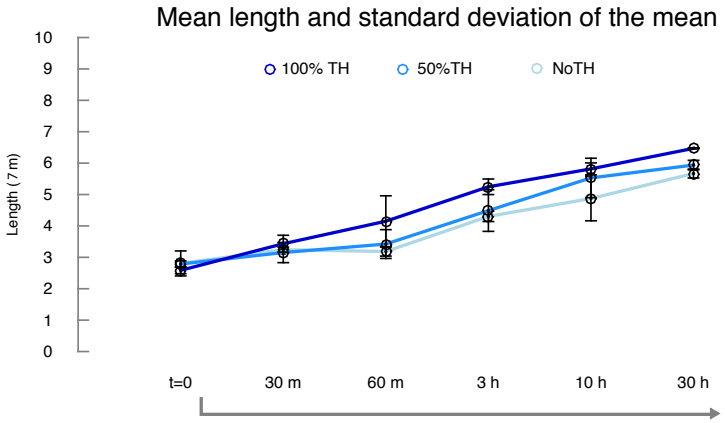

Figure 14: Growth of nanotubes is not significantly influenced by the presence of external toehold *We compare the mean length data from Fig. 11, 12, and 13; the presence of the 7 base external toehold appears to only slightly increase the growth rate.*

4.2 Fluorescence assays confirm external and internal toehold location

The position of the toehold in the nanotube was characterized by binding of streptavidin (conjugated with a cy3 fluorophore) to a biotinylated truncated invader strand that, in turn, binds to the toeholds without causing nanotube disassembly. This truncated invader strand binds to both internal and external toeholds. Streptavidin binds to the 3' end of this strand. The expectation is that the toeholds that show up on the inner surface of the nanotubes will not be able to bind to the streptavidin-truncated invader complex since the protein will not fit inside the nanotube. The external toeholds are expected to bind to the streptavidin-truncated invader complex without any problem.

A mixture of streptavidin and truncated invader was prepared at 1:4 ratio (streptavidin is tetravalent) in 1x TAE and 12.5 mM $MgCl_2$. The final concentration of truncated invader in the mix was 1 μM. The mixture was incubated at room temperature for 30 minutes. Cy5-labeled nanotubes (1 μM) were mixed with the streptavidin-truncated invader mix at 1:4 ratio of Nanotube:streptavidin-truncated invader. The mixture was incubated at 4°C for 2 days. After incubation, the mixture was imaged in both Cy3 and Cy5 channels; example images are shown in Fig. 15. These images indicate that toeholds are exposed on the internal or external nanotube surface as intended. Fig. 15 A1 and A2 show results for internal toehold: no fluorescence is detectable in the Cy3 channel, indicating that there are no binding sites for streptavidin-bridged truncated invader; panels B1 and B2 show results for external toehold: fluorescent aggregates are visible in both channels, indicating that streptavidin-truncated invader complex binds to the external toeholds and since streptavidin is tetravalent, it binds to multiple nanotubes and promotes nanotube aggregation.

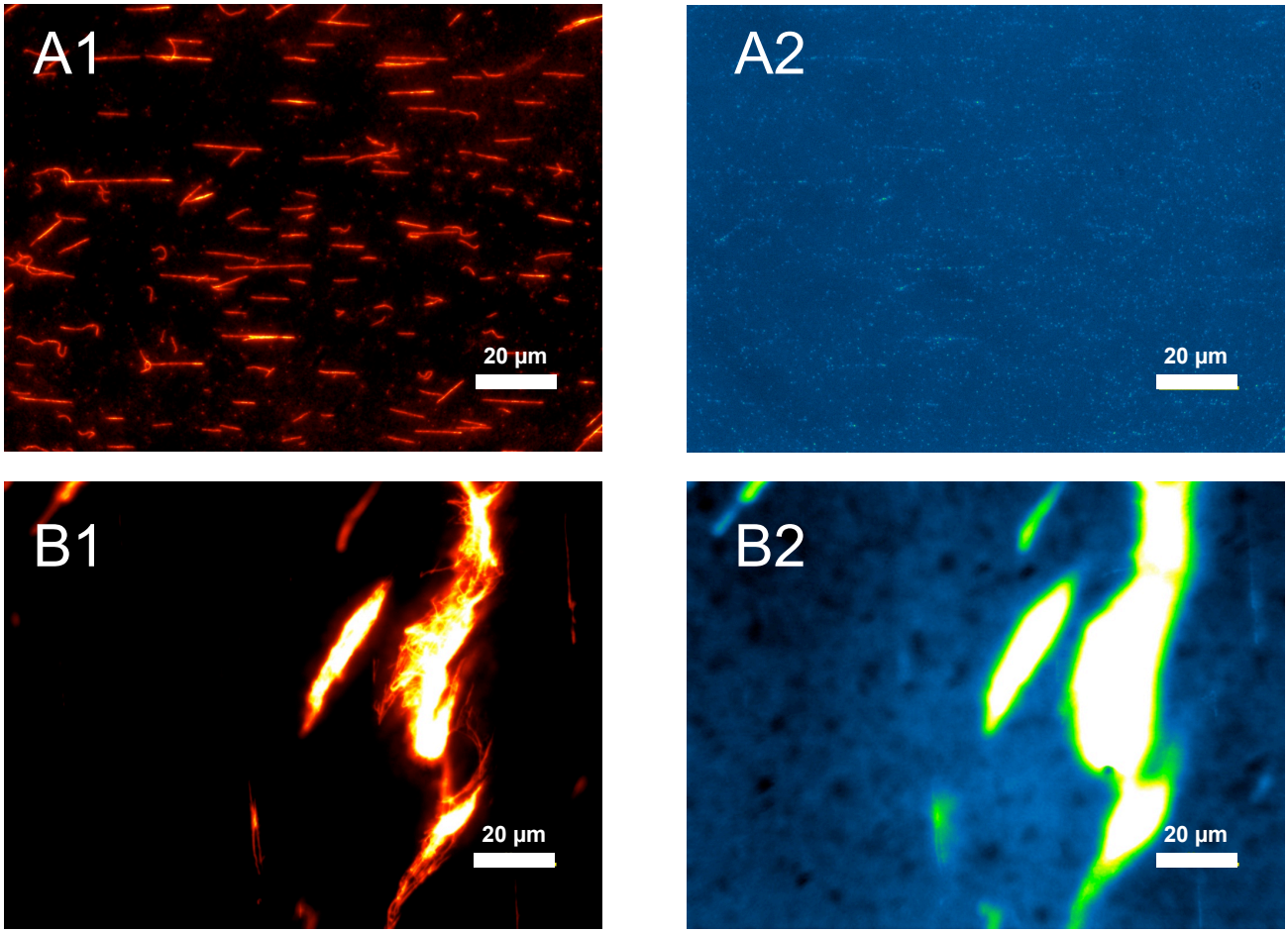

Figure 15: *A1 and A2: Nanotubes (5b SE) with internal toeholds after incubation with Streptavidin-truncated invader complex. A1 shows grown Cy5-labeled nanotubes. A2 is an image of the same sample with a Cy3 filter, which indicates virtually no streptavidin is bound to the nanotubes, following our expectation (toeholds are internal to the nanotube surface, therefore not available for streptavidin-truncated invader complex binding). B1 and B2: Nanotubes (5b SE) with external toehold after incubation with streptavidin-Truncated invader complex. B1 shows the Cy5 channel, and B2 shows the Cy3 channel. Both images show patches of fluorescence, which indicate that a) the streptavidin-bridged truncated invader complex binds to the external toeholds, b) due to tetravalent nature of streptavidin, it binds to multiple nanotubes and promotes aggregation.*

4.3 Invasion and anti-invasion reactions: Example images

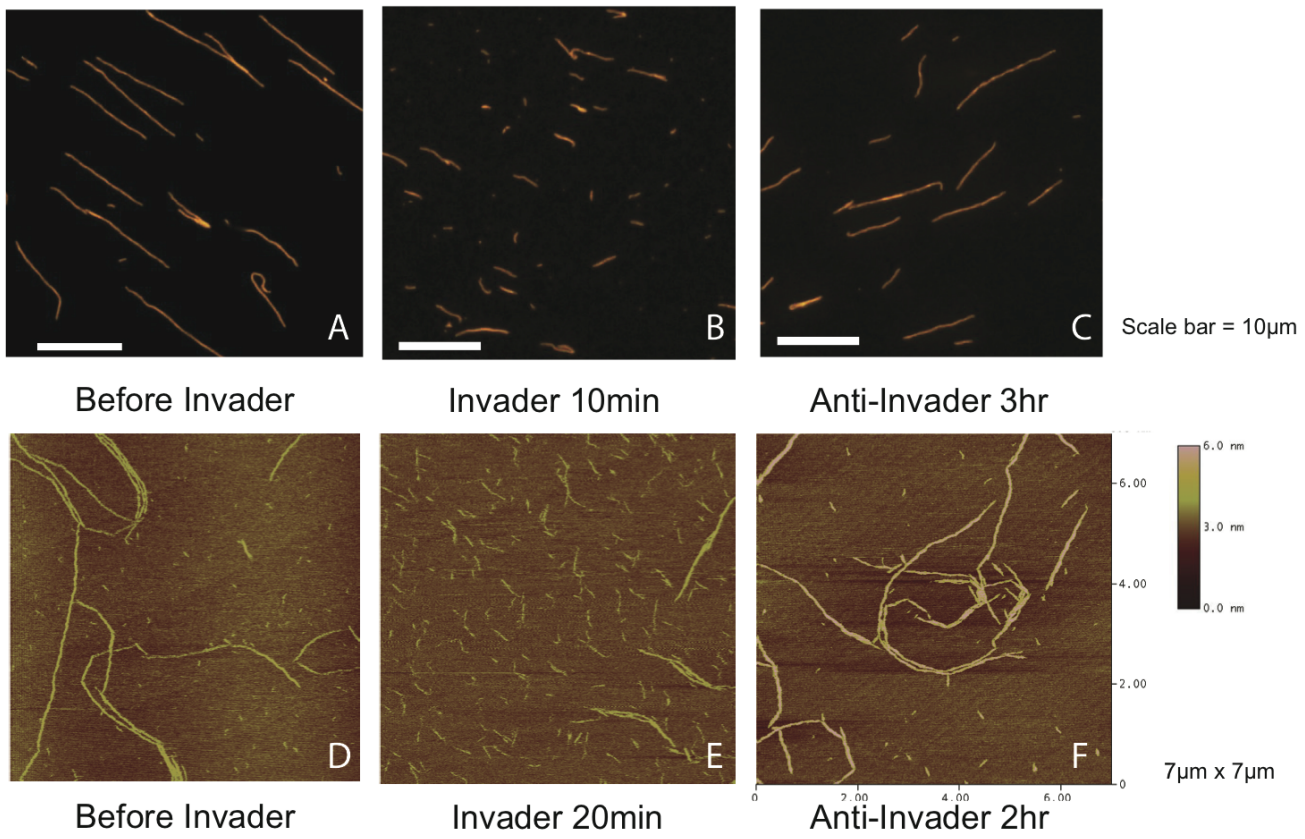

Figure 16: *Tubes with 50% tiles containing toehold (A:C) Fluorescent Microscopy and (D:F) Atomic Force Microscopy. Initial tubes (A,D). Invader reduces tube length significantly, yet tubes are still visible in both microscopy and AFM images (Figure B,E). The addition of anti-invader to tube solution allows nanotube regrowth (C,F).*

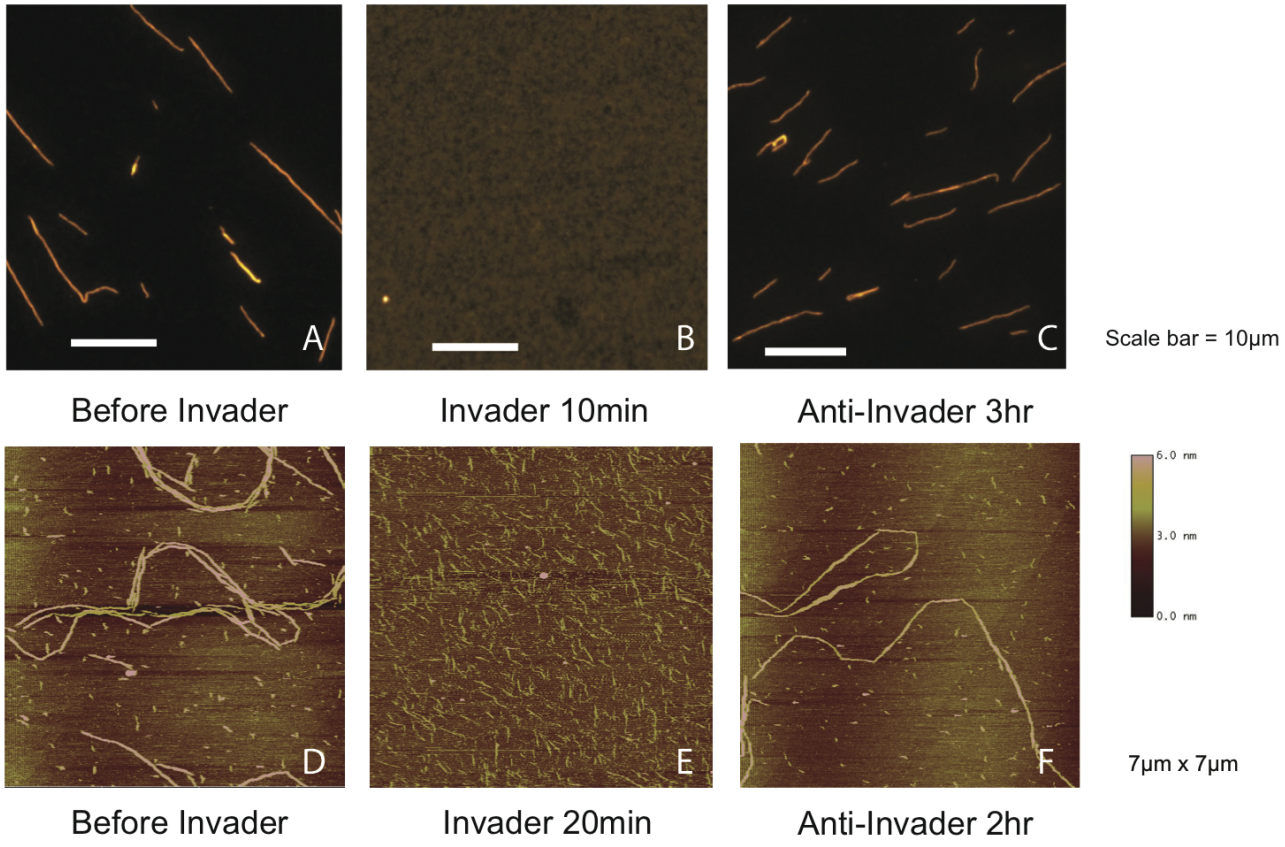

Figure 17: *Visualization of invasion and anti-invasion rxn of tubes with 100% tiles containing toehold (A:C) Fluorescent Microscopy and (D:F) Atomic Force Microscopy. Figures A and D illustrate tubes prior to invasion. After invasion reaction at room temperature, 10 min Figure B, and 20 min Figure E, tubes completely break apart. The presence of anti-invader promotes the re-assembly of tubes from monomer tiles or chunks, Figures C and F.*

4.4 Invasion and anti-invasion reactions: Time-lapse microscopy

Time-lapse movies were submitted as supplementary movies M1–M6. Data were collected according to the protocol described in Section 3.9.

- M1: Example view of a control sample with annealed nanotubes prior to invasion and anti-invasion. This video shows internal-toeholded nanotubes imaged for 11 minutes. The video was originally captured at the rate of one frame every 15 seconds, and has been sped up to get a run length of 9 seconds. Exposure time at every frame was 200 ms. This movie shows that over the imaging period the nanotubes are stable in the absence of invader and that the cy3 fluorophore does not bleach within the relevant time-frame.

- M2: Time-lapse movie of invasion reaction on nanotubes with external toehold. The video starts at around time=120 seconds after addition of invader to nanotubes. The video ends at time=431 seconds after invader addition. The video was captured at the rate of one frame every 30 seconds, with 200 ms exposure time at every frame. The video clearly shows the nanotubes breaking at many positions along the axis (instead of breaking from the extrema as in the case of internal-toeholded nanotubes).

- M3: Time-lapse movie of invasion reaction on nanotubes with internal toehold. The video starts at around 120 seconds after addition of invader to nanotubes, and it ends at t=810 seconds after invader addition. The video was captured at the rate of one frame every 30 seconds. Exposure time at every frame was 200 ms. Some of the nanotubes shrink from the ends upon invasion while others sometimes break along the axis (presumably due to defects on nanotube surface).

- M4: This is a cropped video of an internal-toeholded nanotube shrinking from the ends upon invasion.

- M5: This video shows the regrowth of broken down nanotubes after addition of anti-invader. The invader was added to the sample at time=0 mins, and the anti-invader was added at time=6 minutes. The video was recorded from time=20 minutes and ends at time=50 minutes. The video was originally captured at the rate of one frame every 15 seconds, in the current form it has been sped to have a total runtime of 18 seconds. Exposure time at every frame was 200 ms.

- M6: This is a video cropped from movie M5. Starting from time=20 minutes ending at time=35 minutes. The nanotubes show growth by end-to-end joining.

- M7: This is another video cropped from movie M5. Starting from time=20 minutes ending at time=50 minutes. Again, the nanotubes show growth by end-to-end joining.

We exclude the possibility that breakage observed in movies is an artifact of nanotubes motion. Control nanotubes (no invader or anti-invader present) do not get transiently short by becoming perpendicular to slides. Drifting of nanotubes was also excluded, by monitoring the field of view which is much larger than the "cropped" view.

4.5 Length distribution of nanotubes after invasion

We screened the steady state distribution of nanotube length in the presence of excess invader as a function of toeholded tile percentage, defined as the relative concentration of toeholded S2 strand and non-toeholded S2 strand in the annealing mix. We considered three different assays: 1) tiles without toeholded S2 strand, 2) 50% and 3) 100% concentration of toeholded S2 strand. Tiles were annealed at 1 μM concentration, and invader was added at a 5% excess concentration. Our results show that nanotubes annealed without toeholded tiles are relatively resilient to the presence of invader, and their growth is suppressed. Invasion causes a $\approx$50% decrease in the mean length of nanotubes with 50% toeholded tiles, and suppresses their regrowth. Finally, the mean length in samples of nanotubes with 100% toeholded tiles appear is virtually zero: no nanotubes are visible in fluorescence microscopy images, and their regrowth is suppressed. However, small assemblies are visible in AFM images (assembly may be mica-assisted).

After annealing (Section 3.1), nanotubes were incubated for 30 hours at 25°C prior to addition of invader. The length was measured at room temperature (25°C) using fluorescence microscopy (Methods Section 3.3). Each assay was conducted in triplicates. Nanotube length violin plots for each assay, together with plots of mean and standard deviation of the mean, are shown in Figures 18, 19 and 20. Means for the three different assays are compared in Figure 21.

4.5.1 Invasion of nanotubes in the absence of toeholded tiles

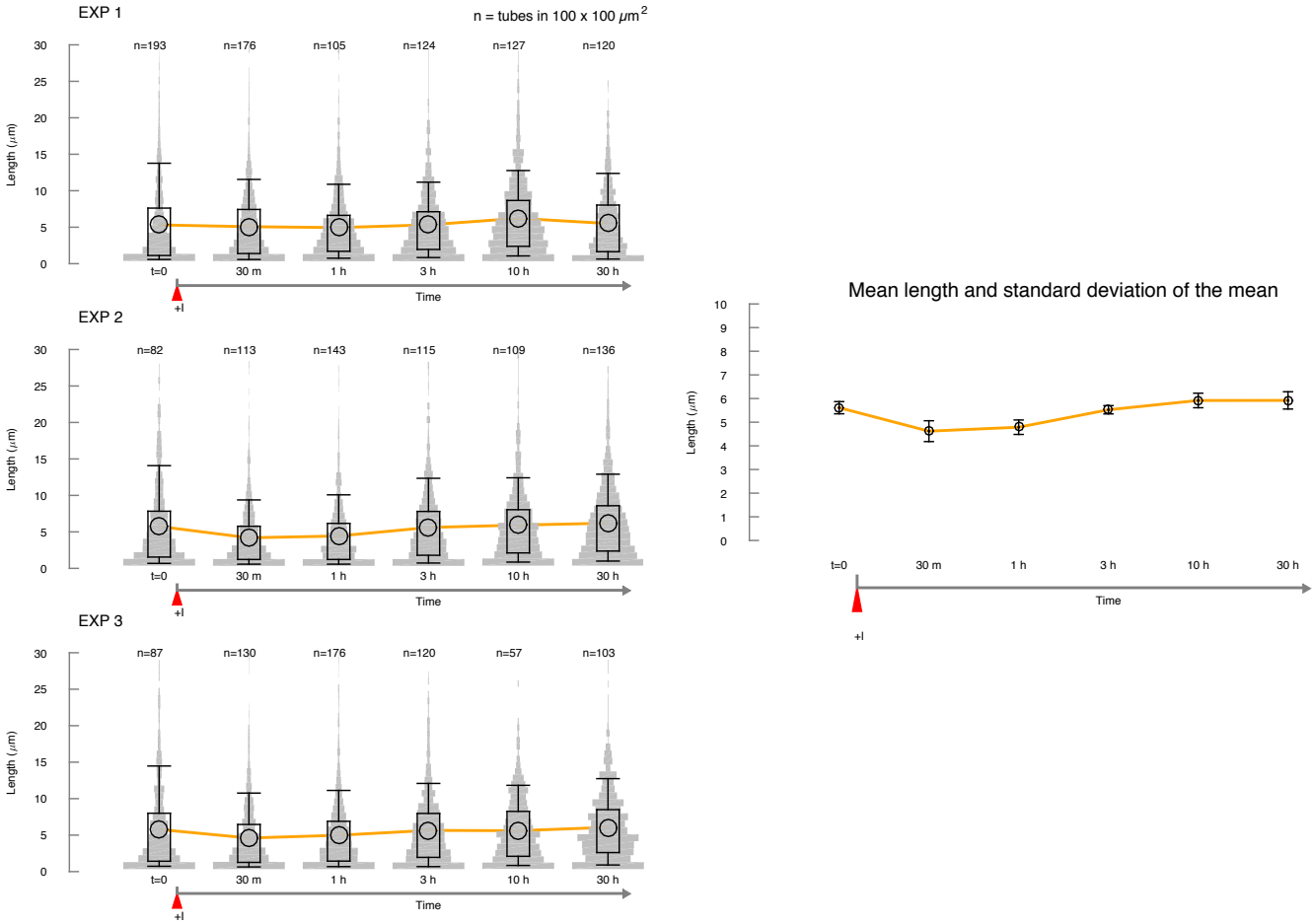

Figure 18: In the absence of toeholds nanotubes do not break in the presence of invader strand. *We measure the nanotube length for 30 hours after addition of invader; prior to the beginning of the experiments, nanotubes were incubated for 30 hours, reaching a mean length of about 6 μm [4]. The red triangle marks when invader is added to the sample. The results indicate that the invader does not significantly decrease nanotube length because the strand invasion reaction (Fig. 2) cannot be initiated in the absence of a toehold. However, the presence of invader appears to suppress further growth. Left: Violin plots of each experiment repeat. Right: mean and standard deviation of the mean of length over the three experiments to the left.*

4.5.2 Invasion of nanotubes with 50% toeholded tiles

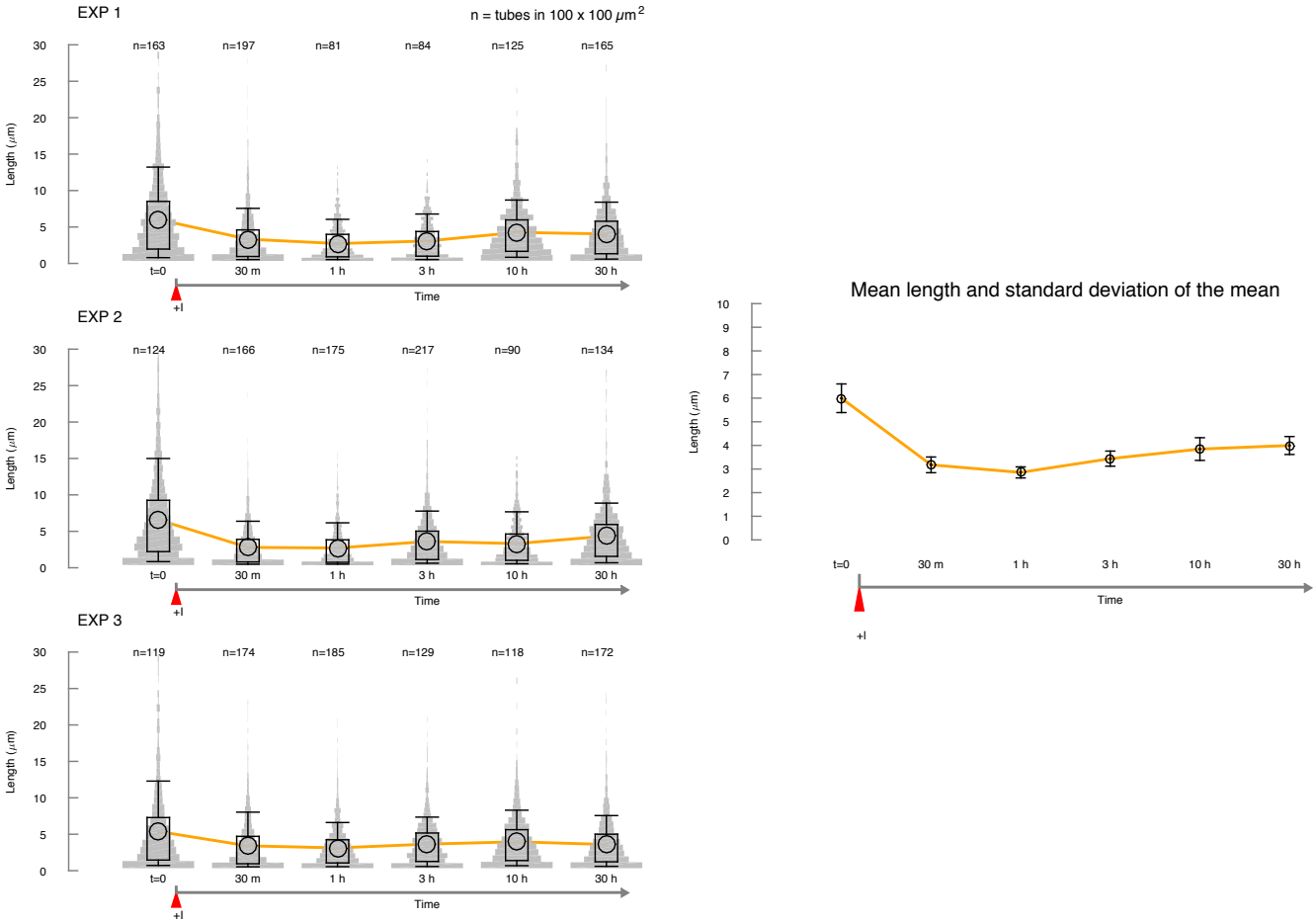

Figure 19: Invasion reaction of nanotubes where 50% of tiles include a toehold domain. *After addition of invader (marked by the red triangle) the mean nanotube length rapidly decreases to half the initial length, and remains constant for the following 30 hours. Left: Violin plots of each experiment repeat. Right: mean and standard deviation of the mean of nanotube length over the three experiments to the left.*

4.5.3 Invasion of nanotubes with 100% toeholded tiles

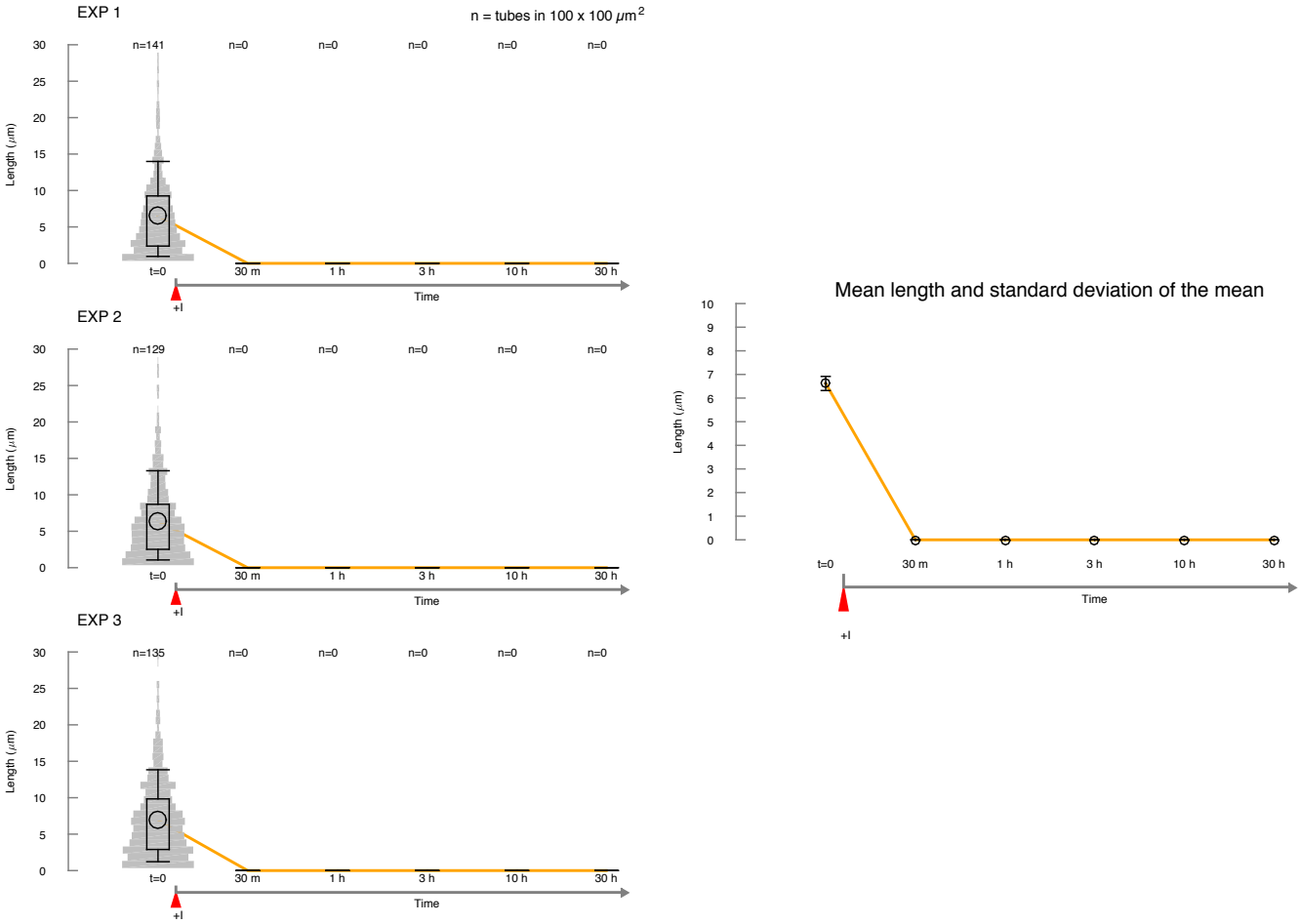

Figure 20: Invasion reaction of nanotubes where 100% of tiles include a toehold domain. *After addition of invader (marked by the red triangle) nanotubes rapidly disassemble and no nanotubes can be seen in fluorescence microscopy images; nanotubes do not reform in the following 30 hours. Right: mean and standard deviation of the mean of nanotube length over the three experiments to the left.*

4.5.4 Comparison mean length during invasion reaction in nanotubes with different percentage of toeholded tile

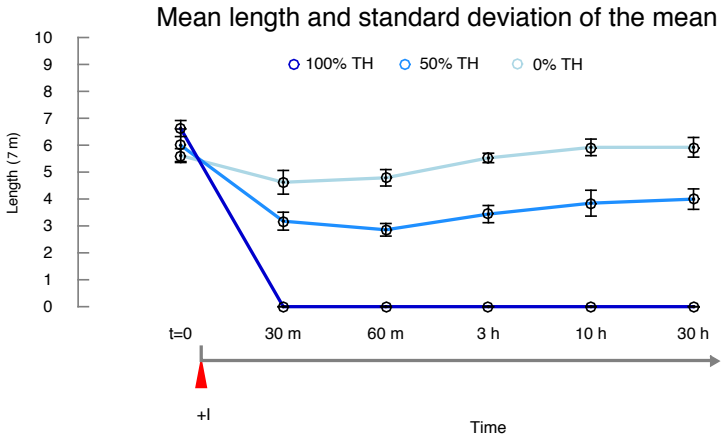

Figure 21: Invasion causes a decrease in mean nanotube length that depends on the concentration of toeholded tiles *This plot compares the mean length data from Fig. 18, 19, and 20.*

4.6 Nanotube invasion as a function of toehold length

The length of the toehold in strand S2 determines the stability of the invader-tile complex. (It is also known that the speed of a toehold-mediated strand displacement reaction is proportional to the length of the toehold, as shown by [27] and many following studies). If the length of the toehold in S2 is decreased, the invader-S2 duplex is shortened and its dissociation rate is expected to become higher. To test this hypothesis, we evaluated invasion reactions in tiles with 3 and 5 bases long toehold in strand S2, and performed invasion assays as described in the previous Section 4.5. Our results validate this hypothesis: invasion of nanotubes assembled from tiles with shorter toeholds results in a reduction of mean length that is around 50% the initial length; in addition, after a transient nanotubes resume growth, indicating that a considerable fraction of the tile population is not bound to invader and thus available for nucleation and polymerization.

Nanotubes were annealed (Section 3.1) from 100% toeholded tiles at 1 μM tile concentration, using strands S2 3'T 5bp or S2 3'T 5bp (Table 1). After annealing, tubes were incubated for 30 hours at 25°C. Invader was added at 5% tile concentration excess. Violin plots of the corresponding distributions, together with mean and standard deviation of the mean are shown in Figures 22 and 23. Mean length of these two assays is compared with the mean of invasion reaction on 7-base toeholded tile (S2 3'T 7bp) in Figure 24.

4.6.1 Invasion of nanotubes with 3-base toehold length

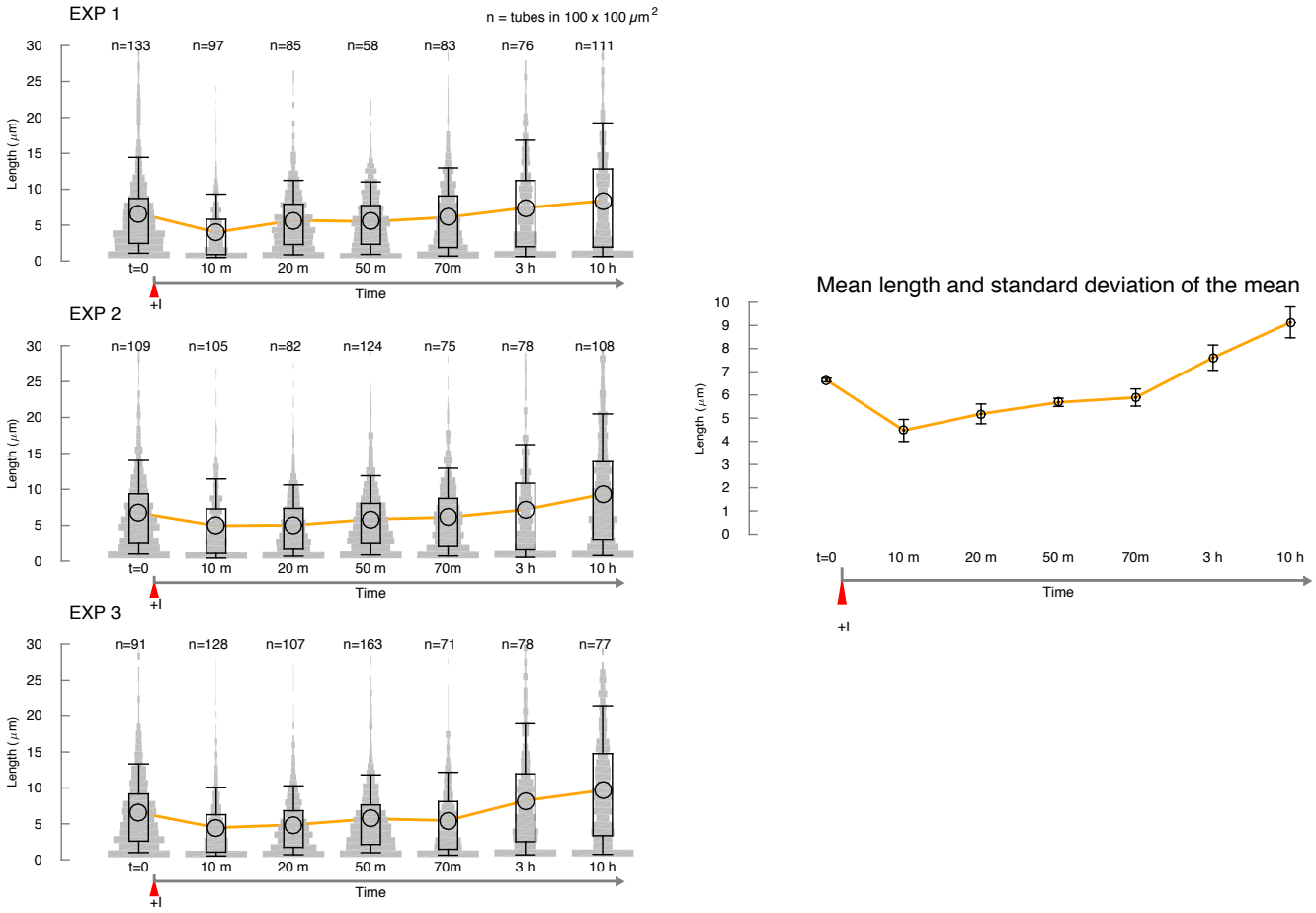

Figure 22: Invasion reaction on nanotubes with 100% tiles including a 3 base-long external toehold. *A 3 base toehold enables weak breakage of nanotubes, as indicated by the slight decrease in mean length after addition of invader (marked by the red triangle). On average, nanotubes subsequently regrow reaching mean length higher than their initial length. Left: Violin plots of separate experiments. Right: Mean and standard deviation of the mean for the length distributions measured in the experiments to the left.*

4.6.2 Invasion of nanotubes with 5-base toehold length

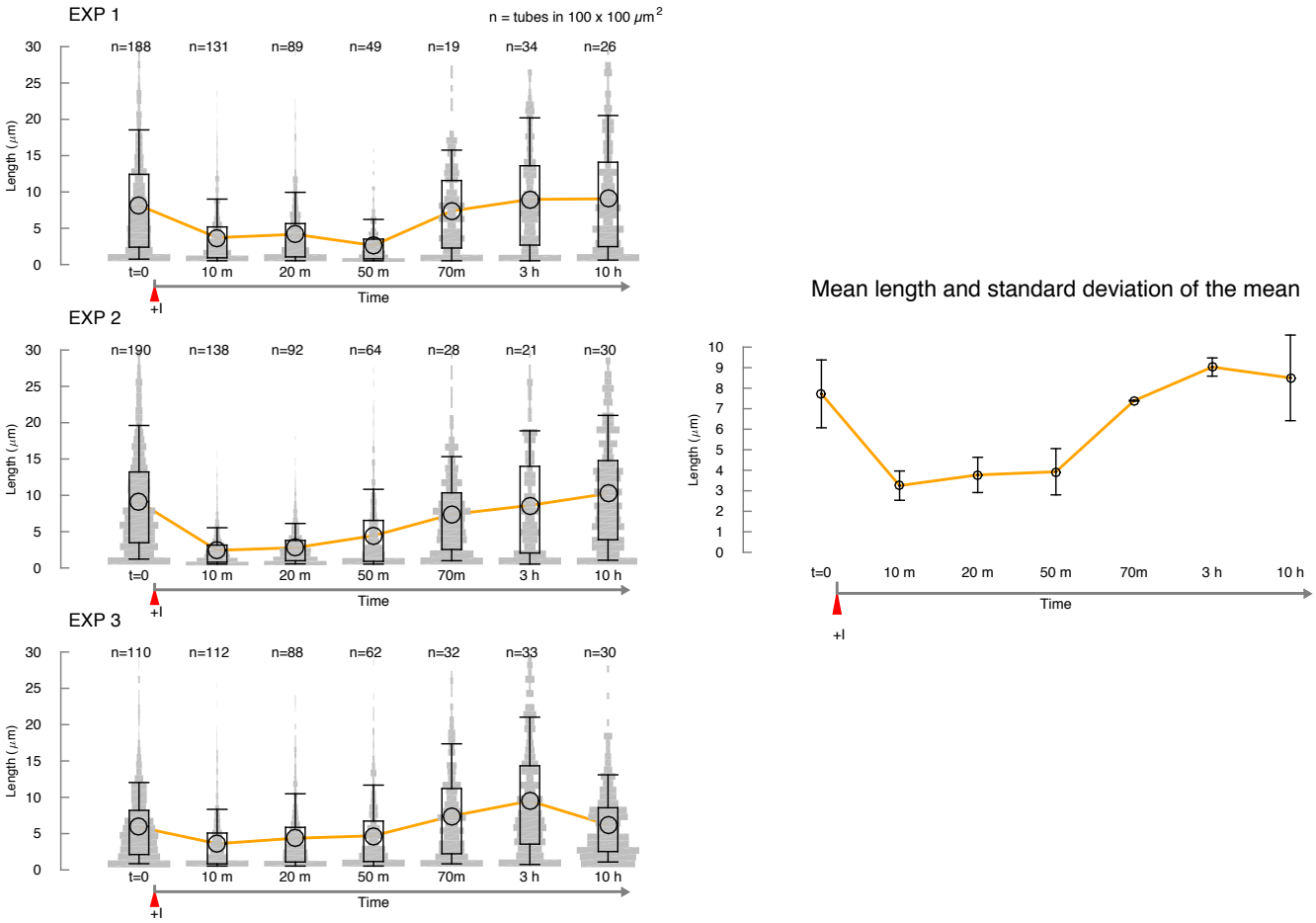

Figure 23: Invasion reaction on nanotubes with 100% tiles including a 5 base-long external toehold. *A 5 base toehold is sufficient to initiate breakage of nanotubes. Addition of invader (marked by the red triangle) results in roughly a 30% decrease in the mean nanotube length; however, nanotubes subsequently regrow reaching mean length comparable to the initial mean length. Left: Violin plots of separate experiments. Right: Mean and standard deviation of the mean for the length distributions measured in the experiments to the left.*

4.6.3 Comparison of mean length during invasion reaction in nanotubes with different toehold length

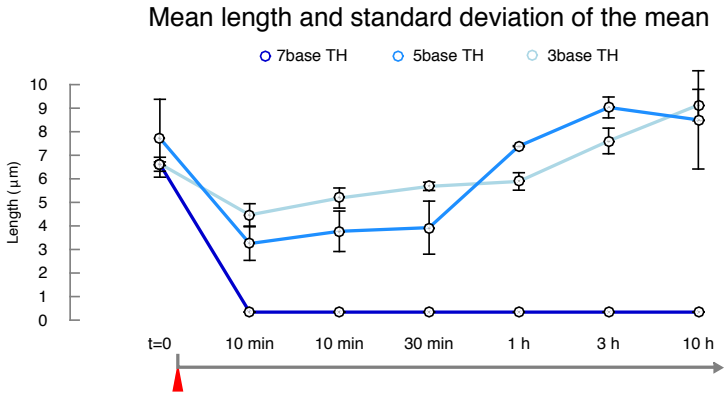

Figure 24: A 7 base-long toehold is necessary to fully break nanotubes and suppress growth. *We compare the mean length measured in invasion experiments using nanotubes grown from 3 base, 5 base and 7 base-long toehold tiles (100% tiles including an external toehold). Addition of invader is marked by the red triangle. A 7 base toehold is necessary to fully break nanotubes and suppress their regrowth.*

4.7 Length distribution of nanotubes after invasion and anti-invasion

Anti-invasion restores the ability of tiles to nucleate and polymerize by displacing and titrating the invader strand.

We screened the steady state distribution of nanotube length in the presence of invader and subsequent addition of anti-invader, as a function of toeholded tile percentage (defined as the relative concentration of toeholded S2 strand and non-toeholded S2 strand in the annealing mix). We report the results of three different assays: 1) tiles without toeholded S2 strand, 2) 50% and 3) 100% concentration of toeholded S2 strand. In all these experiments we used tiles with 7 base-long (external) toehold on strand S2 (Fig. 1 A4). Tiles were annealed at 1 μM concentration (Section 3.1), and after completion of the annealing procedure, nanotubes were incubated for 30 hours at 25°C prior to addition of invader. Invader was added at a 5% excess concentration, and anti-invader was subsequently added at 10% excess concentration (relative to the tile concentration). Invasion and anti-invasion reactions were done at room temperature (25°C).

Length distributions were measured using fluorescence microscopy images (Methods Section 3.3). Example images of nanotube samples after addition of invader and anti-invader are shown in Figures 16 (50% toeholded tiles) and 17 (100% toeholded tiles). Each assay was conducted with triplicate experiments. Nanotube length violin plots for each assay, together with mean and standard deviation of the mean, are shown in Figures 25, 26 and 27. Mean lengths measured in the three different assays are compared in Figure 28.

Addition of invader and anti-invader can be repeated multiple times, as shown at the end of this section. Violin plots of nanotube distributions for cycles of invasion and anti-invasion, and corresponding means are shown in Figure 29. In each cycle, invader was added at a 5% excess concentration, and anti-invader was subsequently added at 10% excess concentration (relative to the tile concentration).

4.7.1 Invasion and anti-invasion of nanotubes in the absence of toeholded tiles

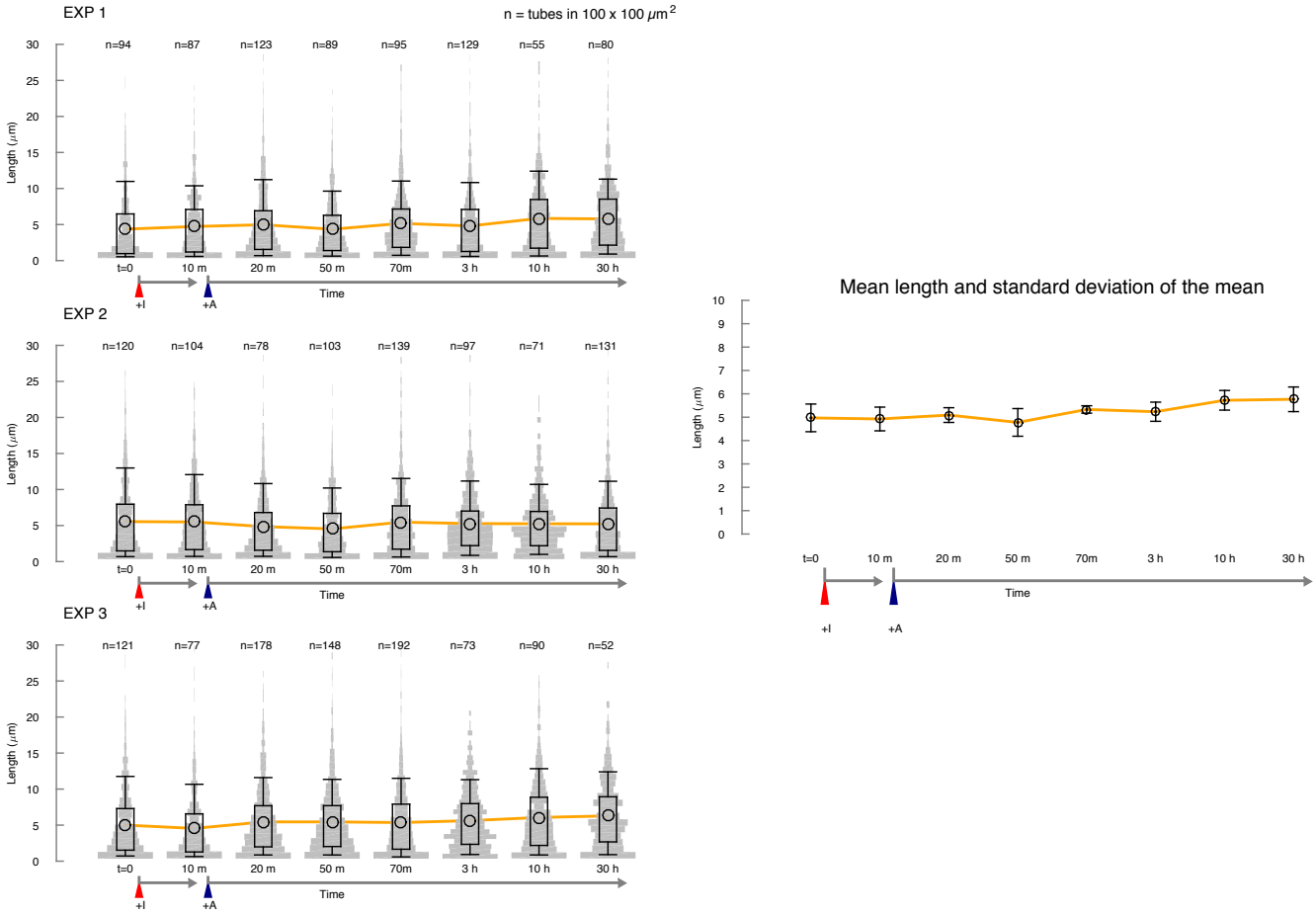

Figure 25: The mean length of nanotubes without toehold is not affected by the presence of invader and anti-invader. *Red and blue triangles mark respectively the addition of invader and anti-invader. The mean length of nanotubes does not decrease after addition of invader; addition of anti-invader does not promote further growth, suggesting that nanotubes have reached an equilibrium length distribution. Left: violin plots of each experiment. Right: mean and standard deviation of the mean for the experiments to the left.*

4.7.2 Invasion and anti-invasion of nanotubes with 50% toeholded tiles

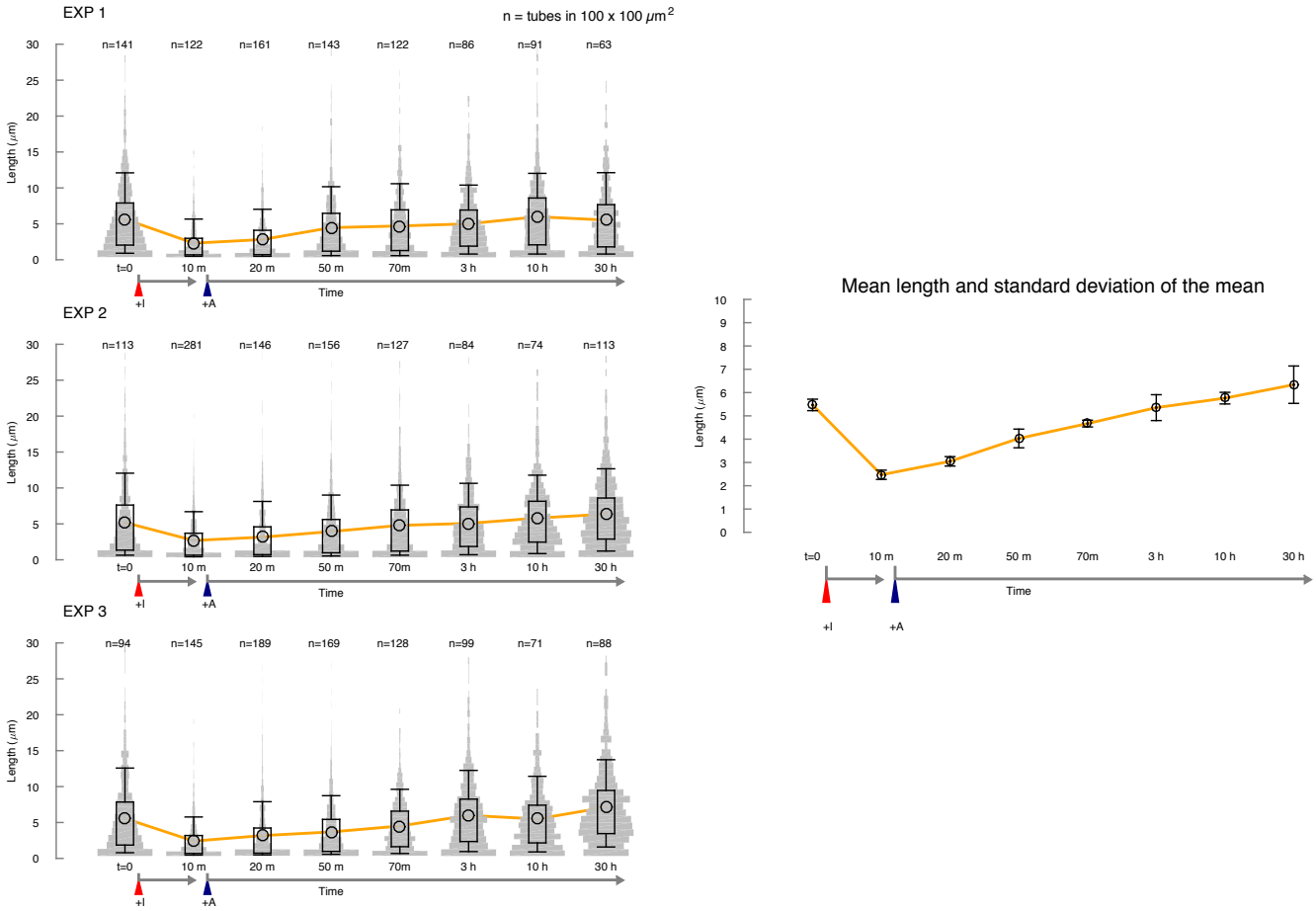

Figure 26: Invasion and anti-invasion of nanotubes with 50% toeholded tiles *Consistently with the experimental results on invasion (Fig. 19), nanotube mean length decreases by about 50% after addition of invader (marked by the red triangle). Addition of anti-invader (marked by blue triangle) promotes regrowth to a mean length that is comparable to the initial mean length. Left: violin plots of each experiment. Right: mean and standard deviation of the mean for the experiments to the left.*

4.7.3 Invasion and anti-invasion of nanotubes with 100% toeholded tiles

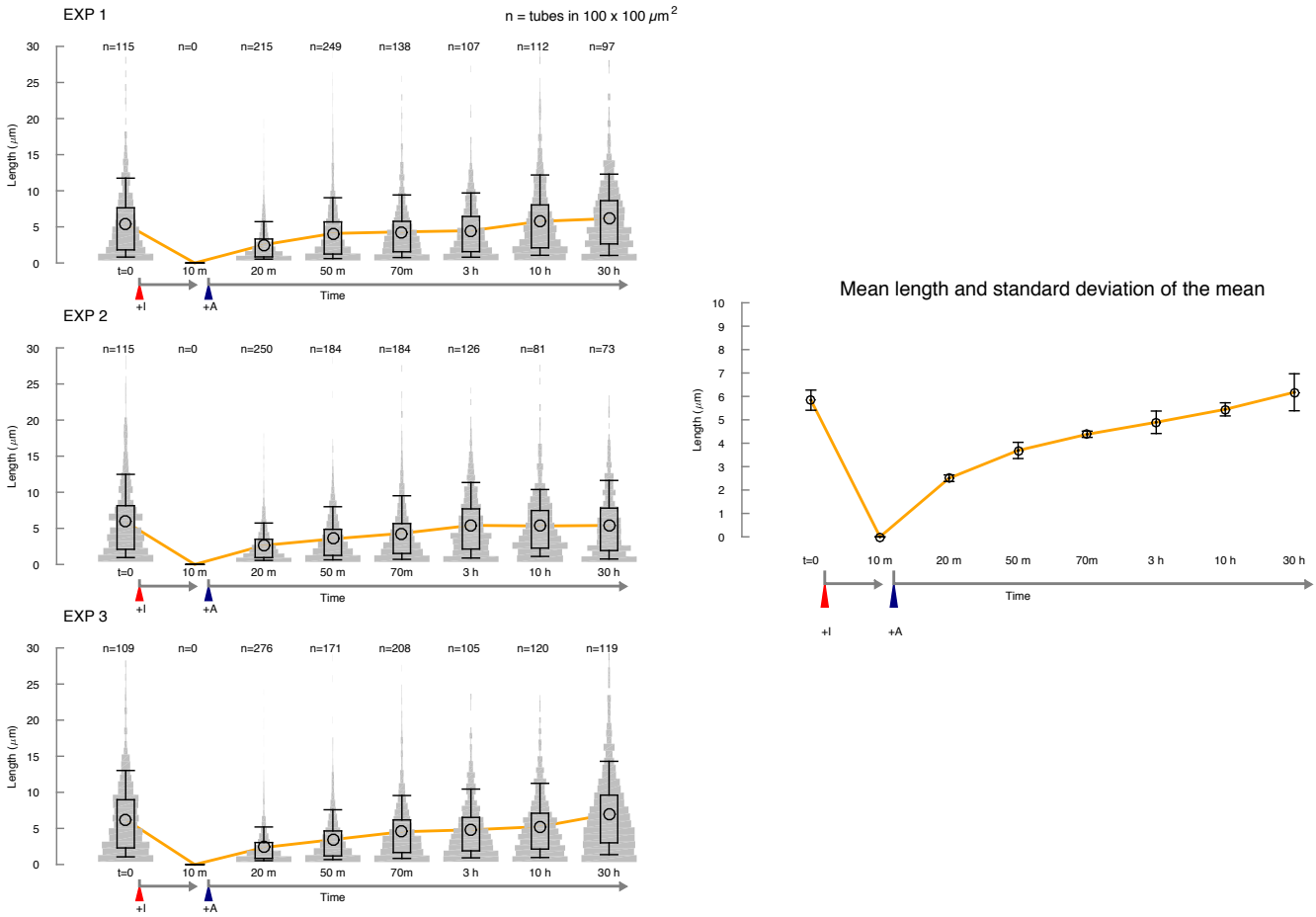

Figure 27: Invasion and anti-invasion of nanotubes with 100% toeholded tiles. *Addition of invader, marked by the red triangle, results in rapid disassembly of nanotubes (no nanotubes are visible in fluorescence microscopy images). When anti-invader is added, as marked by the blue triangle, nanotubes start regrowing reaching a mean length comparable to the initial length. Left: violin plots of each experiment. Right: mean and standard deviation of the mean for the experiments to the left.*

4.7.4 Comparison of mean length during invasion and anti-invasion reactions in nanotubes with different percentage of toeholded tile

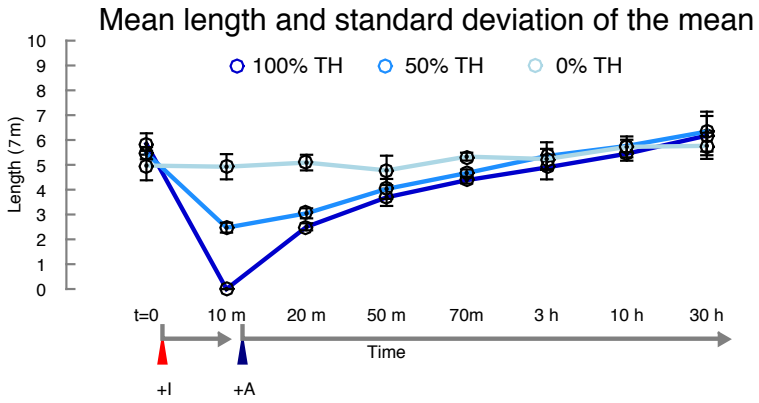

Figure 28: Comparison of mean nanotube length following invasion and anti-invasion reactions for different percentage of toeholded tiles. *This plot compares the results shown in Fig. 25, 26 and 26.*

4.7.5 Cycles of invasion and anti-invasion in nanotubes with 100% toeholded tiles

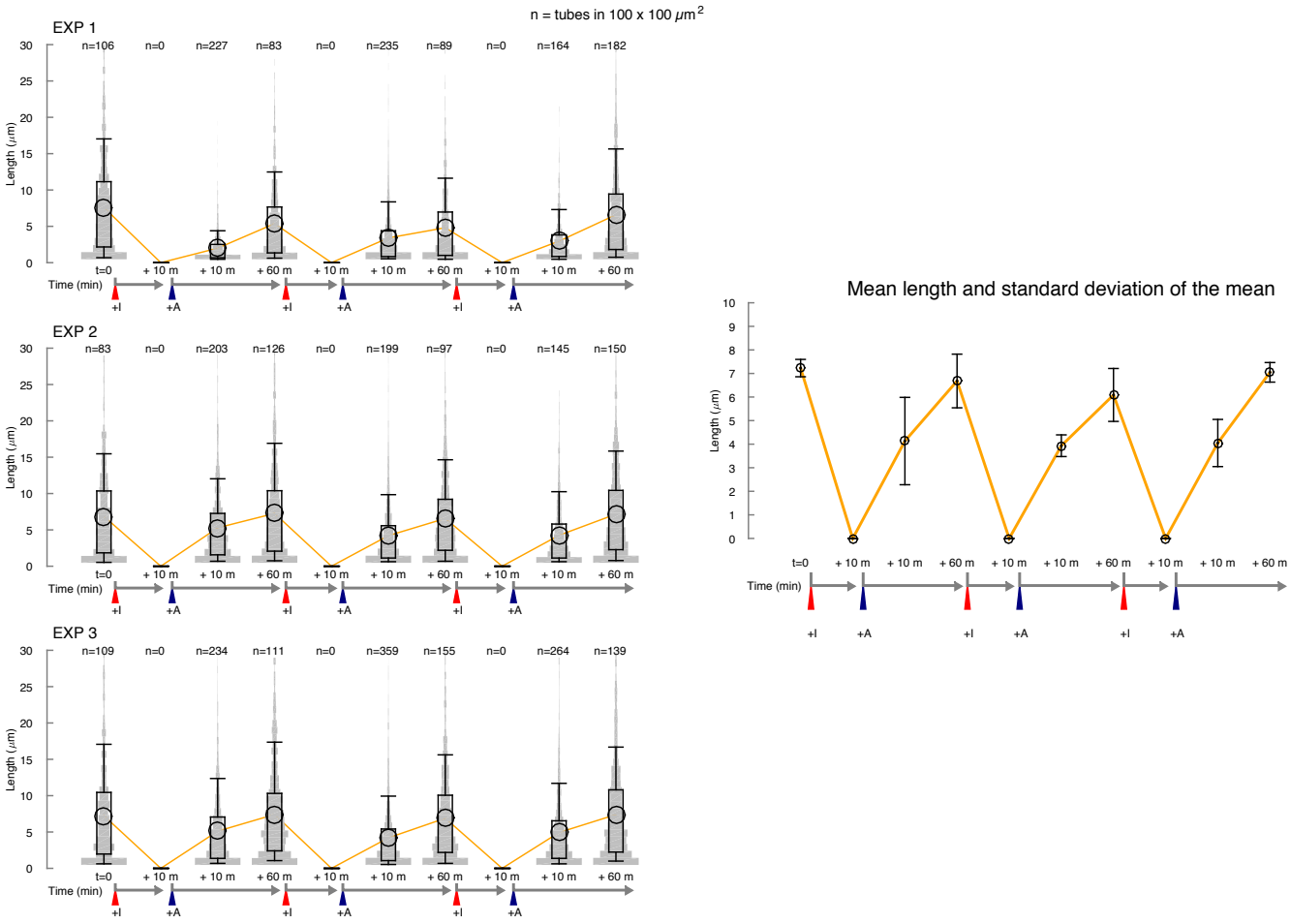

Figure 29: Repeated addition of invader and anti-invader result in reversible cycles of assembly and disassembly. *Left: Violin plots of each experiment. Right: Mean and standard deviation of the mean of the experiments to the left.*

4.7.6 Gel analysis of invasion and anti-invasion reactions

Tubes containing tiles with toeholded strand S2 at different percentages were annealed using the protocol outlined in Section 3.1. Our tile monomer reference band was obtained by annealing all the DNA strands required for formation of tiles together with the invader strand. A high-melt agarose gel was prepared at 0.5%, 1x TAE and 12.4mM $MgCl_2$, following the protocol described at Section 3.6. A sample of 2 μL of Tubes (1 μM), labeled with Cy3, were reacted with 0.3 μL (8.33 μM) Invader for 20 min and then for anti-invasion samples, 0.35 μL (8.33 μM) anti-invader was added for 2 hours at 25°C. The gel wells were sealed using thin films of solid and molten agarose. Electrophoresis was conducted at room temperature. To avoid overheating, the voltage was lowered to 60V and was allowed to run for a total time of 1 hour 30 minutes. Using Cy3 channel of BioRad Universal Hood III gel imager, the change in band intensity of breakdown products of monomer tiles, polymer smears, and tubes was analyzed and reported in Figure 30.

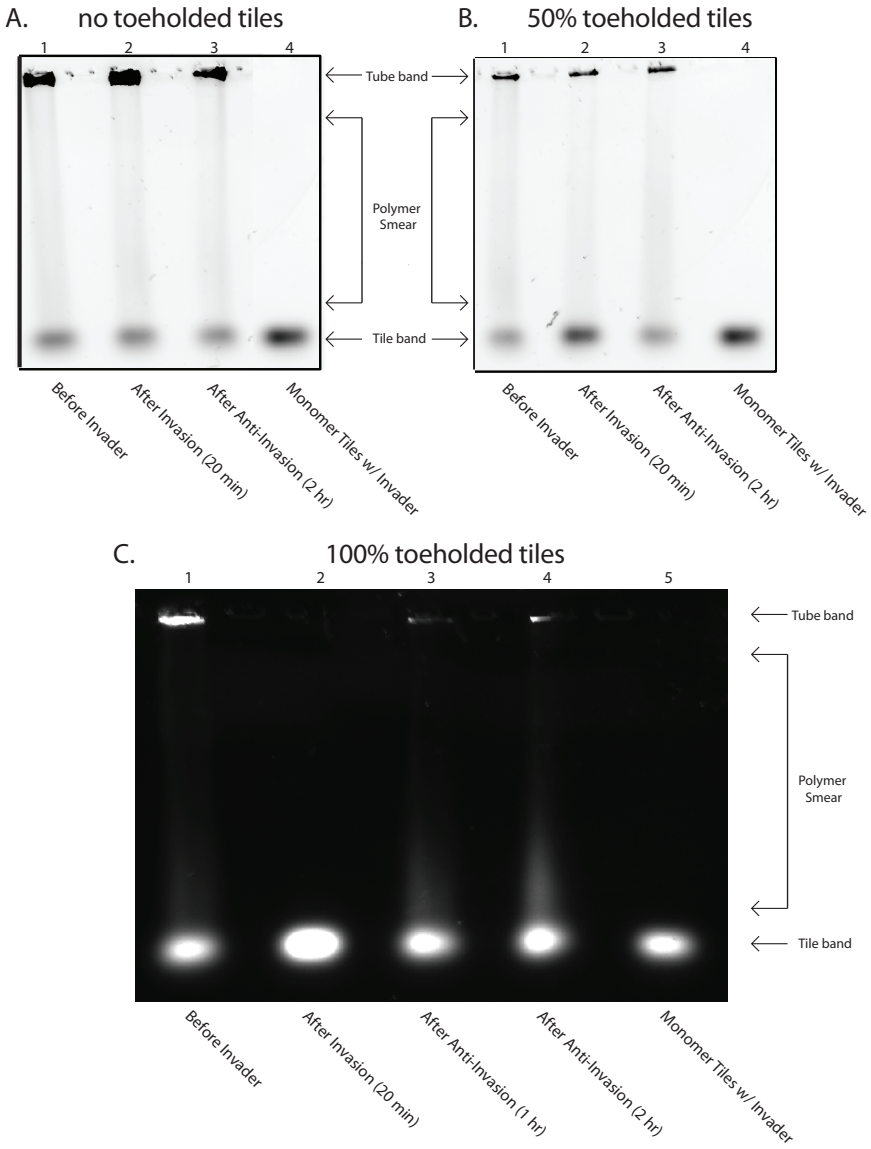

Figure 30: *Gel Assays analyzing breakdown products of invasion and anti-invasion of various tile with toehold concentrations (external toehold). Tubes/tiles are labeled with Cy3. Assembled nanotubes are too large to run through 0.5% agarose gel: a dark (high fluorescent) band at the top of lanes (A:C) indicate tubes that are not able to enter gel. The lowest bands in A:C are unpolymerized tiles or breakdown (invasion) products. The smear between the nanotube and tile bands represent joined tiles not yet polymerized into nanotubes. Control lane: nanotubes annealed with invader – Figures A,B = Lane 4, Figure C = Lane 5. A. 0% of tiles contain toehold. The intensity of tile bands in lanes 1:3 has no noticeable change, indicating that nanotubes with 0% toehold are not broken when mixed with invader. B. Nanotubes with 50% tiles containing toehold. The sample in lane 1, nanotubes after anneal and incubation, shows a faint band corresponding to unpolymerized tiles (cf. control lane 5). After adding invader strand to the nanotube sample (lane 2), the intensity of breakdown products increases significantly. However, there are still nanotubes present in the top band, indicating that some nanotubes form shorter breakdown products, as other tubes remain intact. C. Nanotubes with 100% of tiles with toehold. Lane 1 shows a nanotube band that prior to adding invader, and a faint band corresponding to unpolymerized tiles. After incubation with invader (lane 2), the band corresponding to nanotubes completely disappears, while the tile band becomes more prominent. Lanes 3 and 4 (anti-invasion after 1 hour and 2 hour incubation respectively) show that the nanotube band reappears (as well as a more noticeable smear in the lane).*

4.8 $MgCl_2$ Concentration Optimization

The presence of divalent magnesium ions helps with the stability of B-helix DNA strands by interacting with the negatively charged sugar phosphate backbones [3]. In optimizing tube dynamics, we studied how divalent magnesium ions at different concentration affect the stability of the tubes being invaded and anti-invaded. Tubes were annealed using protocol in Section 3.1, varying the $MgCl_2$ concentration from the nominal 12.4 mM to 24.8mM, 6.2mM, and 3.1mM. Samples annealed at 3.1 mM did not result in any assembled nanotubes. All invader (5% excess to tile concentration) and anti-invader (10% excess to tile concentration) reactions were conducted in 1x TAE buffer with appropriate $MgCl_2$ concentration at 25°C.

4.8.1 Invasion and anti-invasion reactions at 24 mM $MgCl_2$

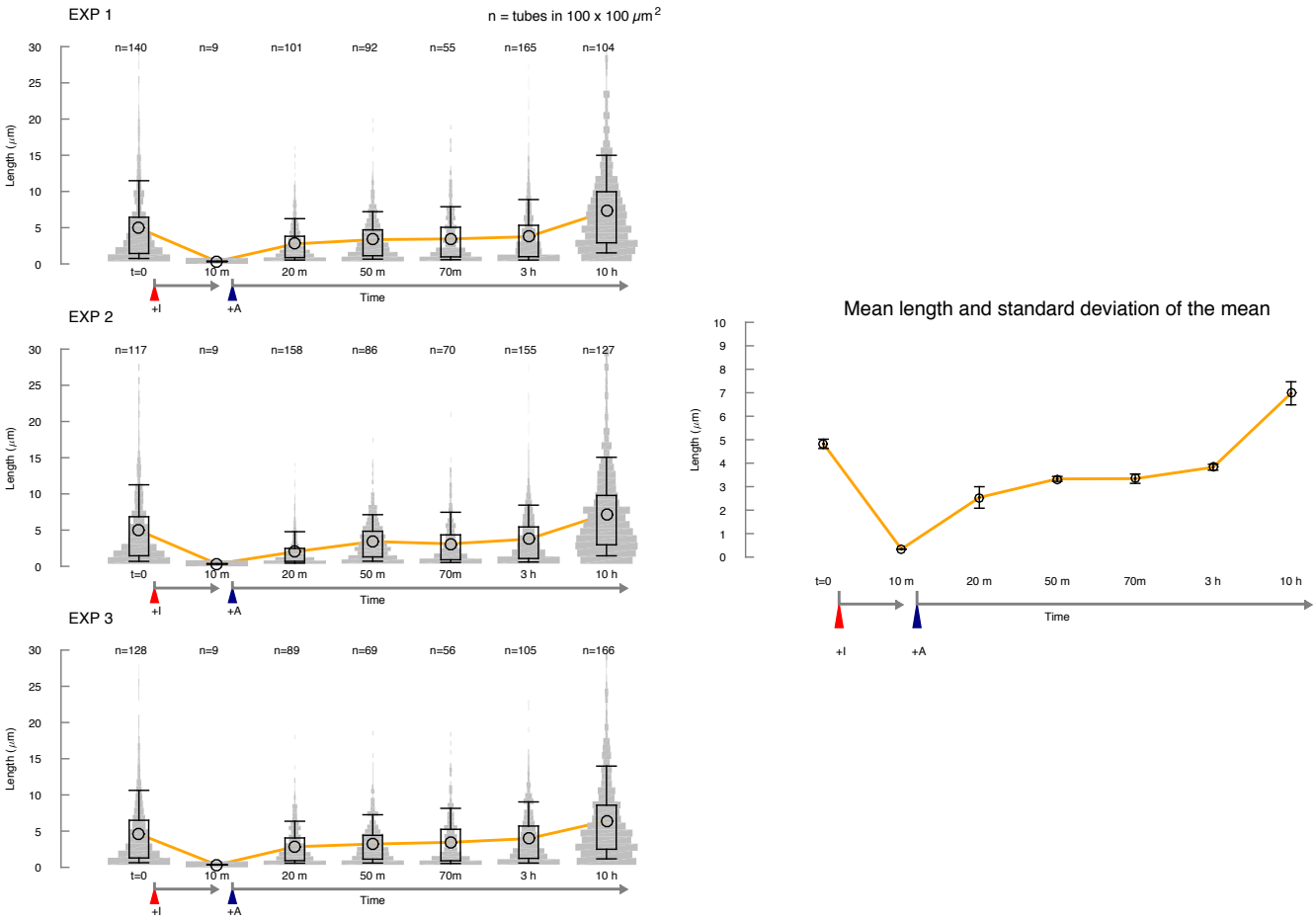

Figure 31: Invasion and anti-invasion reactions in the presence of 24.8 mM $MgCl_2$ *The concentration of $MgCl_2$ in these experiments is twice the concentration used in typical annealing conditions. The mean length of nanotubes after addition of invader (red triangle) decreases to zero (no nanotubes are visible in fluorescence microscopy experiments). Addition of anti-invader (blue triangle) promotes nanotube regrowth as at nominal $MgCl_2$ concentration. Left: Violin plots of each experiment. Right: Mean and standard deviation of the mean of the experiments to the left.*

4.8.2 Invasion and anti-invasion reactions at 6 mM $MgCl_2$

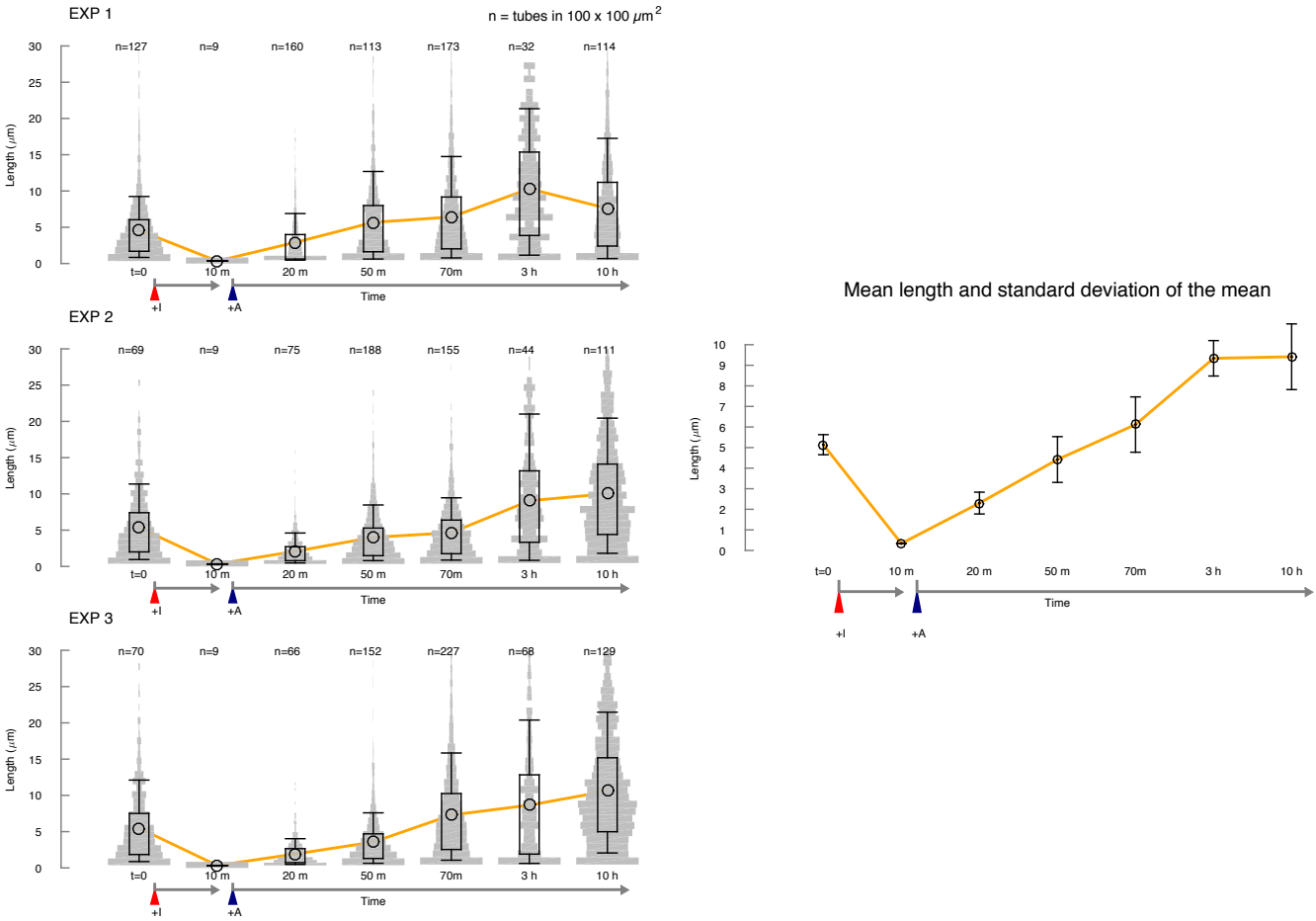

Figure 32: Invasion and anti-invasion reactions in the presence of 6.1 mM $MgCl_2$ *The concentration of $MgCl_2$ in these experiments is half the concentration used in typical annealing conditions. The mean length of nanotubes after addition of invader (red triangle) decreases to zero (no nanotubes are visible in fluorescence microscopy experiments). Addition of anti-invader (blue triangle) promotes nanotube regrowth reaching a mean length that exceeds the mean length at nominal $MgCl_2$ concentration. Left: Violin plots of each experiment. Right: Mean and standard deviation of the mean of the experiments to the left.*

4.8.3 Comparion of mean nanotube length after invasion and anti-invasion at varying $MgCl_2$ concentrations

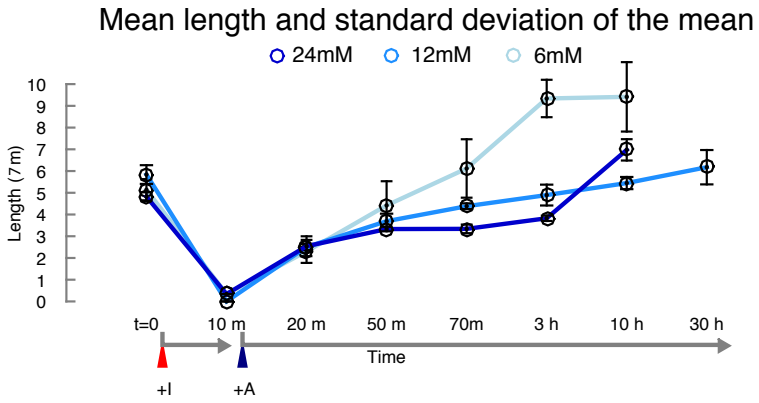

Figure 33: Comparison of mean nanotube length after invasion and anti-invasion at different concentrations of $MgCl_2$. *This plot compares mean length shown in Fig. 31 and 32. These results indicate that a concentration of $MgCl_2$ lower than the nominal concentration (12.4 mM) facilitates nanotube regrowth.*

4.9 Invasion and anti-invasion reactions on nanotubes with internal toehold

We tested the capacity of invasion and anti-invasion reactions to modulate the length of 5 base sticky-end nanotubes with 7 base-long toehold designed to be exposed on the internal surface of the nanotubes (toehold is positioned on the 3' end of strand S2, see sequence S2 3'T reported in Table 1). This assay was conducted with 100% of strand S2 having an internal toehold. After annealing, nanotubes were incubated at room temperature for 30 hours; incubation results in nanotubes with mean length of $\approx 12\mu$m, a two-fold increase relative to nanotubes with external toehold. The reason behind this increase is yet to be elucidated. At room temperature (25°C), invader was added at a 5% excess concentration, and anti-invader was subsequently added at 10% excess concentration (relative to the tile concentration). Violin plots for each experiment in this assay and the mean length are shown in Figure 34.

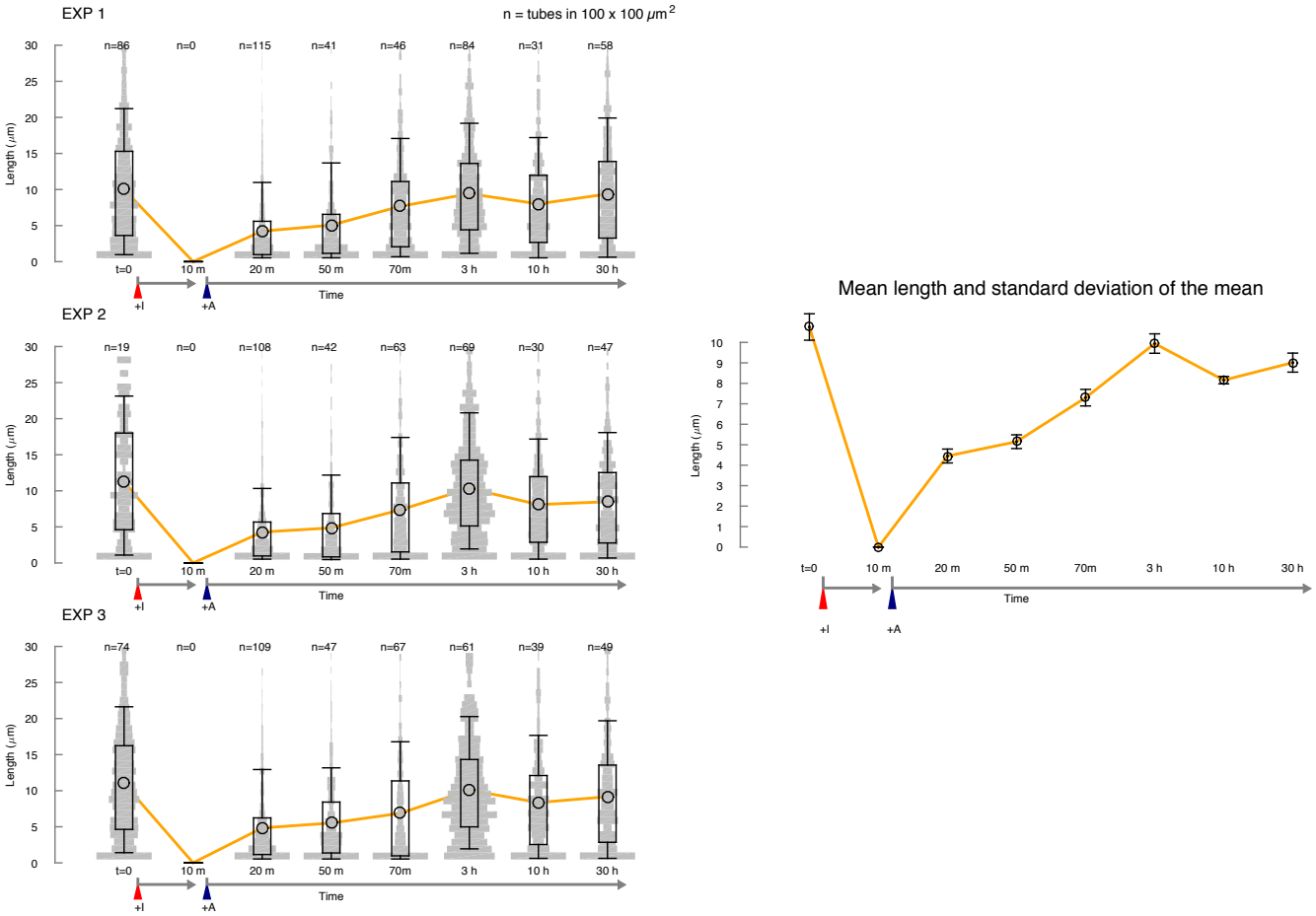

Figure 34: Invasion and anti-invasion reactions of nanotubes with internal toehold. *Left: Violin plots of each experiment. Right: Mean and standard deviation of the mean of the experiments to the left.*

4.10 Tiles with 8 base sticky ends are required to obtain nanotubes that are stable in the presence of enzymes

Tiles with 5 base sticky ends are not stable in the buffer mix and temperature conditions required for transcription; in addition, we found that T7 RNA polymerase promotes melting of nanotubes via a mechanism yet to be elucidated (Section 4.11.1). Thus, we extended the sticky end domains of our tiles and tested the stability of annealed nanotubes at 37° C, in the presence of transcription buffer, and T7 RNAP.

4.11 Invasion and anti-invasion of nanotubes with 8 and 7 base sticky ends

Nanotubes annealed from tiles having 7 and 8 base sticky ends are stable when incubated in transcription mix at 37° C. We further tested the effect of these temperature and buffer conditions on invasion and anti-invasion reactions. We find that invasion and anti-invasion reactions on nanotubes annealed from 7 base sticky end tiles result in mean length profiles similar to what was observed in 5 base sticky end tile nanotubes (Fig. 35). Regrowth after anti-invasion is slower in nanotubes annealed from 8 base sticky end tiles (Fig. 36), presumably due to the possibility of anti-invader binding to the sticky end of strand 4 (Fig. 4), and the formation of undesired complexes.

Fluorescence microscopy experiments were done by annealing tiles at 1μM tile concentration in 1X transcription buffer (New England Biolab) and incubated at room temperature for 30 hours. Invader species was added at 5% concentration excess, and anti-invader was added to invaded nanotube solution at 10% concentration excess (relative to tile concentration). Violin plots and mean plots are shown in Figs. 35 and 36.

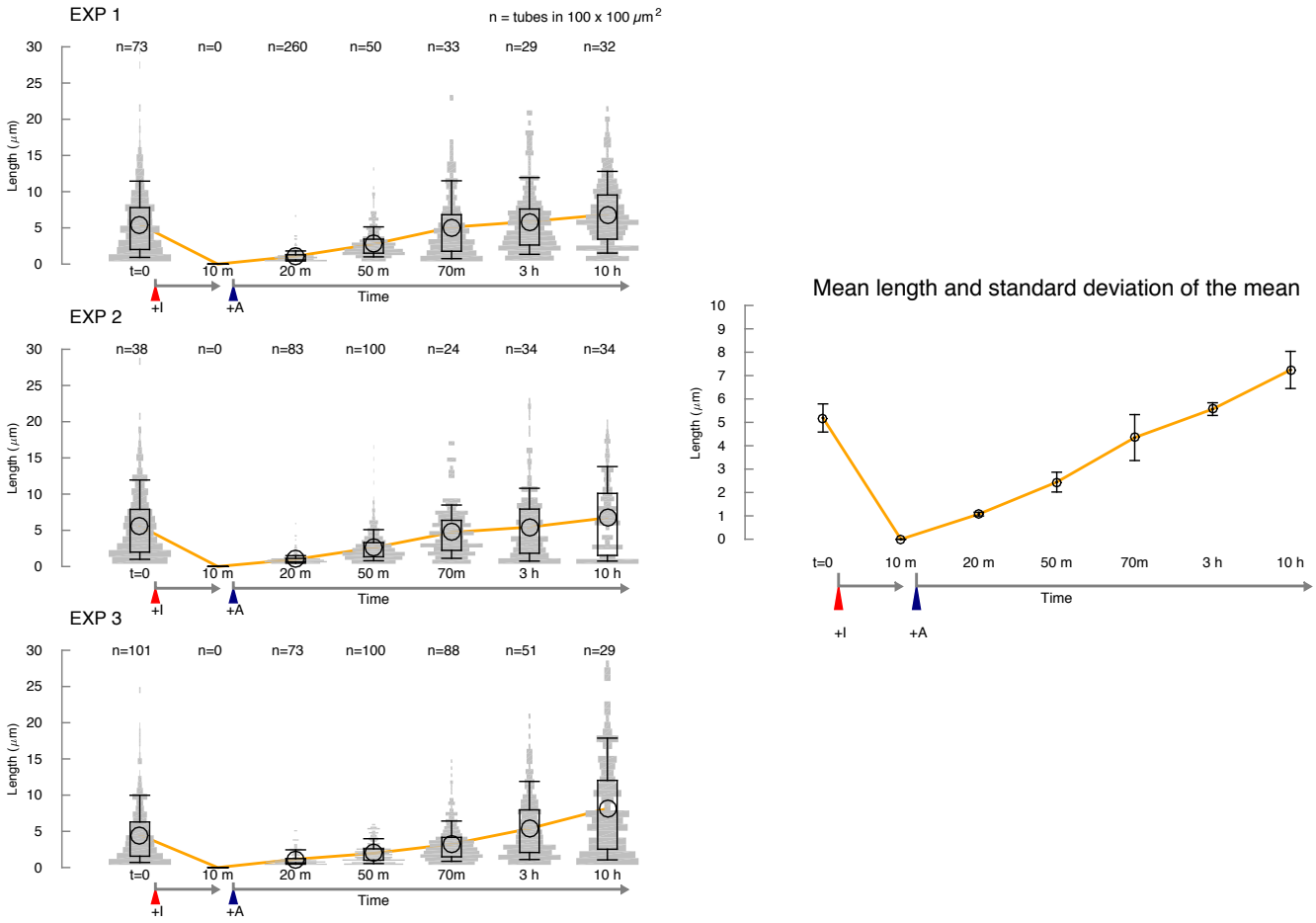

Figure 35: Invasion and anti-invasion of nanotubes assembled from tiles with 7 base-long sticky ends (100% toeholded tiles). *Addition of invader (marked by the red triangle) results in rapid disassembly of nanotubes (no nanotubes are visible in fluorescence microscopy images). When anti-invader is added (marked by the blue triangle) nanotubes regrow reaching a mean length which exceeds their initial mean length. In this case, binding of anti-invader to the sticky end of strand S4 seems to not contribute slower growth 4. Left: violin plots of each experiment. Right: mean and standard deviation of the mean for the experiments to the left.*

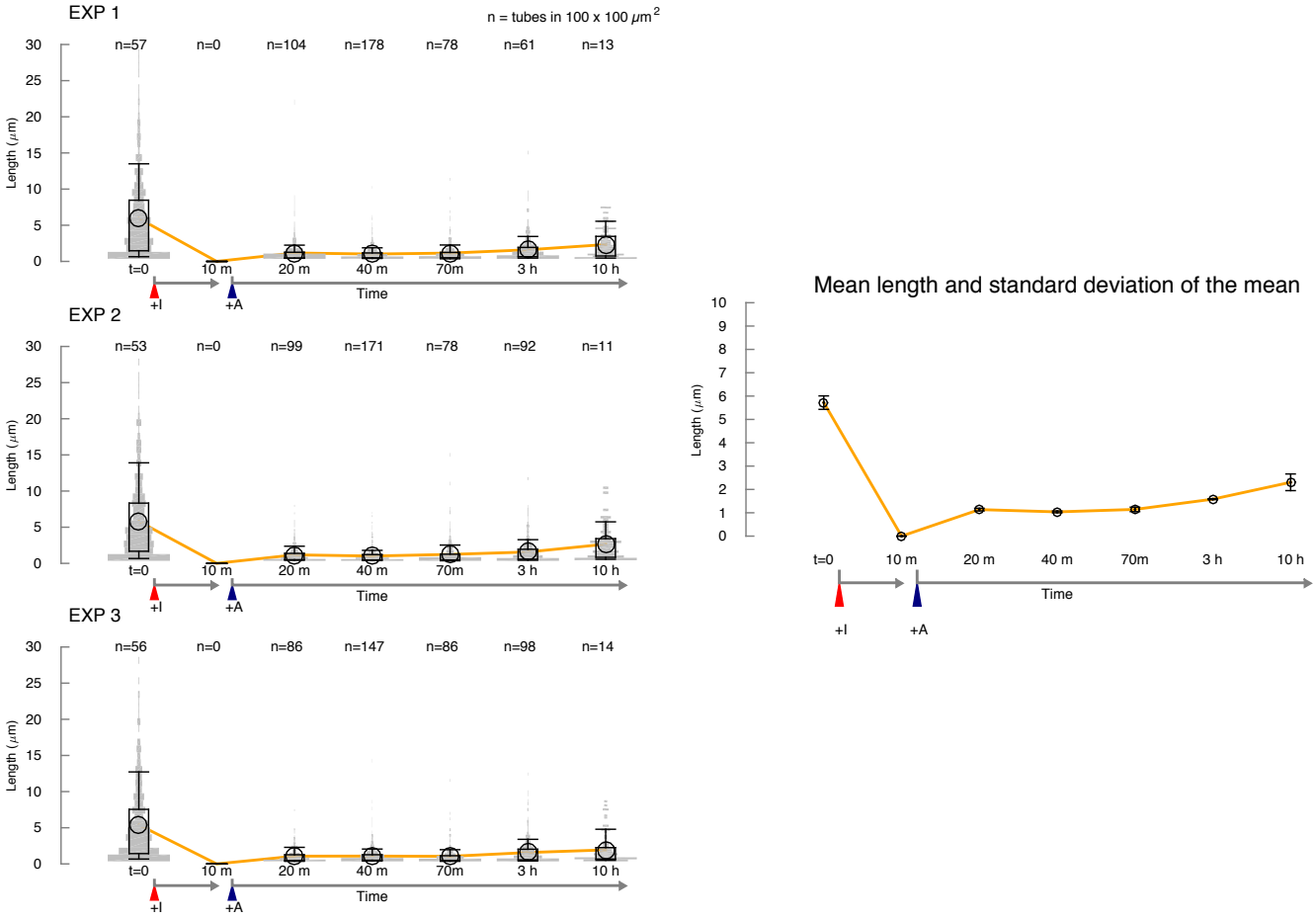

Figure 36: Invasion and anti-invasion of nanotubes assembled from tiles with 8 base-long sticky ends (100% toeholded tiles). *Addition of invader (marked by the red triangle) results in rapid disassembly of nanotubes (no nanotubes are visible in fluorescence microscopy images). When anti-invader is added (marked by the blue triangle) nanotubes regrowh reaching less than 50% the initial mean length. Limited regrowth may be due to two phenomena: 1) instability of the shortened tile arms, and 2) binding of anti-invader to one of the sticky ends of strand S4, which may form a stable complex in the 8 base-long sticky end tile as noted in Fig. 4. Left: violin plots of each experiment. Right: mean and standard deviation of the mean for the experiments to the left.*

4.11.1 T7 RNAP promotes disassembly of nanotubes

We designed DAE-E tiles that are stable in transcription mix and at 37°C by extending the length of their sticky ends to 7 and 8 bases. Nanotubes assembled from tiles having 7 base sticky ends are stable at 37°C and in transcription buffer, as shown in Fig. 37 A; however after addition of RNA polymerase and 30 minutes of incubation at 400 nM tile concentration and 37° C, the majority of tubes melt resulting in high contrast of fluorescence on surface of glass slide (background), and low number of tubes present in solution as shown in Fig. 37 B.

Nanotubes assembled from tiles having 8 base sticky ends are stable at 37°C in transcription buffer and in the presence of T7 RNA polymerase, as long as nanotubes are incubated at tile concentration exceeding 500-600 nM, as shown in Figs. 38 and 39.

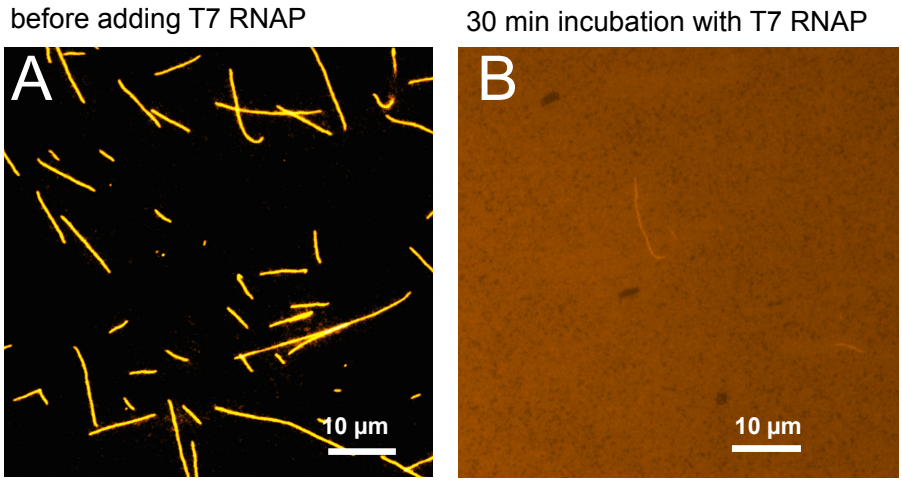

Figure 37: Nanotubes assembled from tiles with 7 base sticky ends are not stable when incubated with T7 RNAP *Nanotubes were annealed at 5 μM tile concentration, subsequently diluted to a 500 nM tile concentration and incubated in transcription buffer, at 37° C. A) Example image of nanotubes prior to addition of T7 RNA polymerase. B) Example image of nanotubes taken after 30 minutes addition of 10% (v/v) T7 RNA polymerase. Nanotubes annealed at higher tile concentration melt as well in the presence of T7 RNAP.*

4.11.2 8 base sticky end nanotubes are stable in the presence of enzymes and transcription conditions

Nanotubes annealed from tiles having 8 base sticky ends were annealed at 5 μM tile concentration in 1X transcription buffer, subsequently diluted in transcription mix (1x transcription buffer, 20 mM $MgCl_2$, and 20 mM NTPs) at various tile concentrations (400 nM, 750 nM and 2 μM) and incubated at 37°C (Fig. 38). Nanotubes incubated at 400 nM tile concentration melted after 15 hours at 37° C in RNA polymerase as shown in Fig. 38 A2. Nanotubes incubated at 750 nM and 2 μM tile concentration are stable in presence of RNA polymerase as shown in Fig. 38 B2 and C2. Nanotube length distributions for the 750 nM tile sample are shown in Fig. 39.

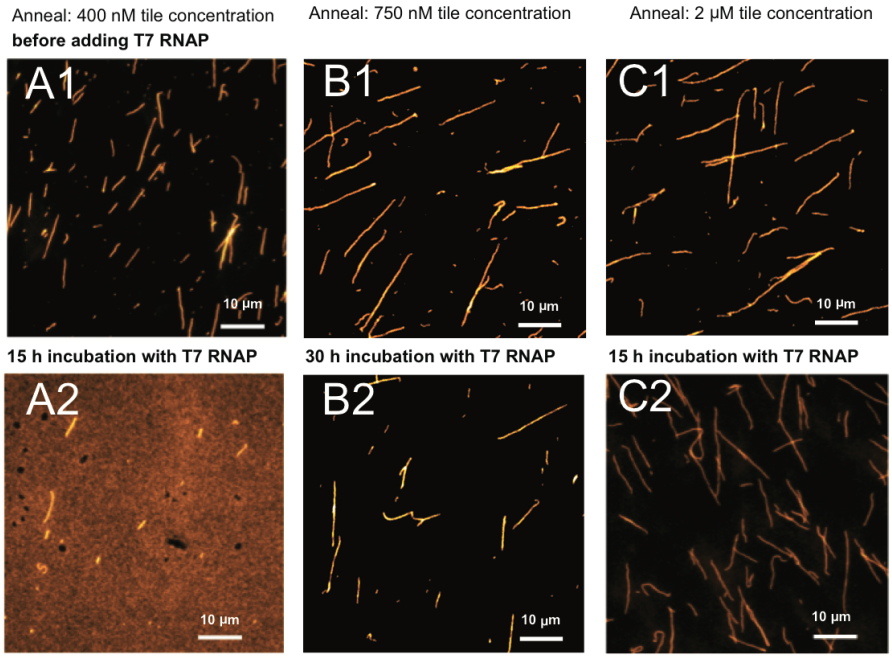

Figure 38: Nanotubes annealed from tiles having 8 base sticky ends are stable in the presence of T7 RNA polymerase at high tile concentration. *were annealed at 5 μM tile concentration in 1X transcription buffer, and subsequently diluted in transcription mix (1x transcription buffer, 20 mM $MgCl_2$, and 20 mM NTPs) including 10% (v/v) T7 RNA polymerase. A1, B1, C1: Example images of nanotubes at 400 nM, 750 nM, and 2 μM tile concentration respectively, prior to addition of T7 RNA polymerase. A2: Example image of nanotubes incubated at 400 nM tile concentration in the presence of RNAP for 15 hours . B2: Example image of nanotubes incubated at 750 nM tile concentration in the presence of RNAP for 30 hours. C2: Example image of nanotubes incubated at 2 μM tile concentration in the presence of RNAP for 30 hours.*

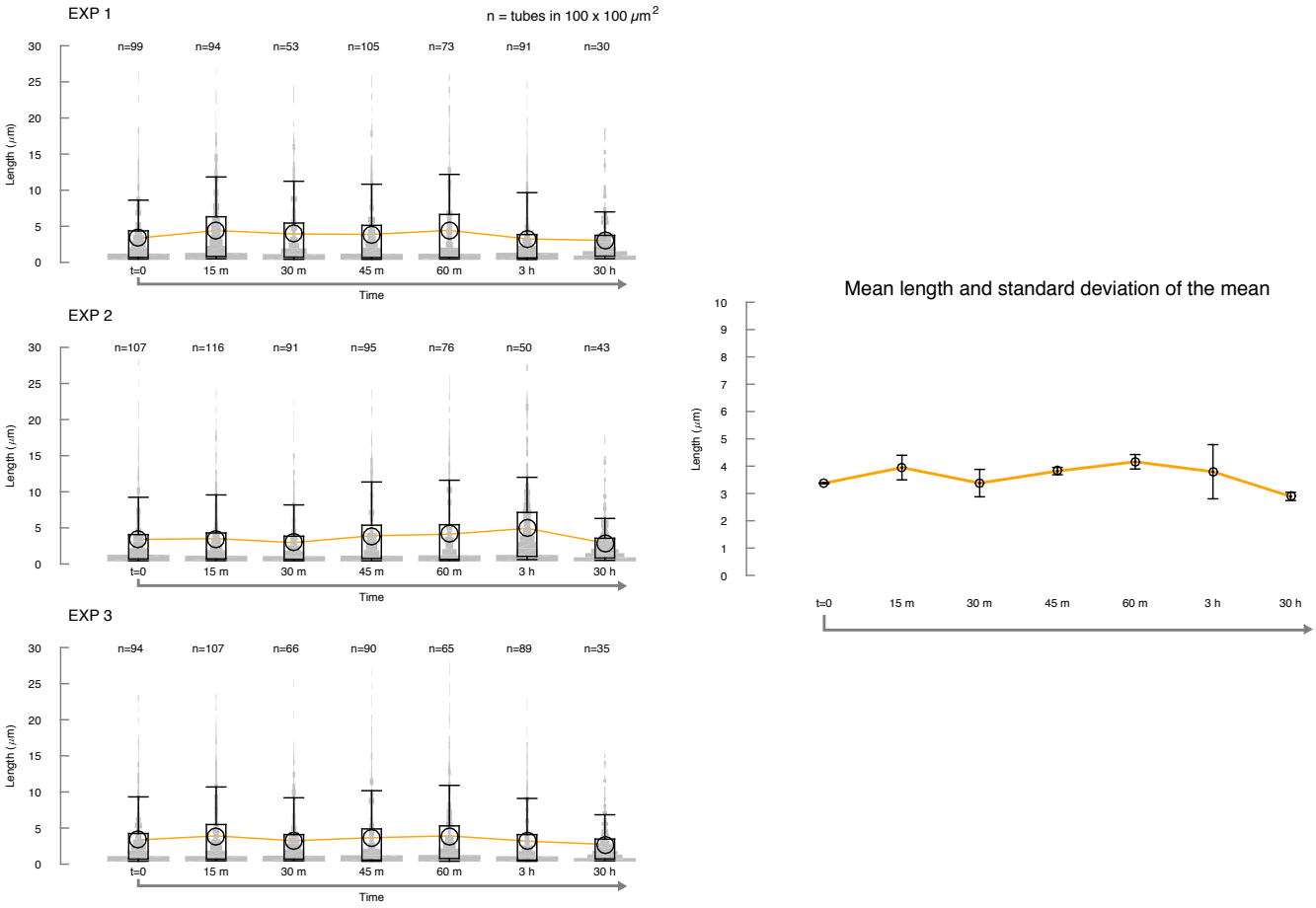

Figure 39: Nanotubes annealed from tiles having 8 base sticky ends are stable in the presence of T7 RNA polymerase at 750 nM tile concentration. *Nanotubes were incubated at 37° C in transcription mix, in the presence of 10% (v/v) T7 RNAP. Left: Violin plots of length distributions tracked over time. Right: Mean and standard deviation of the mean of the results shown in the left panel.*

4.11.3 Invasion and anti-invasion reactions of nanotubes with 8 base sticky ends: bulk fluorimetry

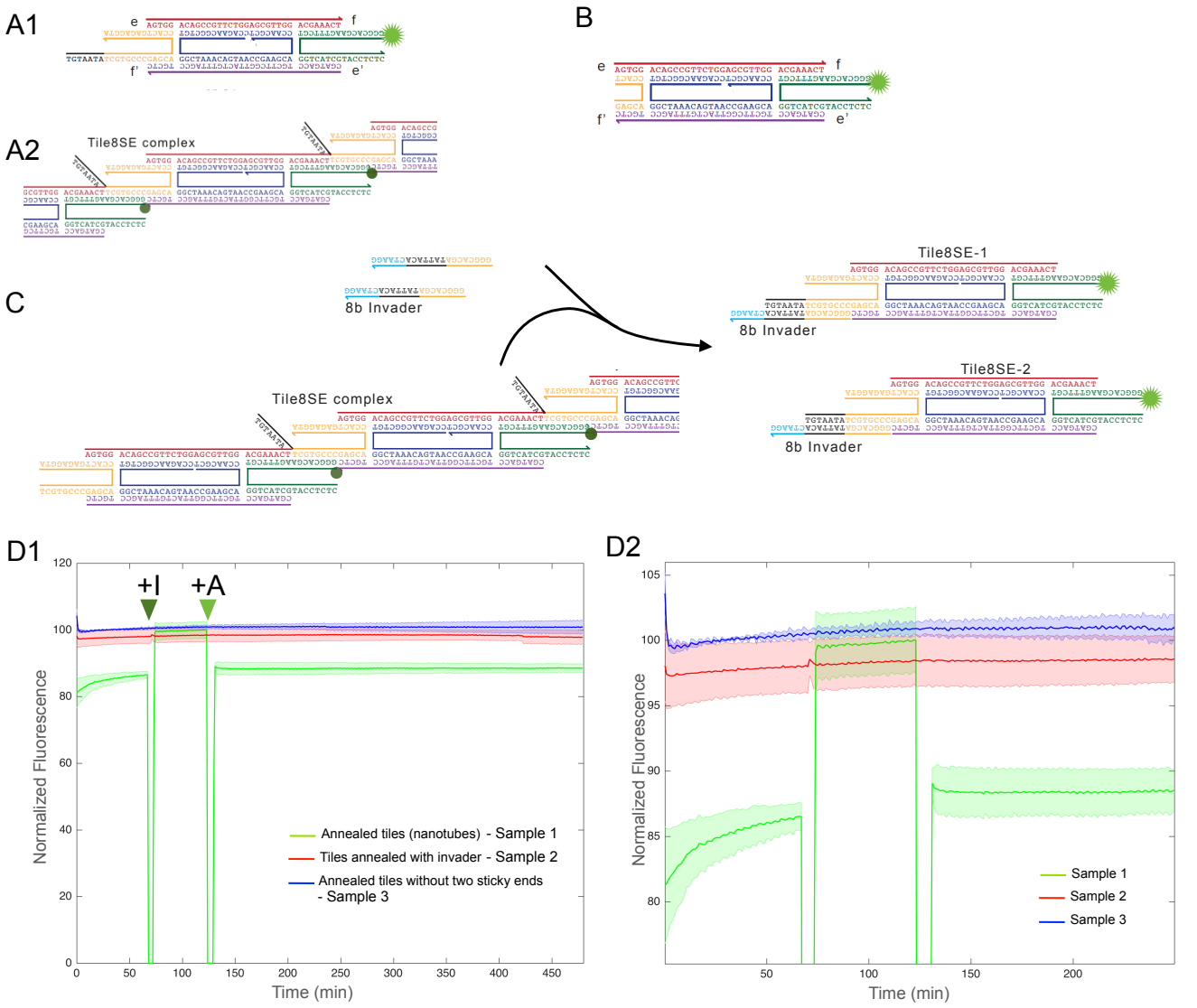

Figure 40: Monitoring invasion and anti-invasion reactions using bulk fluorimetry *A1: 8 base SE tiles were labeled with a TAMRA fluorophore on the 5' end of strand 4. A2: Fluorescence is quenched when strand 4 sticky ends form a double stranded complex (assembled tiles). B: Partially blunt-ended 8 base SE tile with truncated strand 2 (tiles cannot assemble). C: Invasion reaction results in disassembly of sticky ends and therefore increase in fluorescence. D: Bulk fluorimetry data showing that invaded tiles exhibit fluorescence nearly identical to that of partially blunt-ended tiles (that are unable to assemble) and to that of tiles annealed with invader strands. Addition of invader to Sample 1 is marked by the dark green triangle (+I), and addition of anti-invader to Sample 1 is marked by the light green triangle (+A).*

The fluorescence of a fluorophore attached to a single-stranded DNA can be altered upon its hybridization with a complementary DNA strand [23, 16]. Depending on the identity of the base pairs neighboring the fluorophore, the fluorescence either gets quenched or enhanced. We took advantage of this phenomenon to track polymerization of DNA tiles by placing fluorophores at the sticky-end. Fig. 40 A1 shows the placement of TAMRA dye on the 8 base sticky end DNA tile (Fig. 1 C). Upon hybridization of the sticky ends, the adjacent G-C base pairs causes quenching of TAMRA fluorescence (Fig. 40 A2).

For characterizing the polymerization and depolymerization of DNA tiles using this technique, we annealed and compared the fluorescence of three samples. Sample 1: The tile shown in Fig. 40 A1 was annealed by itself. Sample-2: The tile in Fig. 40 A1 was annealed together with the invader strand (Fig. 40 A2). Sample-3: We annealed the partially blunt-ended tile in Fig. 40 B; the modified tile lacks two sticky ends and therefore cannot polymerize. We annealed the samples at 5 μM tile concentration in 1x transcription buffer as described in Section 3.1. For Sample 2, the invader was added at 10% excess before annealing. Annealing Sample 1 results in nanotubes, Sample 2 results in invaded tiles and Sample 3 is a control for fluorescence of free monomers. After annealing, the samples were diluted to 1 μM tile concentration in a solution containing 1x transcription buffer, 24 mM additional $MgCl_2$, 7.5 mM NTPs (each). This condition is similar to the oscillator-nanotube coupling buffer conditions (Section 4.13). By comparing the fluorescence of these three samples we can compare the effectiveness of invasion and anti-invasion reactions in typical oscillator coupling conditions.

We performed triplicate fluorescence measurements as described in Section 3.2 and 3.7. Figs. 40 D1 and D2 shows the mean and standard deviation of the mean of each triplicate experiment. Sample 1 (green trace) was allowed to stabilize for 70 minutes at 37° C; the moderate increase of the measured fluorescence indicates that the depolymerization rate of nanotubes is increased when the sample is heated from room temperature to 37° C. After 70 minutes, 10% stoichiometric excess (to tile strands) of invader was added to Sample 1; 55 minutes after addition of invader, 20% stoichiometric excess of anti-invader (compared to tile strands) was added to Sample 1. Raw fluorescence measurements were normalized relative to Sample 3 (free monomer fluorescence) as detailed in Section 3.8. Fig. 40 D2 is zoomed version of the plot shown in Fig. 40 D1.

Comparison of fluorescence of samples in Fig. 40 D1 shows that fully formed tubes (Sample 1, green) exhibit significantly lower fluorescence than invaded tubes (Sample 2, red) and the control tiles (Sample 3, blue). This observation is consistent with our expectation that upon hybridization, the fluorescence of TAMRA is quenched. Further, the invaded tiles have fluorescence very close to that of control tiles or free monomers. This observation suggests that, upon invasion, almost all of the sticky-ended interactions are broken. When the invader is added to Sample 1, the fluorescence quickly jumps to values close to that of free monomers, suggesting that the breakage of sticky-ended interaction happens very fast. Upon addition of anti-invader to the invaded Sample 1, the fluorescence drops quickly. Our earlier microscopy results show that upon anti-invasion, tubes are visible only after 30-60 minutes. So the quick drop in fluorescence in this experiment suggests that the tiles start interacting with each other very quickly after anti-invasion, but it takes time for the tubes to grow to lengths that are visible under the optical microscope.

4.12 Nanotube disassembly and reassembly via a cotranscribed RNA invader and RNase H

We tested two reactions where invasion and anti-invasion are fueled by enzymes. The first reaction is cotranscriptional invasion of nanotubes directed by an individual synthetic gene, that produces an RNA molecule designed to work as an invader. Nanotubes were annealed from 8 base sticky end tiles in 1X transcription buffer and mixed with genelet and transcription mix at 1 μM tile concentration. Genelet strands were separately annealed and mixed at 87.5 nM concentration with the transcription reaction mix (1x transcription buffer, 20 mM rNTPs and 14 mM $MgCl_2$). The transcription mix was equilibrated at 37° C for 15 minutes, and then T7 RNAP (10% v/v), PPase (3% v/v), and RNAase H (2% v/v) enzymes were added to the mix. Transcription of RNA invader was activated by adding to the solution the ssDNA activator A1 125 nM concentration (A1 hybridizes to the incomplete T7 promoter on the non-template strand of the genelet), and to transcribe RNA invader strander for a total of 30 hours. After 60 minutes of reaction, nanotubes were completely broken, as shown in Fig. 41. Reaction schemes are shown in Section 2.5.

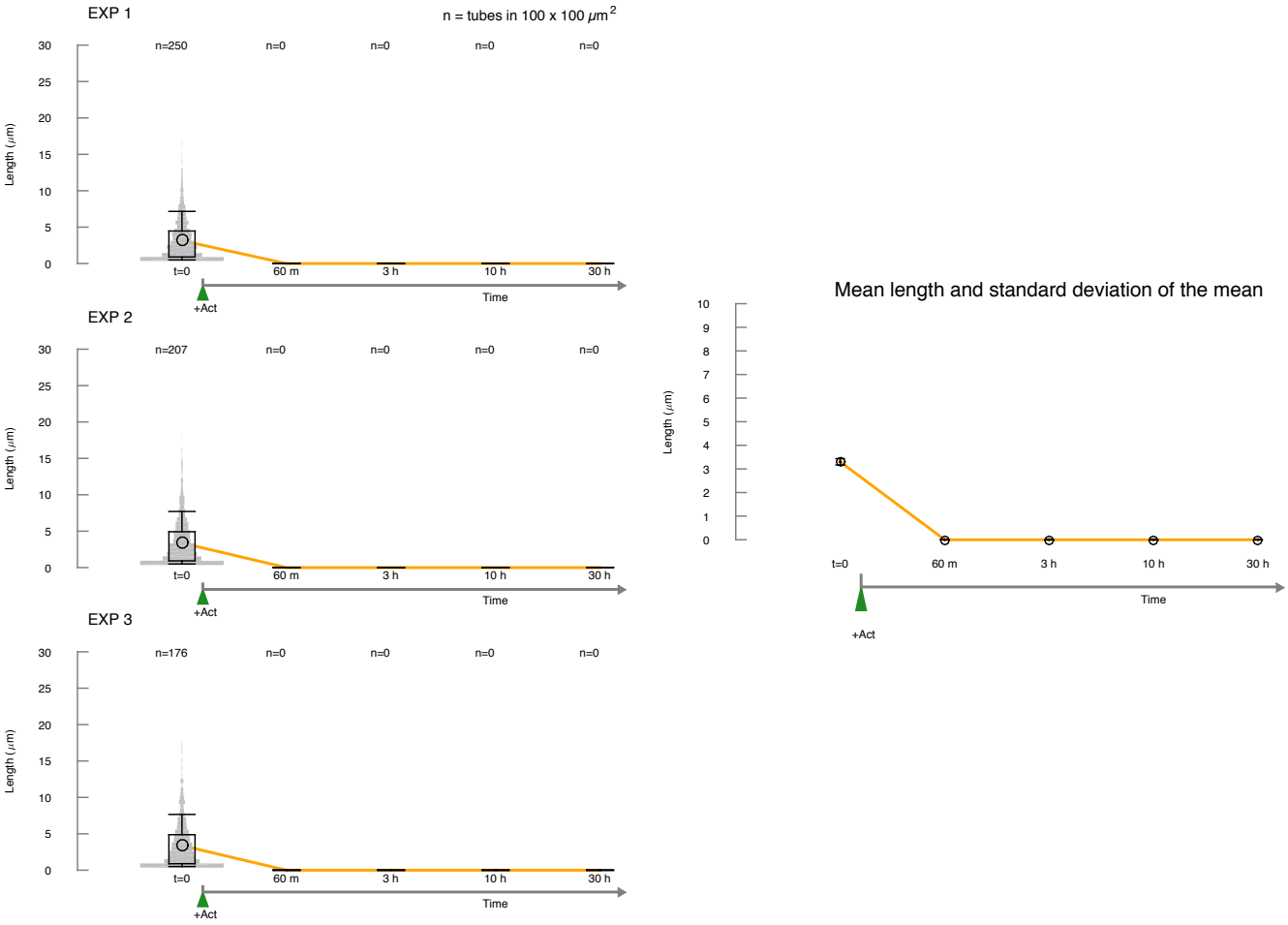

Figure 41: Co-transcriptional invasion mediated by RNA *Left: violin plots of each experiment. Right: mean and standard deviation of the mean for the experiments to the left.*

The second reaction tests RNase H mediated reactivation of tiles bound to invader (RNase H degrades RNA bound to DNA). Nanotubes were annealed from 8 base sticky end tiles in 1X transcription buffer and mixed with genelet and transcription mix at 1 μM tile concentration. Genelet strands were separately annealed and mixed at 87.5 nm concentration with the transcription reaction mix (1x transcription buffer, 20 mM rNTPs and 14 mM $MgCl_2$). The transcription mix was equilibrated at 37° C for 15 minutes, and then T7 RNAP (10% v/v), PPase (3% v/v), and RNAase H (2% v/v) enzymes were added to the mix. Transcription of RNA invader was activated by adding to the solution the ssDNA activator A1 125 nM concentration (A1 hybridizes to the incomplete T7 promoter on the non-template strand of the genelet), and allowed to react for 30 minutes in presence of RNase H. After 30 minutes, transcription of RNA invader was stopped by adding 150 nM of inhibitor strand dI1, which displaces A1 from the promoter region. As transcription is turned off, RNase H-mediated degradation dominates, resulting in reactivation of individual tiles and tube reassembly (reaction schemes are shown in Fig. 6, Section 2.5). Violin plots and mean nanotube length plots measured in these experiments are shown in Fig. 42.

Both reactions were tested at concentrations of T7 RNA polymerase and RNase H comparable to those used in the transcriptional oscillator experiments previously described by [11], [6], and [25].

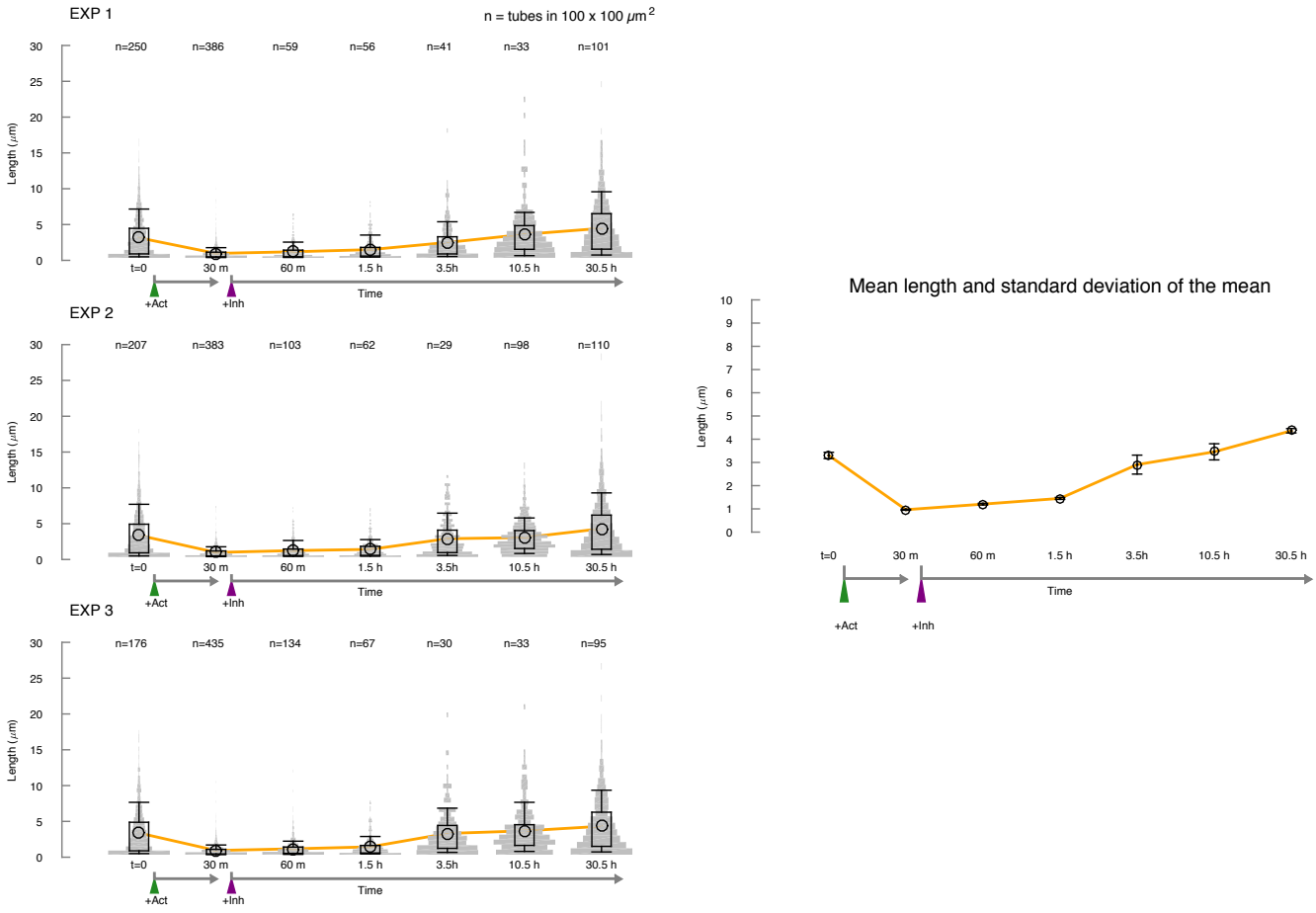

Figure 42: Co-transcriptional invasion mediated by RNA, and RNase H-mediated anti-invasion of nanotubes assembled from 8 base-long sticky end tiles. *Left: violin plots of each experiment. Right: mean and standard deviation of the mean for the experiments to the left.*

4.12.1 Temporal control of invasion by activating and deactivating a synthetic template is hampered by undesired transcriptional activity of RNAP

We tested if nanotube disassembly and reassembly can be achieved by subsequent activation and deactivation of a synthetic template in the presence of RNAP and RNAse H. We refer again to the reaction schemes in Fig. 6, Section 2.5. Samples were prepared consistently with the protocol outlined earlier in this section, using 37 nM template (Insulator), 1022 units of RNAP (Cellscript), 6 units of RNase H (Promega). As shown in Fig. 43 A, active template produces invader that rapidly breaks nanotubes; as inhibitor is added (in slight excess with respect to the concentration of template), production of invader is reduced. RNase H degradation of invader bound to tiles thus dominates, and promotes reactivation of tiles and nanotube reassembly. Yet, re-activation of template, by adding excess activator strand, does not result in significant nanotube disassembly, rather a stall in growth. Even when the concentration of template (and activator) is increased, the nanotube mean length does not significantly decrease.

We hypothesized that loss of RNAP activity may be the reason why production of invader is insufficient to promote nanotube disassembly. However, this hypothesis is not supported by the fact that nanotubes in the presence of active template never regrow even after 30 hours of incubation (Fig. 41), although RNAP activity should drastically decrease after 8-10 hours, while RNAse H activity remains high for much longer [11].

The fact that RNAP activity loss does not hamper the second cycle of cotranscriptional invasion is confirmed by an experiment in which, after addition of inhibitor and activator, we attempted to restore disassembly by adding a fresh aliquot of 600 units of RNAP (Cellscript), and later additional 250 units of RNAP (NEB), as shown Fig. 43, bottom. These additional aliquots were not sufficient to restore disassembly. However, final addition of 0.7 picomoles of active template promotes nanotube disassembly.

We have recently shown that RNAP can transcribe a variety of RNA products from DNA nanotubes [20], and that these products can mediate nanotube disassembly via strand invasion of the sticky ends in particular when a toehold is present on the tiles, like in this case. In [20], however, the 8 base sticky end nanotube variant we consider here was shown to be robust to RNAP-mediated disassembly. Thus, we formulate the hypothesis that a subset of RNA products transcribed by RNAP from the nanotubes either interacts with the toehold of the tiles, or with the invader molecules. These interactions could prevent invasion from occurring with the speed and efficiency observed in nanotubes that were not previously incubated with RNAP. If this hypothesis is correct, also a DNA invader would be slower and less efficient in disassembling nanotubes that have been incubated with RNAP and transcription components. The results of this experiments are shown in Fig. 44: DNA invader was added to DNA nanotubes previously incubated for 6 hours in our standard transcription conditions or in a control (non-transcribing) solution in which NTPs were replaced by ATP only (to maintain the same ionic balance [20]). RNase H was present in both samples. Invasion in the ATP-only mix reaches completion within 20 minutes, while invasion in the NTP-mix proceeds more slowly maintaining a higher mean length. The mean number of nanotubes per image also transiently increases at the 20 minute mark in the NTP-mix sample, indicating that many long nanotubes persist in solution despite the presence of invader. Example representative images are shown in Fig. 45.

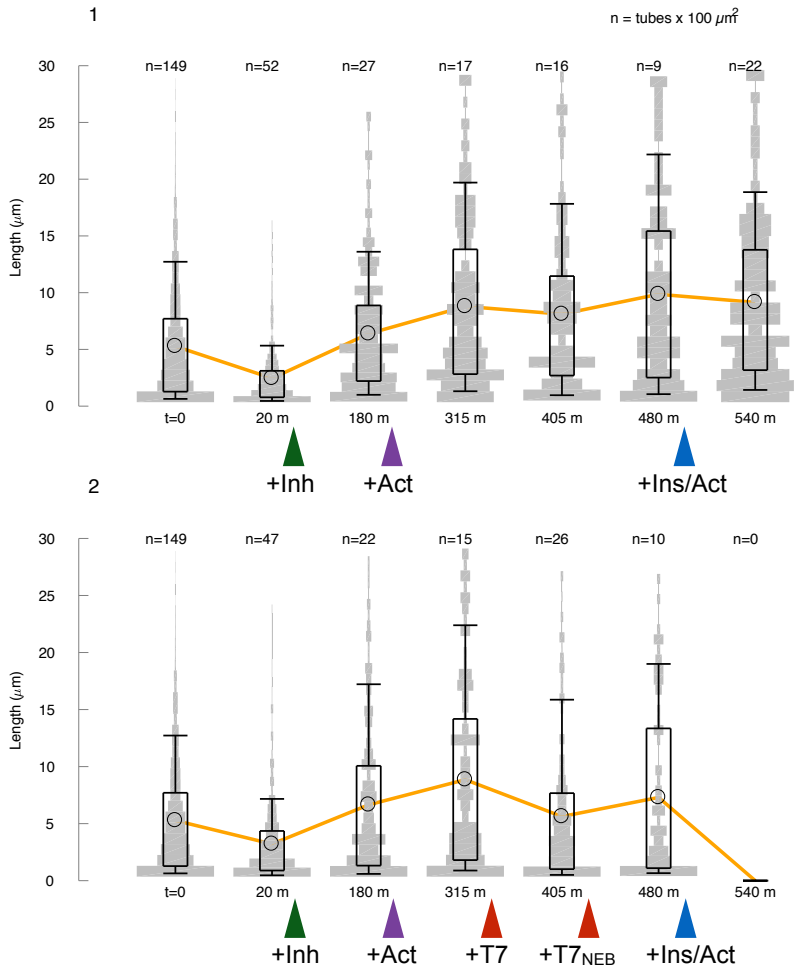

Figure 43: Activation and deactivation of template producing invader for 8 base-long sticky end tiles.

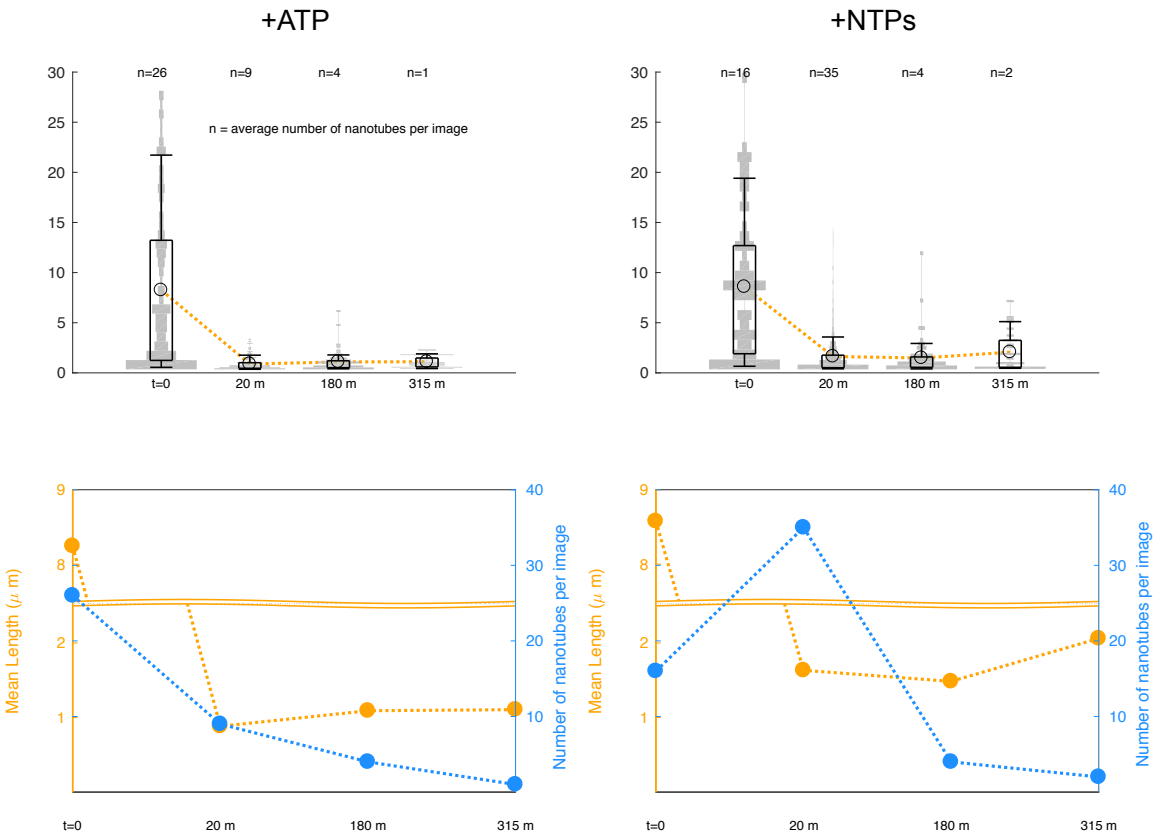

Figure 44: Invasion is slower on nanotubes that were incubated with RNA polymerase and transcription components.

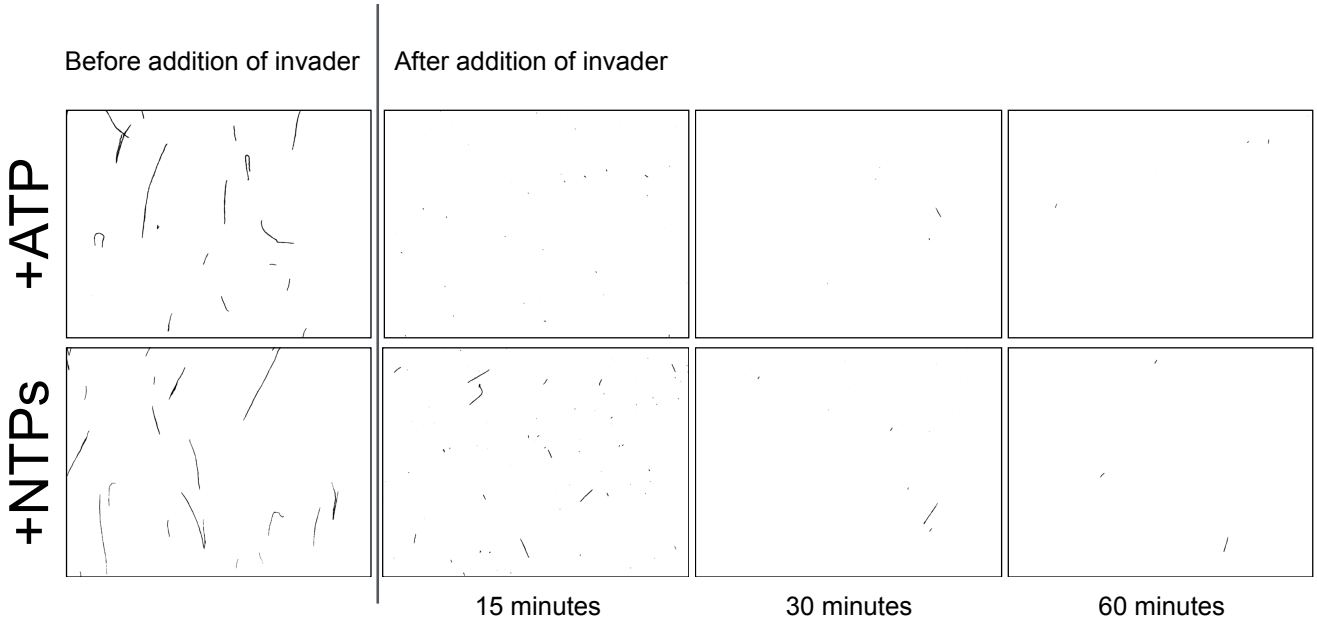

Figure 45: Example images: invasion is slower on nanotubes that were incubated with RNA polymerase and transcription components.

4.13 Directing nanotube disassembly and reassembly using a synthetic transcriptional oscillator

The oscillator was tuned to operate in a regime of high RNase H concentration, because RNase H is needed to promote nanotube regrowth by degrading RNA invader bound to the tiles. Obtaining large amplitude oscillations in this regime requires an increase in RNAP concentration [22]. Amplitude is defined as the peak-well difference in T21 fluorescence, corresponding to the on-off state of switch S21; this amplitude is directly proportional to the on-off ratio of the insulator as well, which is has the same activation/inhibition domains of T21. Activity of genelet T21 was tracked by labeling T21 non-template strand with TYE665, and A1 with Iowa Black quencher as done in previous reports [11, 6]. Fluorescence of T21 was tracked analyzed using Horiba Jobin Yvon Fluorolog 3 system as described in Section 3.7. Nanotube length distributions were assessed by imaging samples from the bulk solution with a fluorescence microscope (see Section 3.3); samples were taken at time stamps specified in each figure.

Amplitude and frequency in this molecular oscillator cannot be independently tuned [22]: large amplitude correlates with a large (slow) oscillation period. In addition, there is significant variability in the achievable oscillator behavior depending on the lot of RNAP and RNase H. As a result of these two challenges, our experiments focus on only two operating points: in the first we obtained a single, slow oscillation with large amplitude followed by a slow drift to a steady state; in the second, we tuned the circuit to exhibit two faster oscillations. In all our experiments, we used RNAP from a single lot (Rp-Lot 1), and RNase H from three different lots (Rh-Lot 1, Rh-Lot 2, and Rh-Lot 3).

Oscillator sequences were premixed in a DNA stock solution containing: 1x transcription buffer, 20 mM rNTPs, 14 mM $MgCl_2$, and annealed 8 base sticky end nanotubes. To control nanotube assembly and disassembly via oscillator inputs and outputs, RNA invader genelet activated by oscillator strand A1 was added to the solution. Experimental repeats were done using the same enzyme batches; in some cases the same master mix was used for repeats, in others distinct master mixes were prepared by different experimenters. We found that distinct master mixes yield very consistent results as long as pipetting and mixing techniques are consistent.

Experiment round 1 (R1): These experiment were done using a single lot of RNAP (Rp-Lot 1) and RNase H (Rh-Lot 1, Thermofisher). The final concentrations of the oscillator strands were: T12 120 nM; T21 250 nM; dI1 600 nM, A1: 250 nM in the absence of insulator, 320 nM in the presence of insulator; A2 600 nM; insulator template (when present) 65 nM. T7 RNAP 10% (v/v), PPase 3% (v/v), and RNase H 2% (v/v) (Rh-Lot 1).

Experiment round 1 (R2): These experiments were done using a single lot of RNAP (Rp-Lot 1) and RNase H (Rh-Lot 2, Thermofisher). The final concentrations of the oscillator strands were: T12 120 nM; T21 250 nM; dI1 700 nM, A1: 250 nM in the absence of insulator, this concentration was adjusted to 250+X nM in the presence of X nM insulator template; A2 600 nM; the insulator template concentration was varied as specified in each experiment below. T7 RNAP 10% (v/v) (Rp-Lot 1), PPase 2.6% (v/v), and RNase H 2.75% (v/v) (Rh-Lot 2).

Experiment round 3 (R3): The third round was done using 8b SE nanotubes with strand variants SE4-TAMRA and SE3-NoDye (Table 3, Fig. 1 D), which helped suppress nanotube growth in oscillator conditions. single lot of RNAP (Rp-Lot 2) and RNase H (Rh-Lot 3, Promega). The final concentrations of the oscillator strands were: T12 120 nM; T21 250 nM; dI1 800 nM, A1: 250 nM in the absence of insulator, this concentration was adjusted to 250+X nM in the presence of X nM insulator template; A2 800 nM; the insulator template concentration was varied as specified in each experiment below. T7 RNAP 10% (v/v) (Rp-Lot 1), PPase 2.6% (v/v), and RNase H 4.2% (v/v) (Rh-Lot 3).

4.13.1 Round 1 experiments

Here we report violin plots and individual oscillator traces. The mean and standard deviation of nanotube length and active T21 concentration as a function of time are plotted in Fig. 5 of the main paper.

We note that, even in the presence of insulator, the oscillator behavior is perturbed as the total concentration of tiles increases. This is presumably due to two phenomena: depletion of RNase H degrading RNA invader bound to tiles, and non-specic binding of RNA polymerase to nanotubes and tiles.

Control experiment: oscillator and nanotubes in the absence of of insulator This experiment was conducted using experimental conditions defined as in experiment rounds R1, in the absence of insulator template.

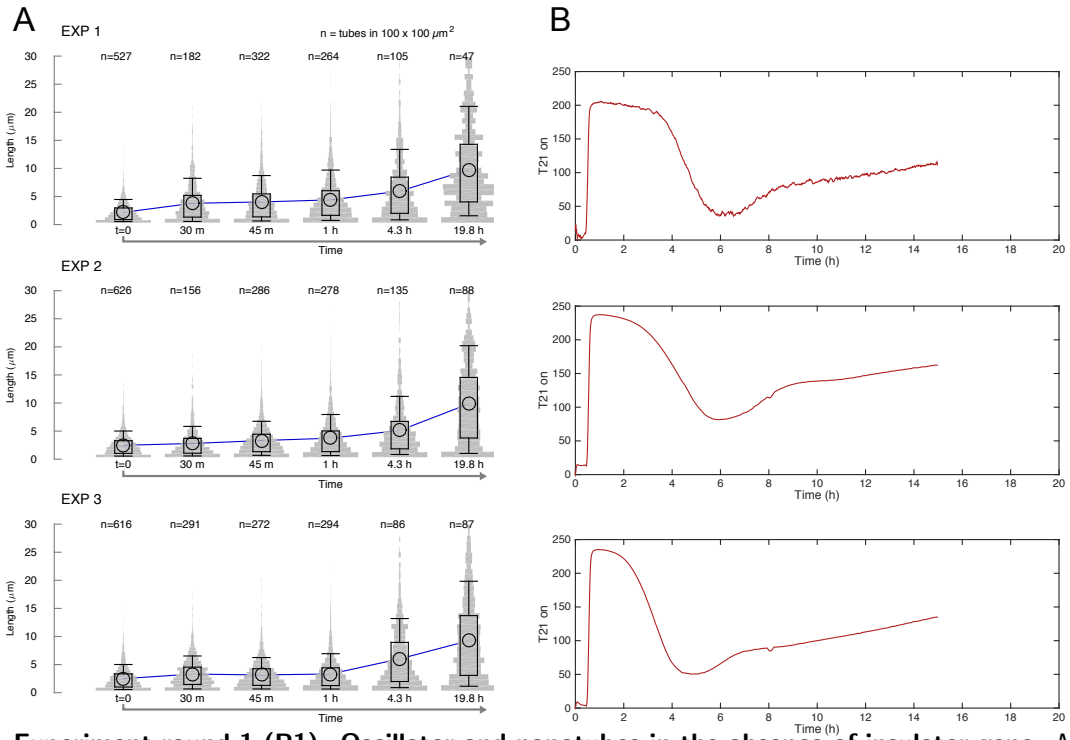

Figure 46: Experiment round 1 (R1). Oscillator and nanotubes in the absence of insulator gene. *Nanotubes at 1 μM tile concentration were incubated in the same sample as the oscillator reaction, in the absence of insulator gene (which directs co-transcriptional invasion by producing an RNA invader). In these conditions, the nanotube mean length increases over time exceeding the mean length measured in control experiments (Fig. 42). Left: Violin plots of nanotube length distributions. Right: Corresponding normalized oscillator traces (fraction of active T21).*

Oscillator directing nanotubes: 750 nM tile concentration

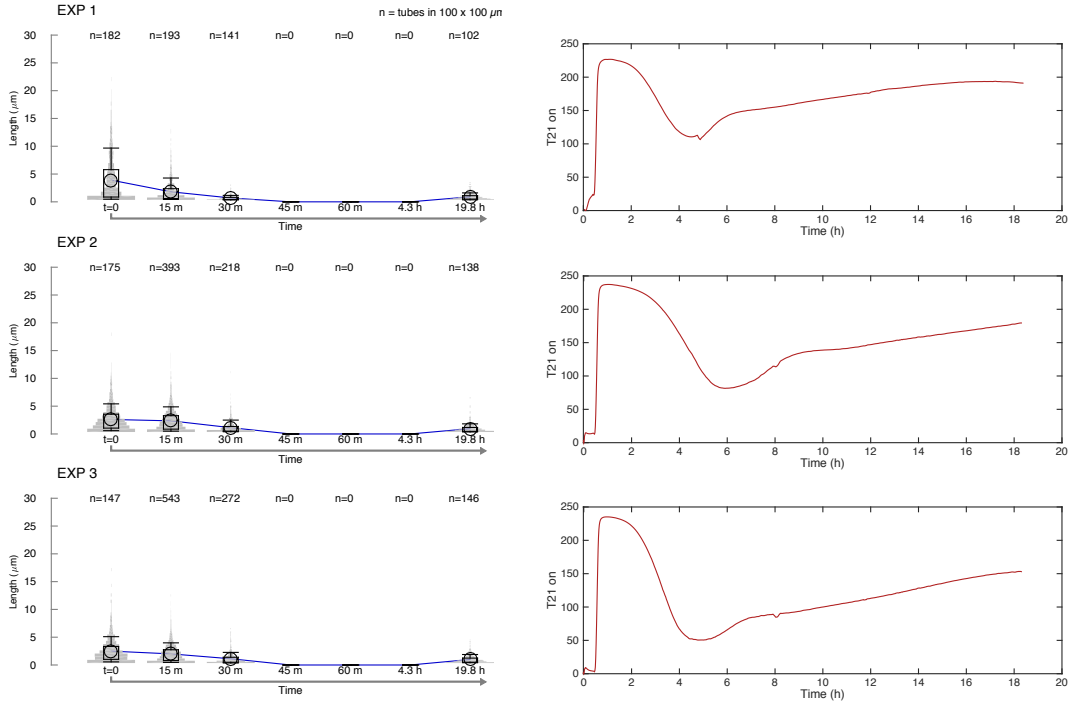

Figure 47: Nanotube growth directed by the oscillator circuit; 750 nM total tile concentration. *Nanotubes annealed from a total concentration of 750 nM tiles were incubated in the same sample as the oscillator reaction in the presence of insulator gene (which directs co-transcriptional invasion by producing an RNA invader). In these low-monomer concentration conditions, nanotubes quickly break after starting the reactions yet regrowth (mediated by RNase H) is suppressed presumably due to the low monomer concentration. Left: Violin plots of nanotube length distributions. Right: Normalized oscillator traces (fraction of active T21).*

Oscillator directing nanotubes: 1000 nM tile concentration

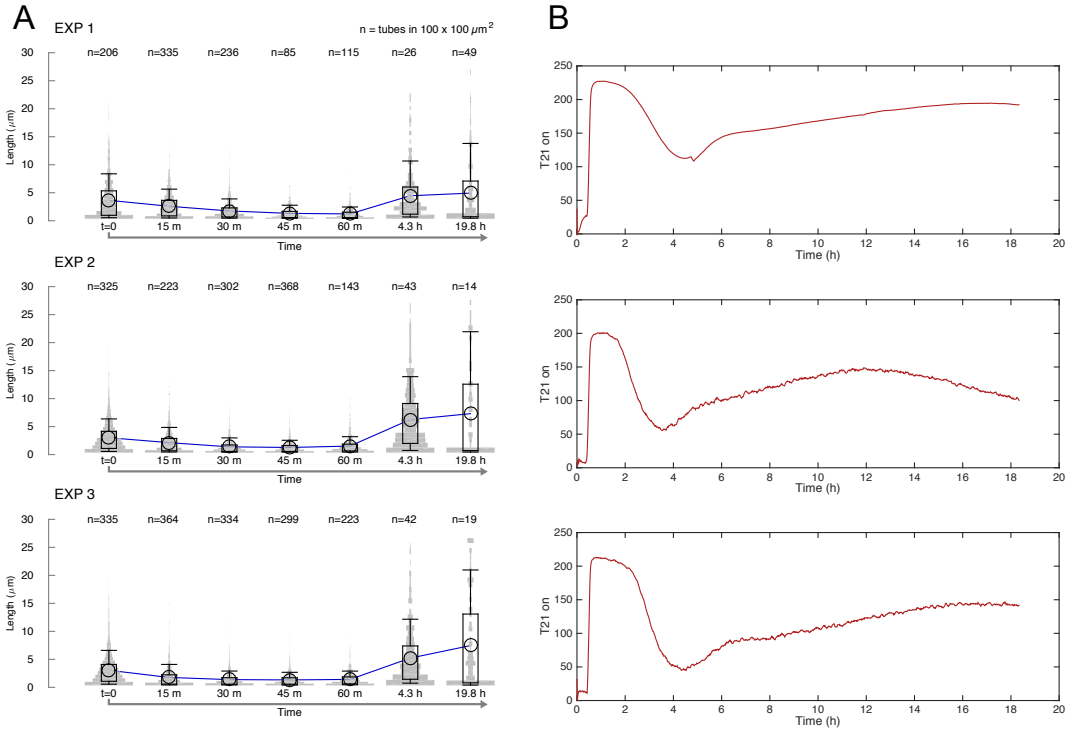

Figure 48: Nanotube growth directed by the oscillator circuit; 1000 nM total tile concentration. *Nanotubes annealed from a total concentration of 1000 nM tiles were incubated in the same sample as the oscillator reaction in the presence of insulator gene (which directs co-transcriptional invasion by producing an RNA invader). Nanotubes break after starting the oscillator reaction by adding enzymes when the insulator is active. When T21 turns off, the insulator activity is also reduced; this means that RNase H degradation dominates over production of invader, and nanotube regrowth is promoted. Left: Violin plots of nanotube length distributions. Right: Corresponding normalized oscillator traces (fraction of active T21).*

Oscillator directing nanotubes: 1500 nM tile concentration

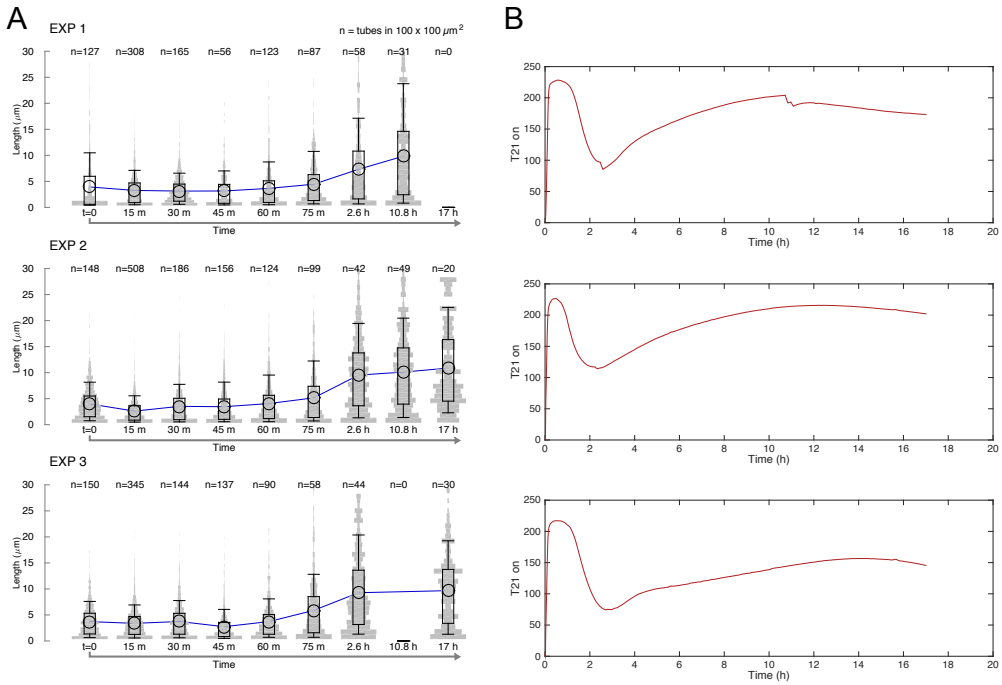

Figure 49: Nanotube growth directed by the oscillator circuit; 1500 nM total tile concentration. *Nanotubes annealed from a total concentration of 1500 nM tiles were incubated in the same sample as the oscillator reaction in the presence of insulator gene (which directs co-transcriptional invasion by producing an RNA invader). After the oscillator reaction starts (addition of enzymes) the insulator is active, yet breakage is not effective presumably due to the high concentration of tiles, but growth is halted until T21 begins to be turned off. When T21 turns off, the insulator activity is also reduced, and less invader is produced. RNase H degradation dominates over production of invader, and facilitates rapid growth of nanotubes. Left: Violin plots of nanotube length distributions. Right: Corresponding normalized oscillator traces (fraction of active T21).*

4.13.2 Round 2 experiments

Here we report violin plots and individual oscillator traces. The mean and standard deviation of nanotube length and active T21 concentration as a function of time are plotted in Fig. 5 of the main paper, unless otherwise noted.

Oscillator directing nanotubes: 1000 nM tile concentration, 70 nM insulator

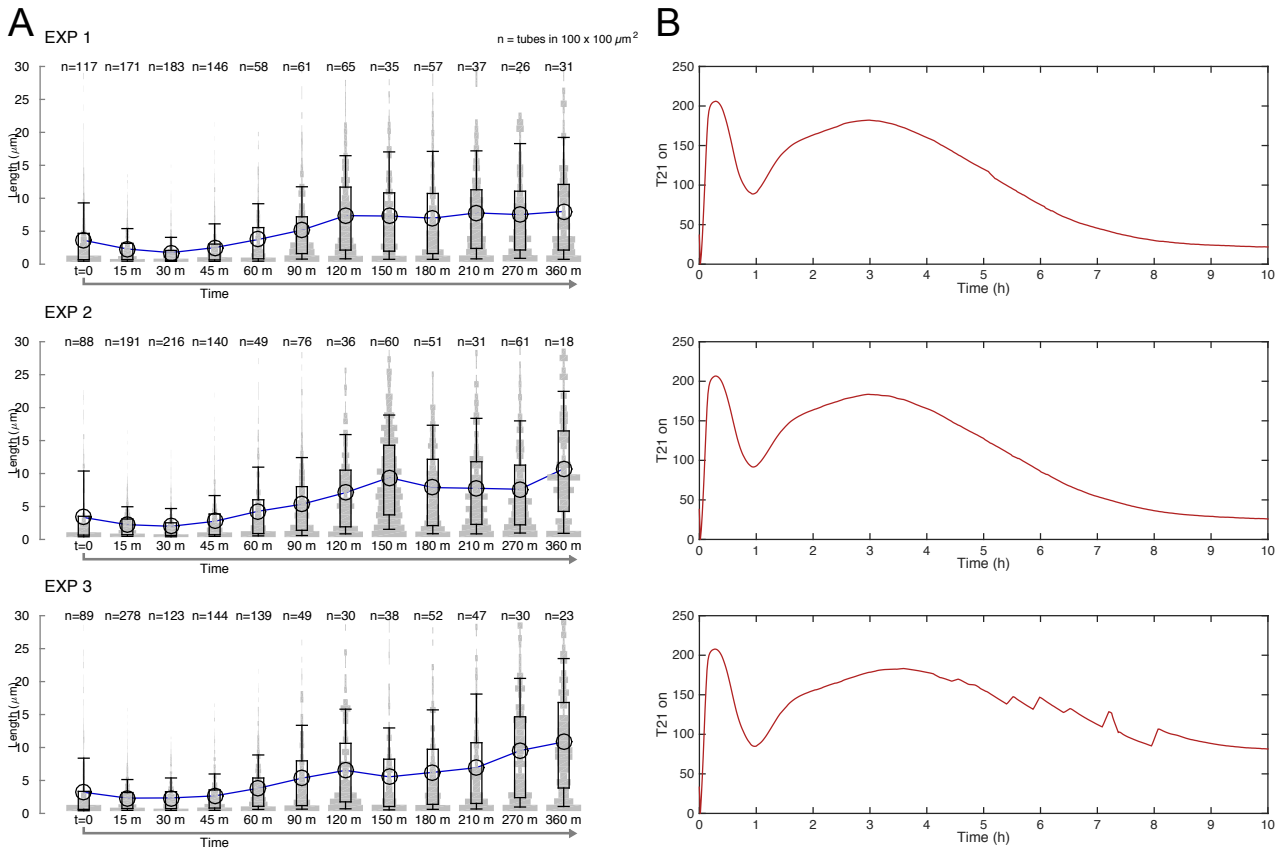

Figure 50: Nanotube growth directed by the oscillator circuit; 1000 nM tile concentration, 70 nM insulator. *Nanotubes annealed from a total concentration of 1000 nM tiles were incubated in the same sample as the oscillator reaction in the presence of 70 nM insulator gene (which directs co-transcriptional invasion by producing an RNA invader). Left: Violin plots of nanotube length distributions. Right: Corresponding normalized oscillator traces (fraction of active T21).*

Oscillator directing nanotubes: 1000 nM tile concentration, 100 nM insulator

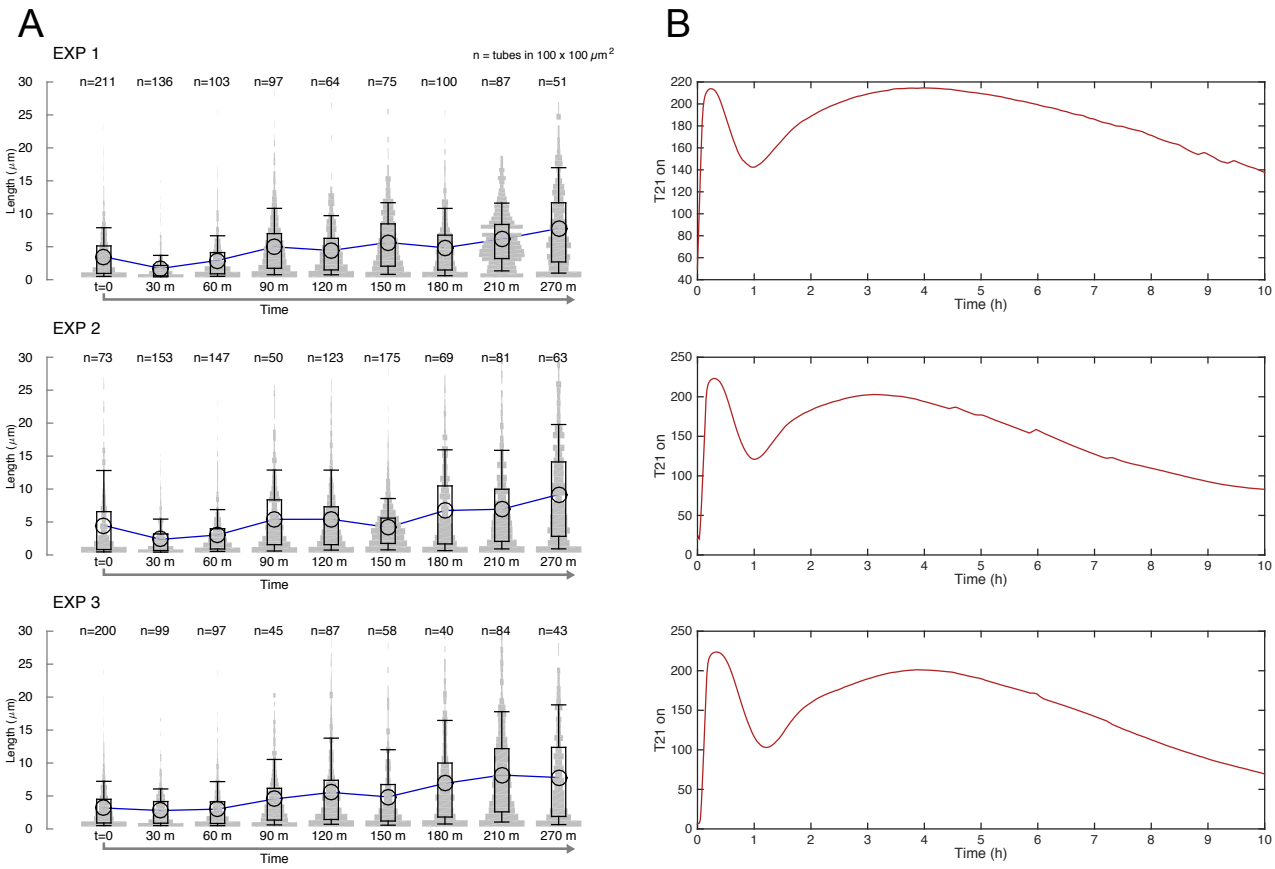

Figure 51: Nanotube growth directed by the oscillator circuit; 1000 nM tile concentration, 100 nM insulator. *Nanotubes annealed from a total concentration of 1000 nM tiles were incubated in the same sample as the oscillator reaction in the presence of 100 nM insulator gene (which directs co-transcriptional invasion by producing an RNA invader). Left: Violin plots of nanotube length distributions. Right: Corresponding normalized oscillator traces (fraction of active T21).*

Oscillator directing nanotubes: 1000 nM tile concentration, insulator titration

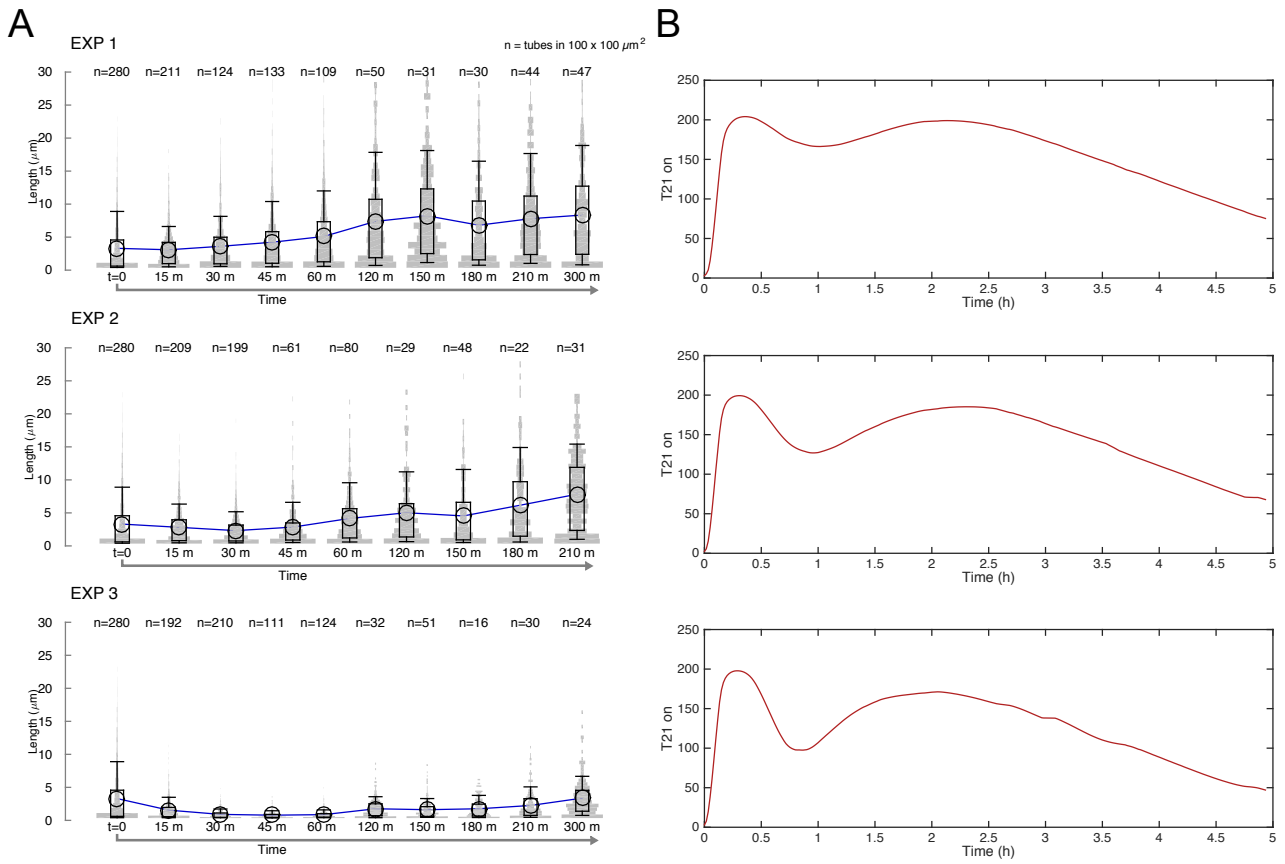

Figure 52: Nanotube growth directed by the oscillator circuit; 1000 nM tile concentration, varying concentration of insulator. *Nanotubes annealed from a total concentration of 1000 nM tiles were incubated in the same sample as the oscillator reaction in the presence of different amounts of insulator gene (which directs co-transcriptional invasion by producing an RNA invader); insulator concentration from top to bottom row is: 150 nM, 100 nM and 50 nM. Left: Violin plots of nanotube length distributions. Right: Corresponding normalized oscillator traces (fraction of active T21).*

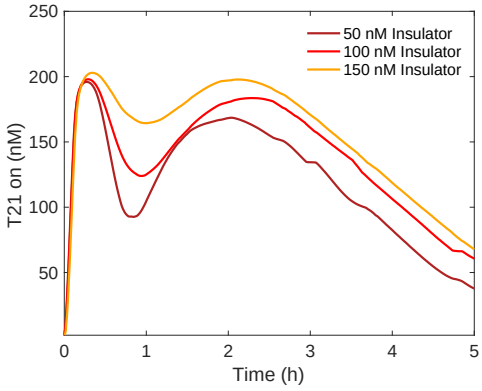

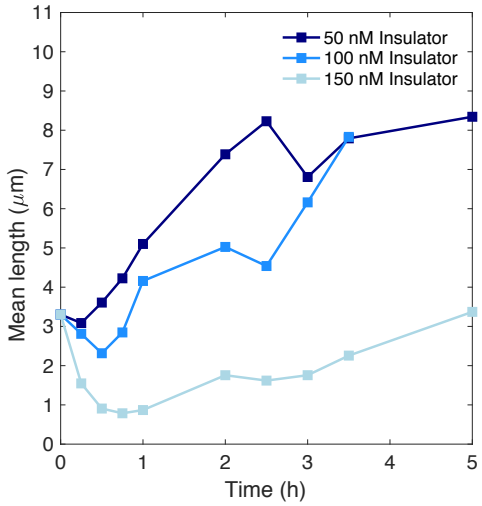

Figure 53: Overview: nanotube growth directed by the oscillator circuit; 1000 nM tile concentration, varying concentration of insulator. *Top: Oscillator, Bottom: Mean length of nanotubes.*

4.13.3 Experiment round 3

This experiment was conducted using experimental conditions defined in Experiment series R3.

Here we report violin plots and individual oscillator traces. The mean and standard deviation of nanotube length and active T21 concentration as a function of time are plotted in Fig. 5 of the main paper.

Control experiment: oscillator and nanotubes in the absence of insulator This experiment was done using the conditions listed for round 3 (R3), at 1000 nM tile concentration, in the absence of insulator.

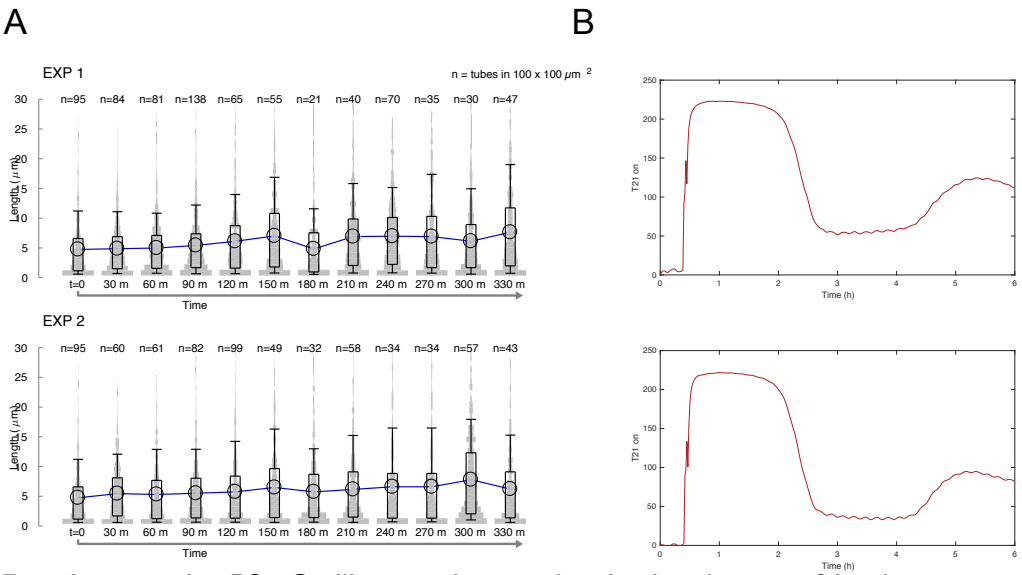

Figure 54: Experiment series R3. Oscillator and nanotubes in the absence of insulator gene. *Nanotubes at 1 μM tile concentration were incubated in the same sample as the oscillator reaction, in the absence of insulator gene (which directs co-transcriptional invasion by producing an RNA invader). In these conditions, the nanotube mean length increases over time exceeding the mean length measured in control experiments (Fig. 42). Left: Violin plots of nanotube length distributions. Nanotubes longer than 15 μM were excluded due to the presence a large number of long overlapping nanotubes, which are automatically excluded by our software. Right: Corresponding normalized oscillator traces (fraction of active T21). Overlapped mean nanotube length and mean oscillator traces are reported in the main paper.*

Oscillator directing nanotubes: 1000 nM tile concentration, insulator 34 nM

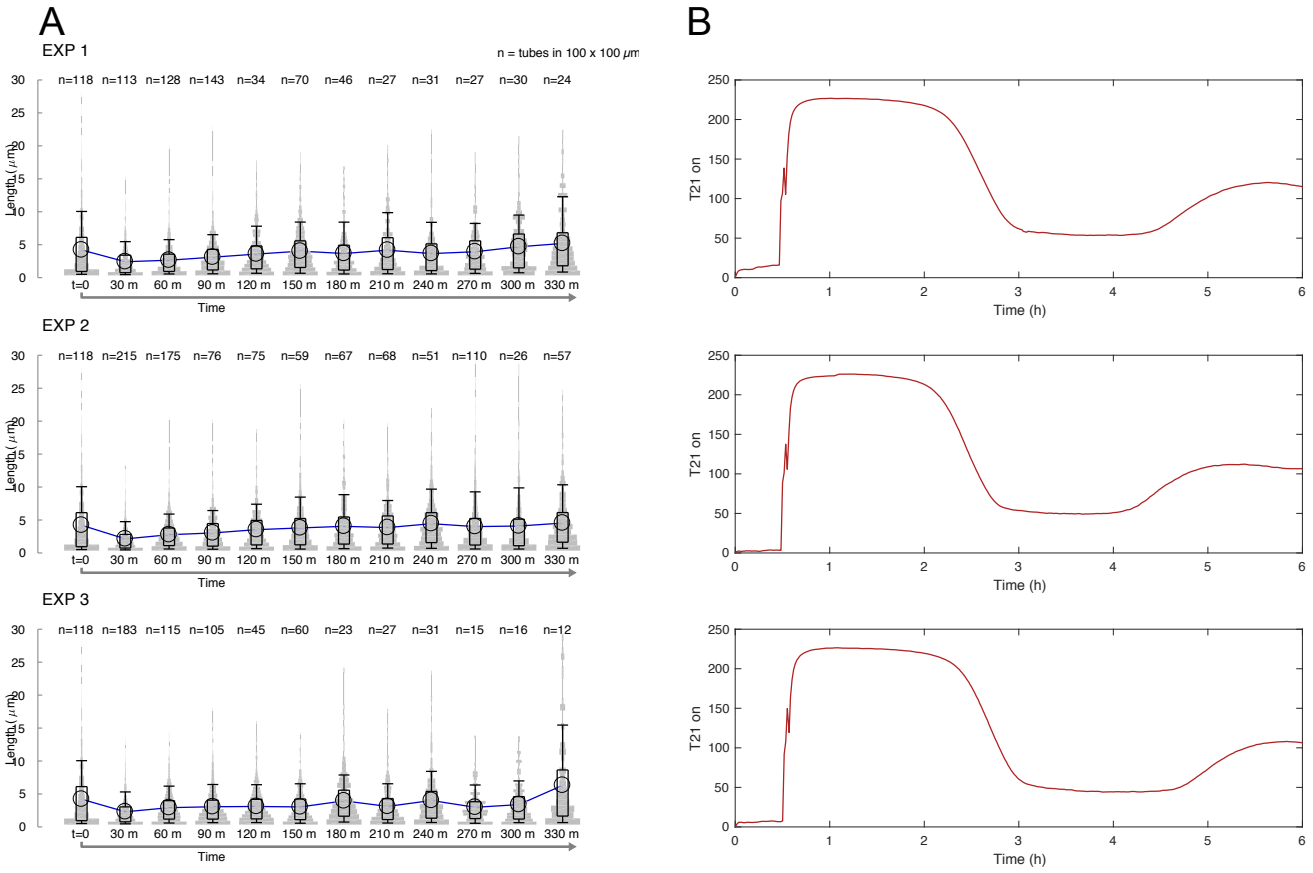

Figure 55: Nanotube growth directed by the oscillator circuit; 1000 nM tile concentration, 34 nM insulator. *Nanotubes annealed from a total concentration of 1000 nM tiles were incubated in the same sample as the oscillator reaction in the presence of different amounts of insulator gene (which directs co-transcriptional invasion by producing an RNA invader). Left: Violin plots of nanotube length distributions. Right: Corresponding normalized oscillator traces (fraction of active T21).*

Oscillator directing nanotubes: 1000 nM tile concentration, insulator 37 nM This experiment was conducted using experimental conditions defined in Experiment series R3.

Here we report violin plots and individual oscillator traces. The mean and standard deviation of nanotube length and active T21 concentration as a function of time are plotted in Fig. 5 of the main paper.

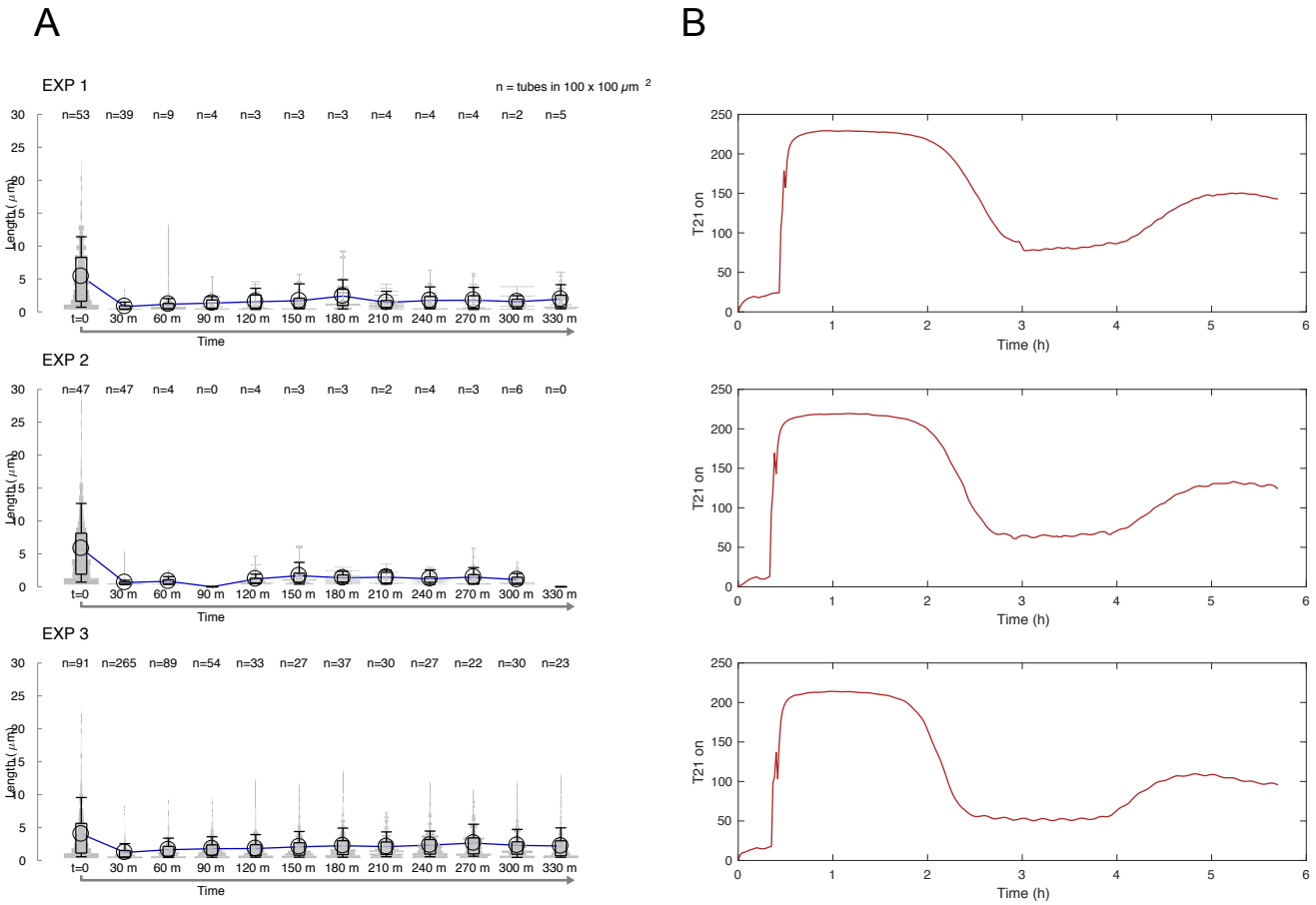

Figure 56: Nanotube growth directed by the oscillator circuit; 1000 nM tile concentration, 37 nM insulator. *Nanotubes annealed from a total concentration of 1000 nM tiles were incubated in the same sample as the oscillator reaction in the presence of 37 nM of insulator gene (which directs co-transcriptional invasion by producing an RNA invader). Left: Violin plots of nanotube length distributions. Right: Corresponding normalized oscillator traces (fraction of active T21).*

Oscillator directing nanotubes: 1000 nM tile concentration, insulator 40 nM This experiment was conducted using experimental conditions defined in Experiment series R3.

Here we report example images taken during the experiment, in addition to those reported in Fig. 5d of the manuscript. Samples were taken every 30 minutes; we only show a subset of sampling times to minimize redundancy (many images are qualitatively equivalent). The oscillator components and the nanotubes are incubated together without enzymes for the first 30 minutes, to make sure temperature is equilibrated. The first sample in each image is taken right after adding enzymes, 30 minutes after starting to collect fluorescence data on the oscillator; the 30 minute mark corresponds to t=0 in the main paper (the 30 minute equilibration data were removed in all oscillator data in Fig. 5). Because overall there is a small number of nanotubes in nearly every field of view, the data were not processed to collect length histograms and compute the mean length over time. Yet, the images show that at oscillator peaks, no nanotubes or rare short nanotubes can be found. At the oscillator well, some long nanotubes can be found in each field of view; similarly, long nanotubes can be found after overnight incubation, when the oscillator reaction is finished and RNA has been largely degraded [11]. Short undegraded RNA molecules bound to the tile sticky end could be responsible for the fact that nanotubes do not regrow to reach length and number similar to the initial sample (t=30 min).

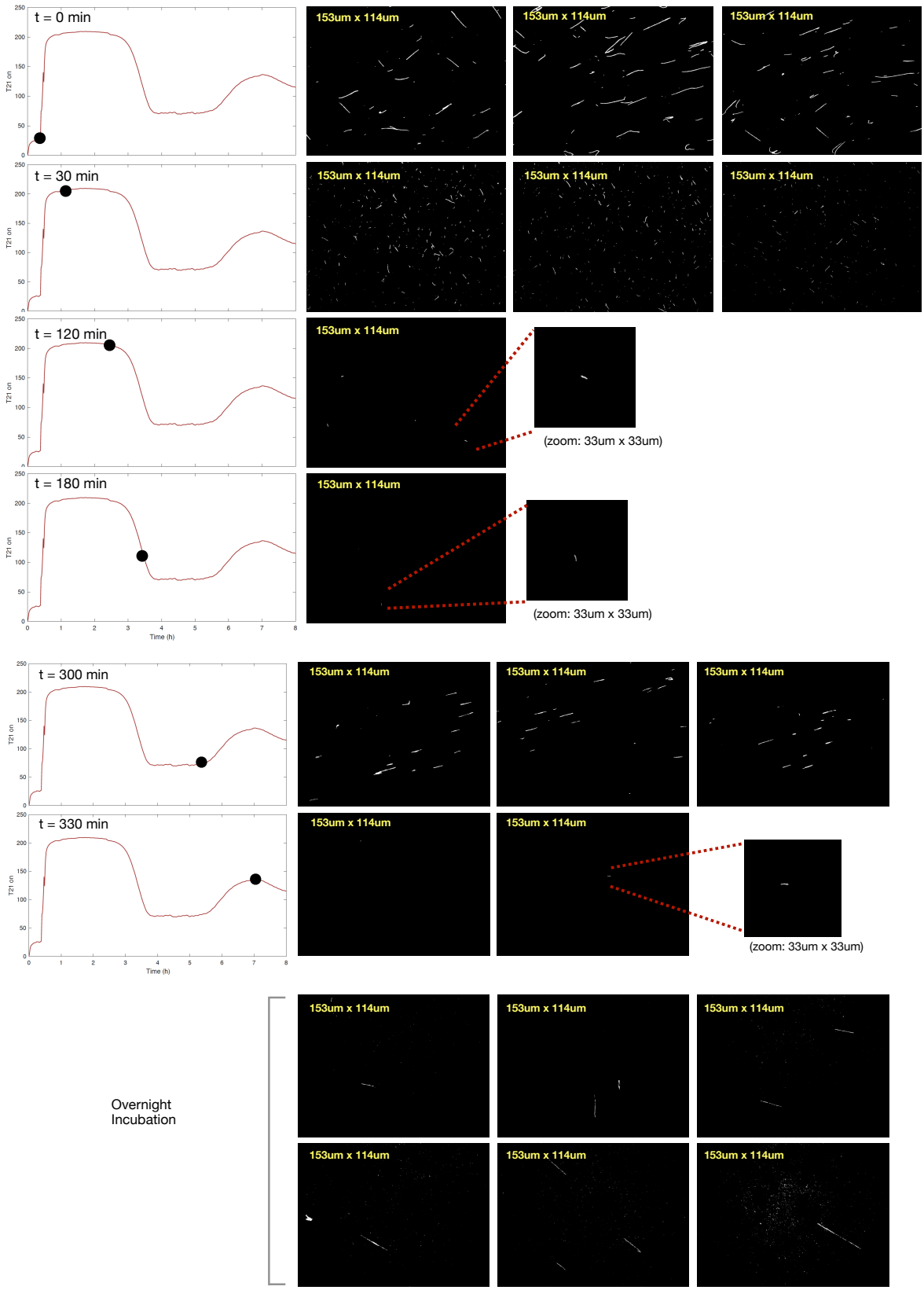

Figure 57: Nanotube growth directed by the oscillator circuit; 1000 nM tile concentration, 40 nM insulator. Repeat 1. *Nanotubes annealed from a total concentration of 1000 nM tiles were incubated in the same sample as the oscillator reaction in the presence of 40 nM of insulator gene (which directs co-transcriptional invasion by producing an RNA invader). Left: Fraction of active T21 template of the oscillator and time of sampling. Right: Representative images.*

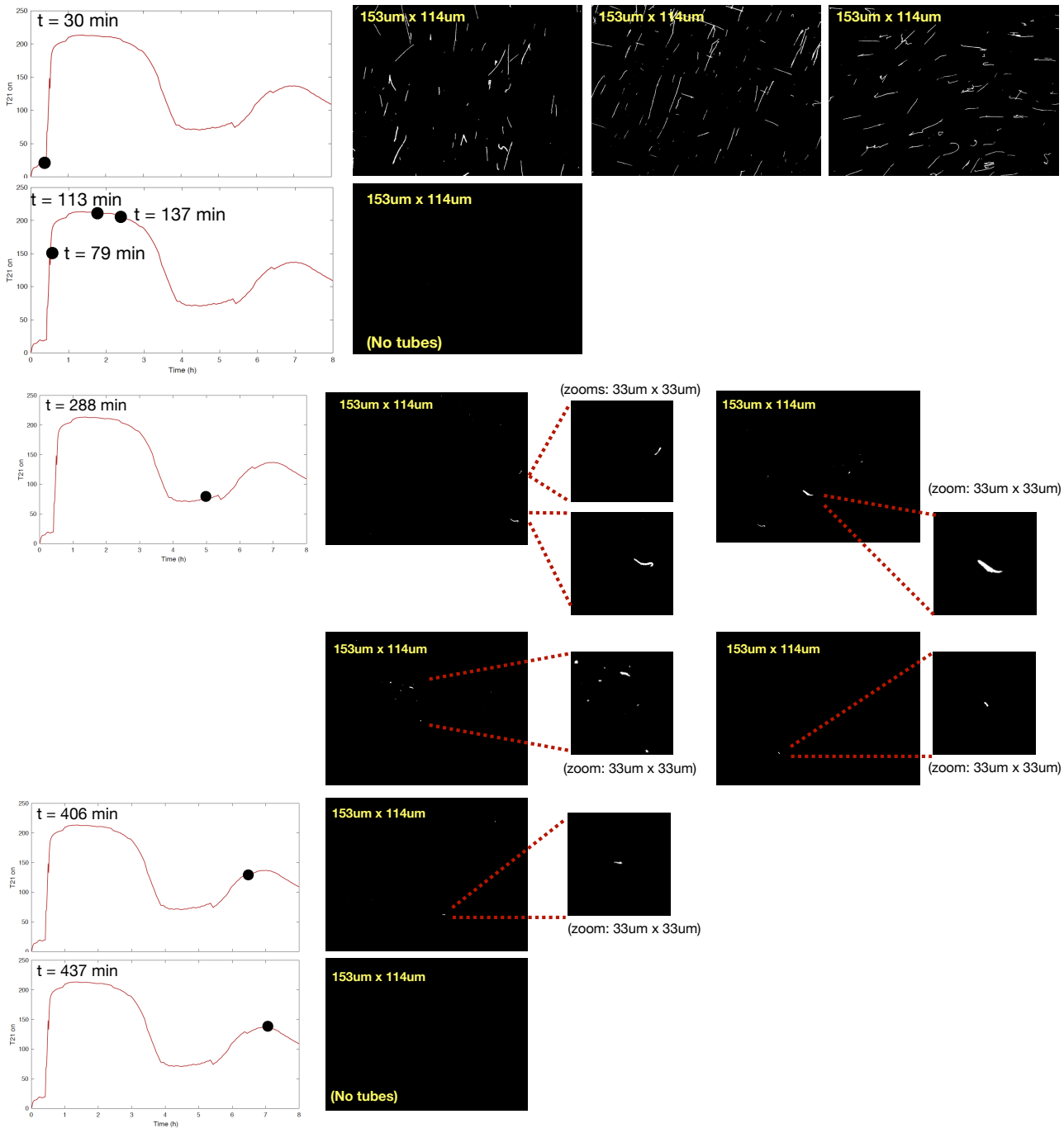

Figure 58: Nanotube growth directed by the oscillator circuit; 1000 nM tile concentration, 40 nM insulator. Repeat 2. *Nanotubes annealed from a total concentration of 1000 nM tiles were incubated in the same sample as the oscillator reaction in the presence of 40 nM of insulator gene (which directs co-transcriptional invasion by producing an RNA invader). Left: Fraction of active T21 template of the oscillator and time of sampling. Right: Representative images.*

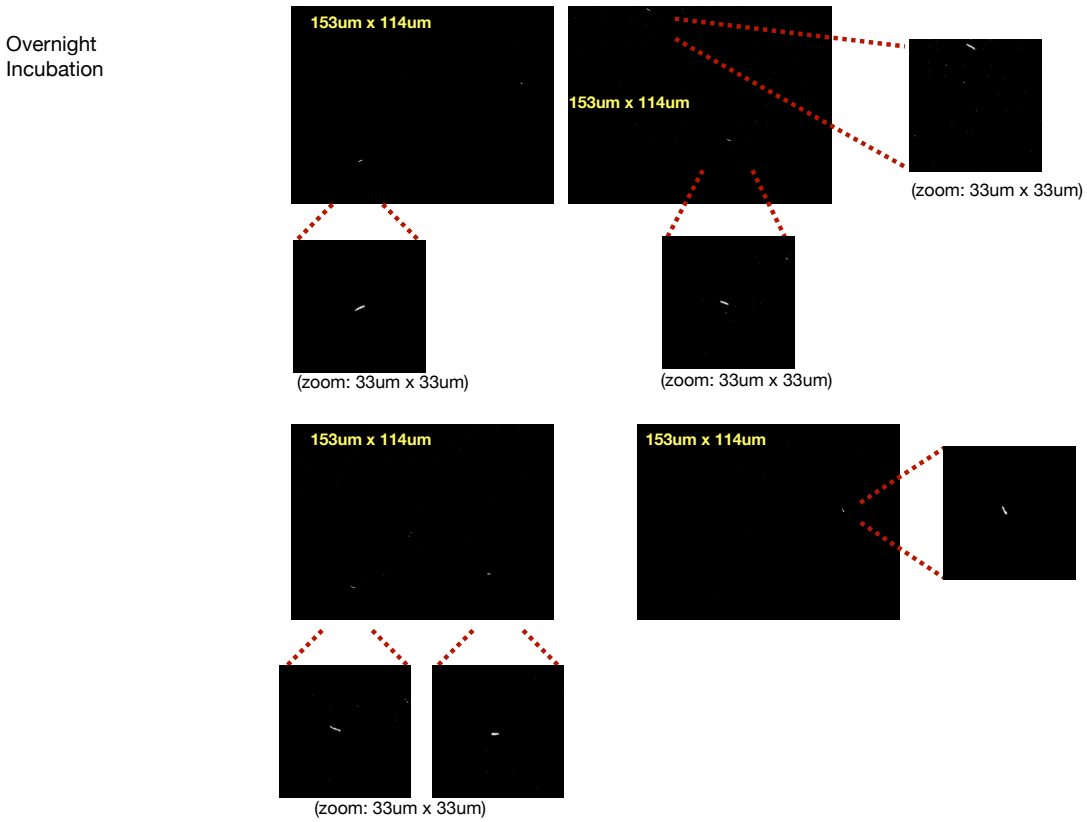

Figure 59: Nanotube growth directed by the oscillator circuit; 1000 nM tile concentration, 40 nM insulator. Repeat 2. Representative images after overnight incubation. *Nanotubes annealed from a total concentration of 1000 nM tiles were incubated in the same sample as the oscillator reaction in the presence of 40 nM of insulator gene (which directs co-transcriptional invasion by producing an RNA invader). These are example images taken after the oscillator has reached steady state and most RNA has been degraded. Short RNA products that cannot be degraded by RNase Hcould bound to sticky ends may prevent regrowth of a large population of nanotubes.*

5 Modeling

5.1 Phenomenological normalization and modeling of experiments on the oscillator directing nanotube self-assembly

The nanotube mean length data collected in Experiment rounds R1 and R2, shown in Figs. 46–51, were normalized with a phenomenological approach.

The nanotube mean length data $L_M(T)$ (where T are the times at which we sampled the nanotube length distribution) were processed by subtracting the baseline growth observed when nanotubes are incubated in oscillator samples. The mean baseline growth in each experiment was estimated using the following phenomenological exponential function:

$$L_{M,sim}(T) = K_0 + K_1(1 - e^{-\frac{T}{\tau}}). \quad (1)$$

This function can be fitted very well to the mean length observed in the control experiments shown in Figs. 46, where nanotubes are grown in the oscillator mix, in the absence of insulator (which couples nanotubes and oscillator). The parameters of expression (1) were fitted using MATLAB's `lsqcurvefit` routine using the bounds in Table 7.

Then, nanotube mean length data were normalized as follows:

$$L_{M,norm}(T) = L_M T - L_{M,sim}(T).$$

Table 6 reports the fitting results for each experimental repeat (separated by commas), and Table 7 summarizes the fitting constraints. For consistency, we normalized with this procedure also the Experiment R1, 750 nM tile concentration, although nanotubes remained disassembled throughout the experiment.

Table 6: *Nanotubes exponential growth model - overview of fitting results for Experiment rounds R1 and R2*

Experiment	K_0 (μM)	K_1 (μM)	τ (min)
R1 Control	2.9, 2.6, 2.5	7.1,9.3,7.0	416,805,389
R1, 750 nM tile	1,1,0.9	0,0,0	1000,1000,1000
R1, 1000 nM tile	2.0,1.4,1.4	3.2,6.2,6.4	401,279,412
R1, 1500 nM tile	2.8, 2.3, 2.4	7.9,8.4,7.6	273, 158, 145
R2, 70 nM insulator	1.8, 1.8, 2.2	7.2, 9.6, 28.4	141, 185, 1000
R2, 100 nM insulator	2.3,2.7,2.4	20.9, 23.1, 24.9	1000,1000,1000

Table 7: *Constraints for the nanotubes exponential growth model*

Bound	K_0 (μM)	K_1 (μM)	τ (min)
Lower	0	0	0
Upper	10	100	1000

5.2 Phenomenological fitting of oscillations

Because samples of nanotube length distribution are sparse, we fitted the normalized nanotube mean length data using a sinusoidal function with exponentially dampened amplitude and frequency; the same function was also fitted to the oscillator data, and fitted frequency and damping coefficients were constrained to be in a comparable range for both nanotube mean length and oscillator data. This approach has the merit of showing that the same phenomenological oscillatory function can fit normalized oscillator and nanotube mean length data, with similar frequency and damping parameters. The caveat of this approach is that data are sparse, and some parts of the experiments are overfitted.

Oscillator The concentration data of SW21-on were first processed by subtracting the mean computed over the duration of the experiment M_{osc}:

$$C_{N,active}(t) = C_{active}(t) - M_{osc}$$

Then, the normalized concentration was fitted using the following function:

$$C_{sim}(t) = Ae^{\alpha t}\cos(\omega t e^{\beta t} + \pi). \tag{2}$$

We used the MATLAB routine `fmincon` to fit the model above to $C_{N,active}(t)$. First, triplicate experiments for a given assay were fitted simultaneously using the constraints listed in Table 8. Then, to account for sample variability, individual experiments were fitted allowing parameters to vary $\pm 10\%$ relative to the ensemble fit; we also allowed the phase to deviate $\pm 10\%$ from π. Results of the fitting procedure are reported in Figs. 60–65.

Table 8: *Constraints for phenomenological oscillator model* (2).

Bound	A (nM)	α (/min)	ω (rad/min)	β (/min)
Lower	100	-0.1	0	-0.1
Upper	300	0	0.2	0

Nanotube mean length The nanotube mean length data $L_M(T)$ (where T are the times at which we sampled the nanotube length distribution) were first processed by subtracting the baseline growth observed when nanotubes are incubated in oscillator samples. The mean baseline growth in each experiment was estimated using the phenomenological exponential function (1), obtaining normalized mean lengths $L_{M,norm}(T)$. Then, the normalized length data were fitted using the same sinusoidal function used for the oscillator data (2):

$$L_{M,sim,osc}(t) = Ae^{\alpha t}\cos(\omega t e^{\beta t}). \tag{3}$$

Function (3) was fitted to the normalized data points $L_{M,norm}(T)$ using MATLAB's `fmincon` routine; for the single-oscillator experiments, we constrained A to be between 0–2 μm, and parameters α, ω, and β to be within $\pm 60\%$ of the corresponding parameter obtained by fitting the oscillator data; for the double-oscillation experiments, we used relaxed constraints shown in Table 9. Results are reported and commented in Figs. 60–65.

Table 9: *Constraints for the phenomenological nanotube mean length model* (3)

Bound	A (μ m)	α (/min)	ω (rad/min)	β (/min)
Lower	0	-0.1	0	-0.1
Upper	2	-10^{-3}	0.2	-10^{-3}

5.2.1 Overview of the fitting results

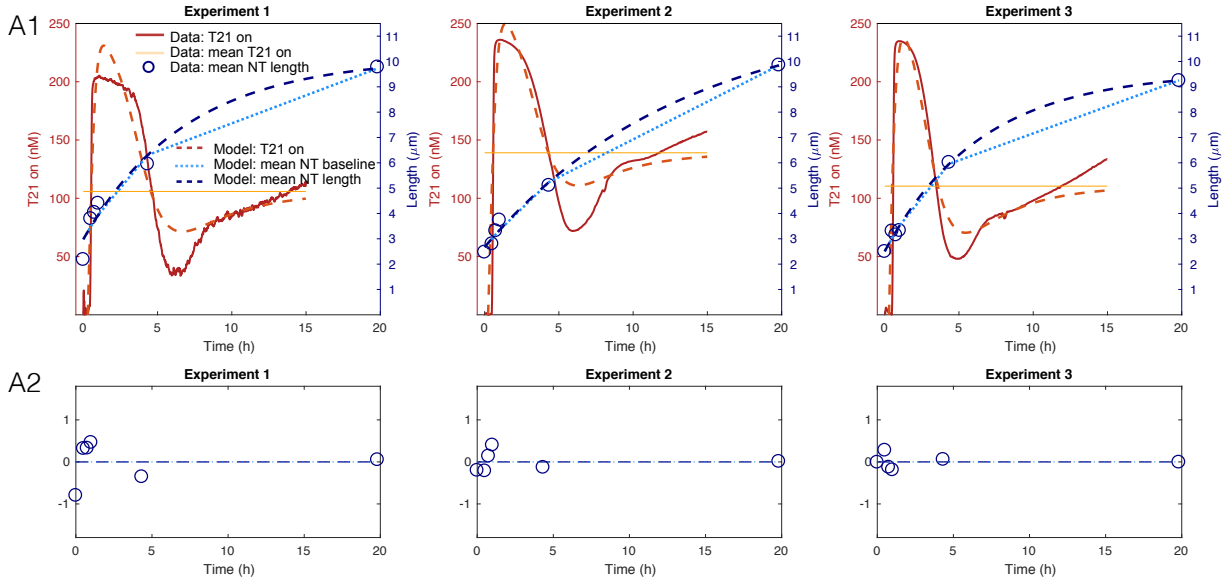

B Nanotube fitting

Mean baseline: $K_0 + K_1(1 - e^{-t/\tau})$

	K0	K1	Tau
Experiment 1	2.98	7.16	416.49
Experiment 2	2.67	9.3	805.64
Experiment 3	2.5	7.1	389.2

Mean length: $Ae^{\alpha t}\cos(\omega t e^{\beta t})$

	A	alpha	omega	beta
Ensemble fit	0	-0.004	0.071	-0.0103
Experiment 1	0	-0.004	0.071	-0.0103
Experiment 2	0	-0.004	0.071	-0.0103
Experiment 3	0	-0.004	0.071	-0.0103

C Oscillator fitting $Ae^{\alpha t}\cos(\omega t e^{\beta t} + \phi)$

	A0	A	alpha	omega	beta	phi
Ensemble fit		201.3	-0.004	0.071	-0.0099	180
Experiment 1	105.86	181.17	-0.004	0.078	-0.0089	162
Experiment 2	139.03	181.18	-0.004	0.076	-0.0091	162
Experiment 3	110.42	221.43	-0.005	0.078	-0.0106	172

Figure 60: Phenomenological fit of experiments shown in Fig. 46: single-oscillation, 1 μM tile concentration, no insulator). *A1: Experimental and simulated data of each experiment. These data are not successfully fitted with a sinusoidal function; this is expected because oscillator and nanotubes are decoupled. A2: Normalized experimental and simulated nanotube mean length data. B and C: Fitting results*

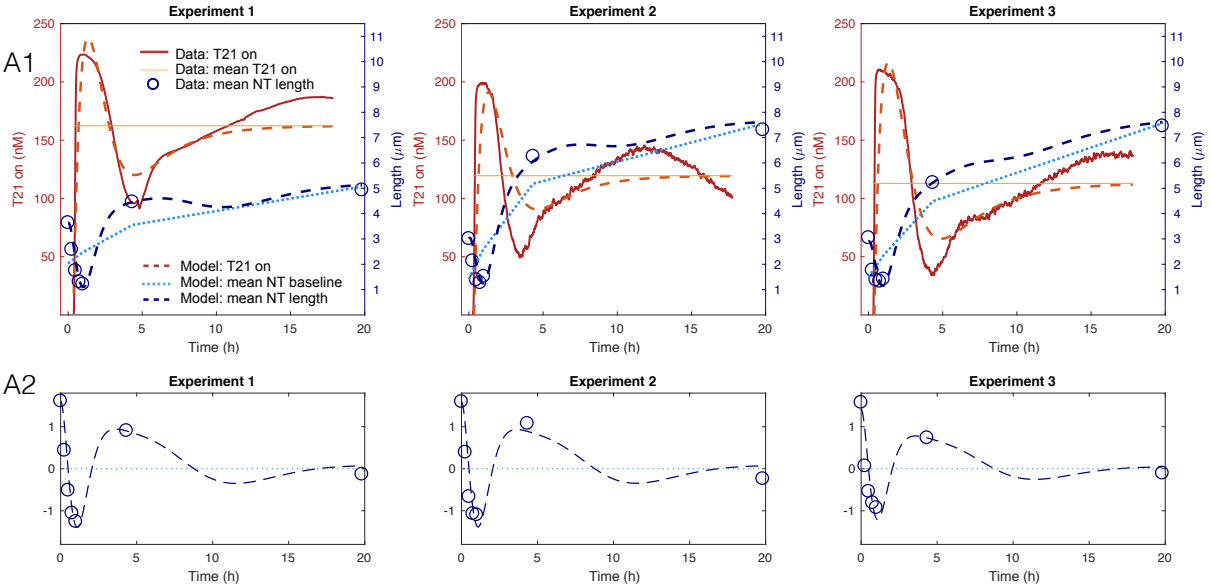

B Nanotube length fitting

Mean baseline: $K_0 + K_1(1 - e^{-t/\tau})$

	K0	K1	Tau
Experiment 1	2.03	3.2	401.35
Experiment 2	1.41	6.22	279.15
Experiment 3	1.5	6.5	412.7

Mean length: $Ae^{\alpha t}\cos(\omega t e^{\beta t})$

	A	alpha	omega	beta
Ensemble fit	1.6	-0.002	0.054	-0.004
Experiment 1	1.61	-0.002	0.06	-0.0036
Experiment 2	1.6	-0.002	0.06	-0.0036
Experiment 3	1.42	-0.002	0.06	-0.0036

C Oscillator fitting $Ae^{\alpha t}\cos(\omega t e^{\beta t} + \phi)$

	A0	A	alpha	omega	beta	phi
Ensemble fit		300	-0.006	0.054	-0.01	180
Experiment 1	162.35	330	-0.006	0.06	-0.011	179
Experiment 2	119.49	270	-0.007	0.06	-0.011	183
Experiment 3	112.91	330	-0.005	0.06	-0.011	186

Figure 61: Phenomenological fit of experiments shown in Fig. 48: single-oscillation, 1 μM tile concentration, 65 nM insulator. *A1: Experimental and simulated data of each experiment. A2: Normalized experimental and simulated nanotube mean length data. B and C: Fitting results*

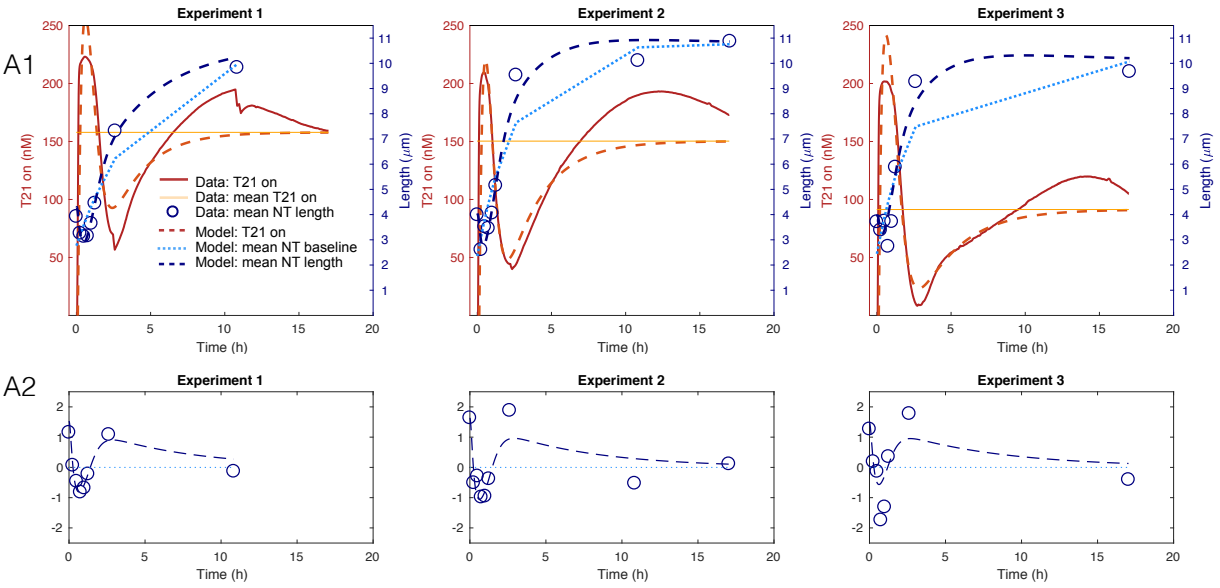

B Nanotube length fitting

Mean baseline: $K_0 + K_1(1 - e^{-t/\tau})$

	K0	K1	Tau
Experiment 1	2.77	7.93	273.5
Experiment 2	2.35	8.42	158.27
Experiment 3	2.4	7.6	145.3

Mean length: $Ae^{\alpha t}\cos(\omega t e^{\beta t})$

	A	alpha	omega	beta
Ensemble fit	1.6	-0.003	0.157	-0.0252
Experiment 1	1.53	-0.003	0.147	-0.0246
Experiment 2	1.64	-0.003	0.16	-0.0249
Experiment 3	1.48	-0.002	0.142	-0.0261

C Oscillator fitting $Ae^{\alpha t}\cos(\omega t e^{\beta t} + \phi)$

	A0	A	alpha	omega	beta	phi
Ensemble fit		245.7	-0.007	0.157	-0.0262	180
Experiment 1	157.87	232.25	-0.007	0.141	-0.0251	186
Experiment 2	150.32	270.24	-0.007	0.149	-0.0288	180
Experiment 3	91.34	232.9	-0.006	0.151	-0.0238	191

Figure 62: Phenomenological fit of experiments shown in Fig. 49: single-oscillation, 1.5 μM tile concentration, 65 nM insulator. *A1: Experimental and simulated data of each experiment. A2: Normalized experimental and simulated nanotube mean length data. B and C: Fitting results*

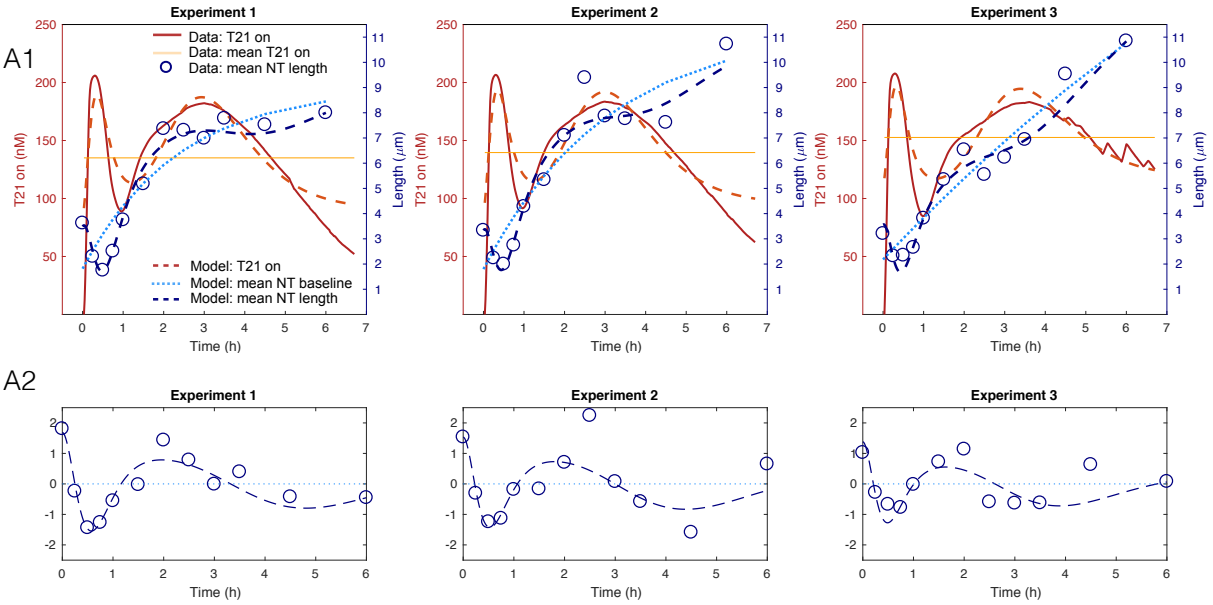

B Nanotube length fitting

Mean baseline: $K_0 + K_1(1 - e^{-t/\tau})$

	K0	K1	Tau
Experiment 1	1.82	7.2	141.43
Experiment 2	1.8	9.67	185.93
Experiment 3	2.2	28.4	1000

Mean length: $Ae^{\alpha t}\cos(\omega t e^{\beta t})$

	A	alpha	omega	beta
Ensemble fit	1.5	-0.003	0.132	-0.009
Experiment 1	1.67	-0.003	0.12	-0.0081
Experiment 2	1.54	-0.002	0.13	-0.0089
Experiment 3	1.38	-0.003	0.142	-0.0099

C Oscillator fitting $Ae^{\alpha t}\cos(\omega t e^{\beta t} + \phi)$

	A0	A	alpha	omega	beta	phi
Ensemble fit		50	0	0.185	-0.0128	180
Experiment 1	135.02	55	0	0.179	-0.0137	198
Experiment 2	139.6	55	0	0.179	-0.0135	198
Experiment 3	152.64	45	0	0.184	-0.0127	198

Figure 63: Phenomenological fit of experiments shown in Fig. 50: double-oscillation, 1 μM tile concentration, 70 nM insulator. *A1: Experimental and simulated data of each experiment. A2: Normalized experimental and simulated nanotube mean length data. B and C: Fitting results*

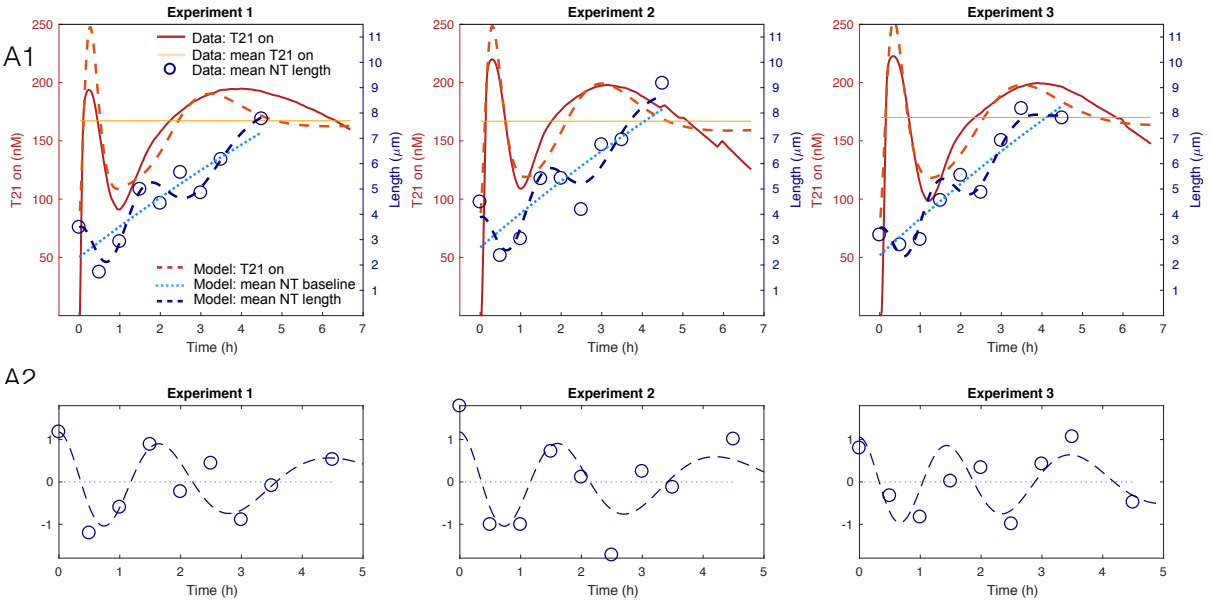

B Nanotube length fitting

Mean baseline: $K_0 + K_1(1 - e^{-t/\tau})$

	K0	K1	Tau
Experiment 1	2.3	20.9	1000
Experiment 2	2.7	23.1	1000
Experiment 3	2.4	24.9	1000

Mean length: $Ae^{\alpha t}\cos(\omega t e^{\beta t})$

	A	alpha	omega	beta
Ensemble fit	1.2	-0.003	0.076	-0.0017
Experiment 1	1.18	-0.003	0.075	-0.0018
Experiment 2	1.18	-0.003	0.076	-0.0017
Experiment 3	1.06	-0.002	0.082	-0.0015

C Oscillator fitting $Ae^{\alpha t}\cos(\omega t e^{\beta t} + \phi)$

	A0 (not fitted)	A	alpha	omega	beta	phi
Ensemble fit		100	-0.006	0.194	-0.0123	180
Experiment 1	167.2	90.05	-0.007	0.213	-0.0134	198
Experiment 2	166.88	90.7	-0.006	0.195	-0.0136	198
Experiment 3	170.07	93.88	-0.006	0.175	-0.0116	193

Figure 64: Phenomenological fit of experiments shown in Fig. 51: double-oscillation, 1 μM tile concentration, 100 nM insulator. *A1: Experimental and simulated data of each experiment. A2: Normalized experimental and simulated nanotube mean length data. B and C: Fitting results*

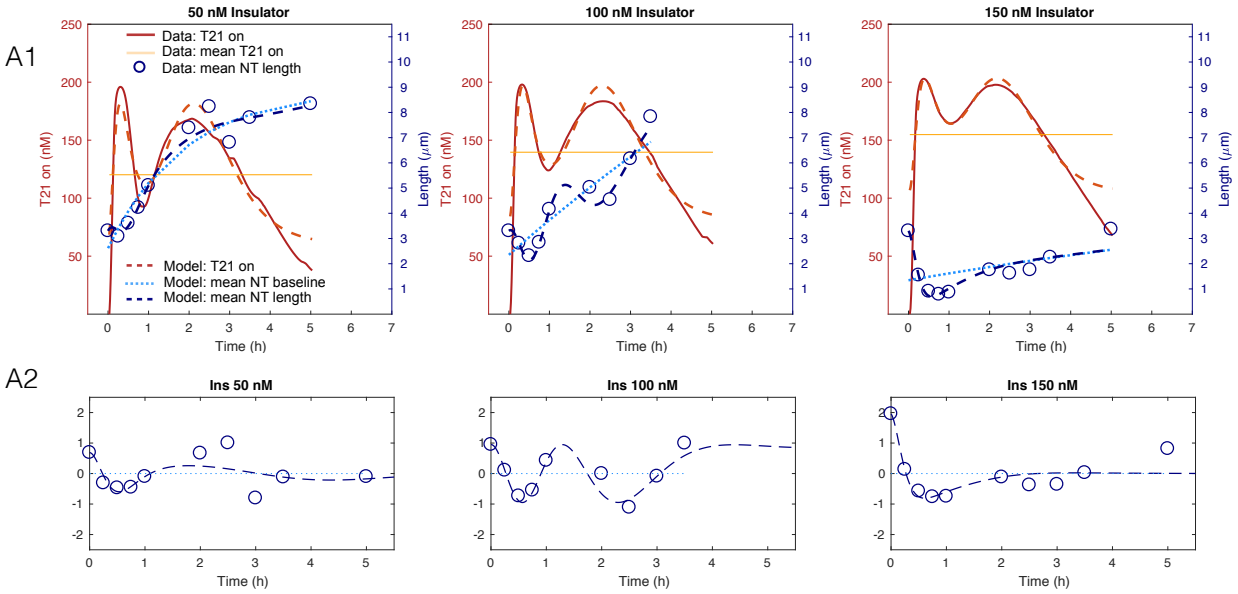

B Nanotube length fitting

Mean baseline: $K_0 + K_1(1 - e^{-t/\tau})$

	K0	K1	Tau
50 nM Insulator	2.62	6.27	112.82
100 nM Insulator	2.35	23.66	1000
150 nM Insulator	1.3	4.7	1000

Mean length: $Ae^{\alpha t}\cos(\omega t e^{\beta t})$

	A	alpha	omega	beta
50 nM Insulator	0.69	-0.004	0.127	-0.0087
100 nM Insulator	0.95	0	0.101	-0.0029
150 nM Insulator	1.96	-0.019	0.125	-0.016

C Oscillator fitting $Ae^{\alpha t}\cos(\omega t e^{\beta t} + \phi)$

	A0	A	alpha	omega	beta	phi
Ensemble fit		52.3	0	0.2	-0.0162	180
50 nM Insulator	154.79	48.68	0	0.204	-0.0158	167
100 nM Insulator	139.63	57.6	0	0.222	-0.0162	171
150 nM Insulator	120.18	61.41	0	0.229	-0.0179	187

Figure 65: Phenomenological fit of experiments shown in Fig. 52: double-oscillation, 1 μM tile concentration, variable concentration of insulator. *A1: Experimental and simulated data of each experiment. A2: Normalized experimental and simulated nanotube mean length data. B and C: Fitting results*

5.3 Fitting the evolution of nanotube length distributions using exponential functions

We fitted the nanotube distributions measured in our experiments where a transcriptional oscillator directs production of invader; specifically, as a test case, we considered Experiment round R2, described at section 4.13.2. The nanotube length distribution at each point in time was fitted using either an exponential distribution (Figs. 66 and 67) or a Flory-Schulz distribution [9] (Figs. 68 and 69). Data fitting was done using MATLAB's `nlinfit` routine. Expressions for the distributions are provided in the figures; in both cases we fitted a single parameter λ. Measured and fitted distributions are overlapped in Figs. 66 and 68; fitted λ values and fitting residuals are plotted in Figs. 67 and 69. Residuals obtained by fitting the distributions using an exponential function are on average smaller than those obtained when using a Flory-Schulz distribution. In both cases, we observe that parameter λ fluctuates as observed in the empirically computed mean of the nanotube length (Fig. 51 and Fig. 5 of the manuscript).

5.3.1 Exponential distribution

$$PDF(L) = \frac{1}{\lambda} e^{-\frac{L}{\lambda}} \qquad CDF(L) = 1 - e^{-\frac{L}{\lambda}}$$

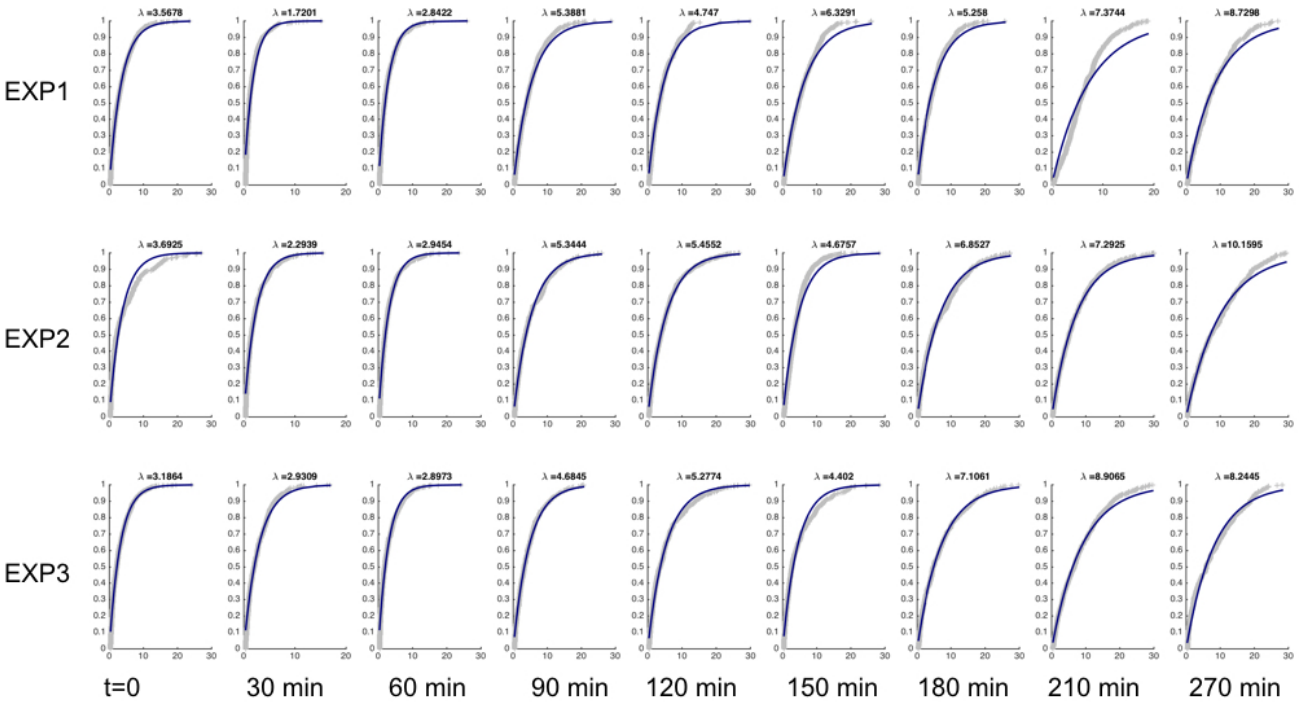

Figure 66: Exponential distribution fit *We fitted length distributions measured in the experiments shown in Fig 51, where we used a transcriptional oscillator to direct nanotube invasion.*

$$PDF(L) = \frac{1}{\lambda} e^{-\frac{L}{\lambda}} \qquad CDF(L) = 1 - e^{-\frac{L}{\lambda}}$$

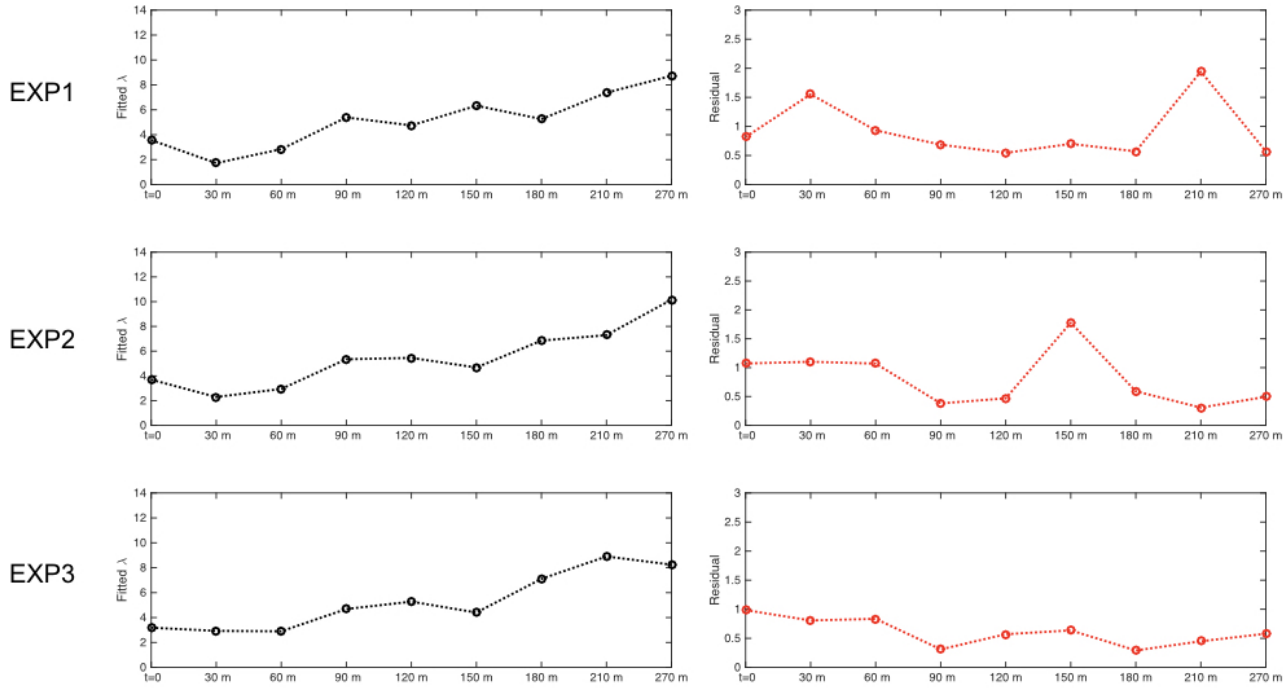

Figure 67: Fitting results from Fig. 66 *A: Fitted λ values for each experiment. B: Residuals of the fitting procedure.*

5.3.2 Flory-Schulz distribution

$$PDF(L) = \frac{L}{\lambda^2} e^{-\frac{L}{\lambda}} \qquad CDF(L) = 1 - e^{-\frac{L}{\lambda}} \left(1 + \frac{L}{\lambda}\right)$$

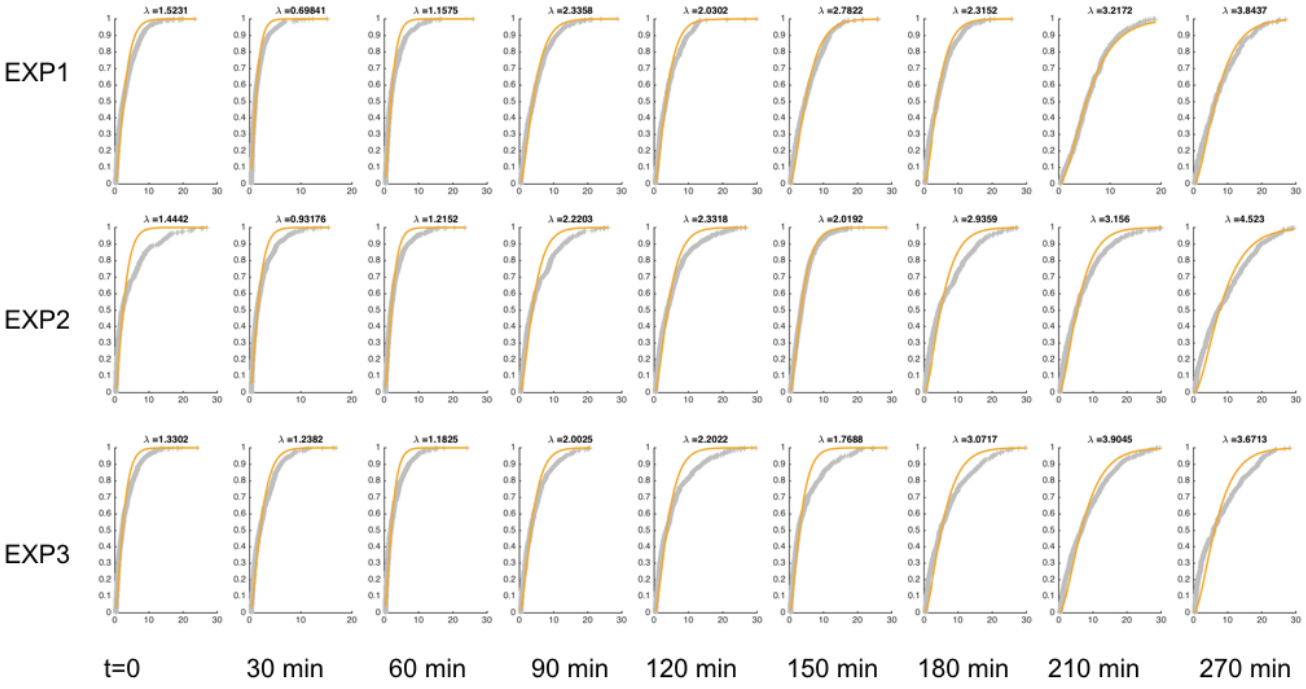

Figure 68: Flory-Schulz distribution fit *We fitted length distributions measured in the experiments shown in Fig 51, where we used a transcriptional oscillator to direct nanotube invasion.*

$$PDF(L) = \frac{L}{\lambda^2} e^{-\frac{L}{\lambda}} \qquad CDF(L) = 1 - e^{-\frac{L}{\lambda}} \left(1 + \frac{L}{\lambda}\right)$$

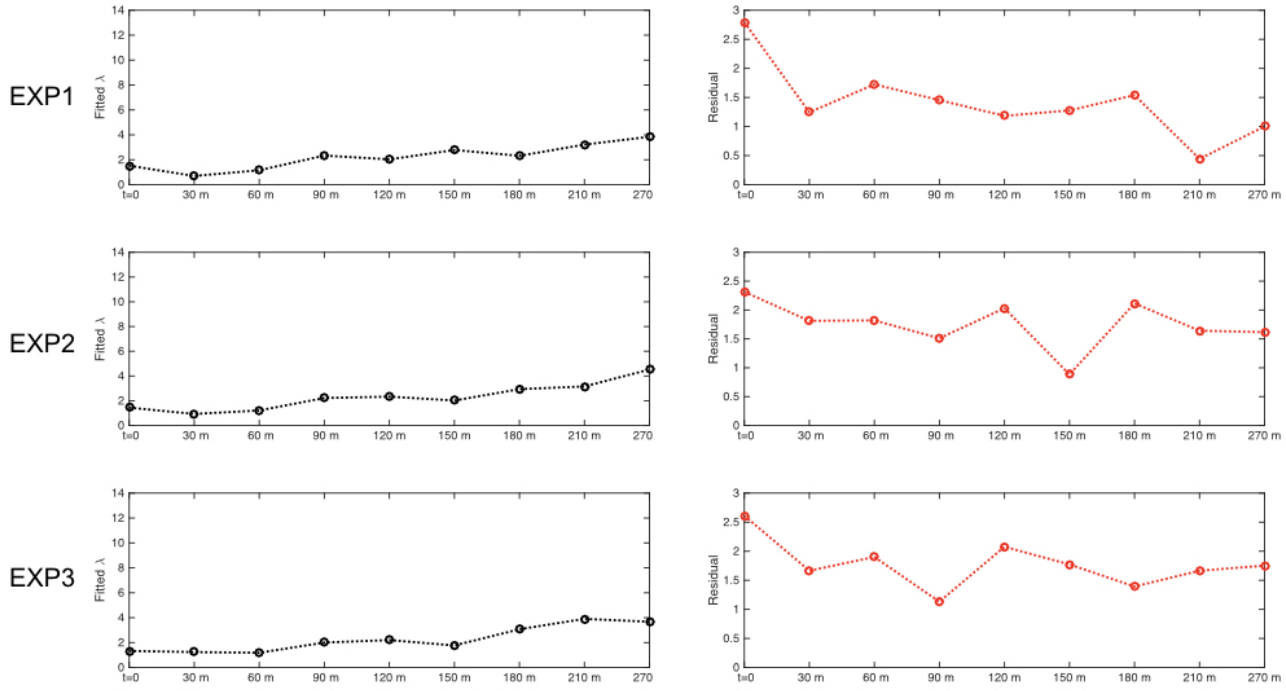

Figure 69: Fitting results from Fig. 68 *A: Fitted λ values for each experiment. B: Residuals of the fitting procedure.*

5.4 Modeling the dynamics of nanotube length distributions

In the following sections we describe the derivation of ordinary differential equation models (ODE) to describe the evolution of nanotube length distributions and the dynamics of the molecular oscillator. In some sections, we indicate molecular species and their concentration with the same (capital) letters to simplify the notation. The model is built based on the results published in [13].

To quantitatively capture how nanotube length distributions vary in response to invasion and anti-invasion reactions in our experiments, we developed a phenomenological model. This model is coarse-grained in the sense that the nanotube population is segmented by length in a number of bins, and we use ordinary differential equations to describe how the population of each bin varies over time. First, one needs to model several processes that are known to affect nanotube length: nucleation, polymerization and depolymerization, end-joining, and fragmentation. These processes were modeled in detail in [13], and here we only report a brief summary; the model was fitted to the data collected in this paper as they are generated by a different type of DNA nanotubes relative to [13]. Further, we focus on the inclusion of additional reactions modeling invasion, anti-invasion, and transcription and degradation processes that generate

5.4.1 Derivation of the model

We consider a solution including assembled nanotubes and unpolymerized tiles. The real distribution of nanotubes is continuous, because our sample includes tubes having any length $L \in [0, l_{max}]$, where l_{max} is the maximum observed length (or a physically meaningful upper bound for length). To build a model that is computationally tractable, we segment the population of molecular species present in the system. We assume the sample includes tiles, whose concentration is indicated as T; nucleated assemblies of tiles, or nuclei, whose concentration is L_0; nanotubes, which are binned by length, so that variable L_n indicates the concentration of nanotubes in bin n. The bin width, which we indicate as l_b, can be chosen depending on the acceptable level of coarseness (and complexity) of the model, because it determines the number of species. For example, if l_b is 300 nm, variable L_1 is the concentration of tubes of length 300 nm. If $l_{max} = 30\,\mu m$, the number of variables in the model is $n_{max} = [l_{max}/l_b] = 100$. Segmentation introduces implicitly the assumption that a tube can switch from bin n to bin $n \pm 1$ only if it acquires or loses a number n_b of tiles, which are the tiles forming a tube segment of length l_b. As an example, let us take again $l_b = 300$ nm; let us assume that the nanotube circumference is on average 7 tiles, each ≈ 14 nm wide; then we find $n_b = 147$ (these figures are based on previous measurements on DAE-E tile nanotubes [19], and were confirmed in our experiments).

We finally assume that tiles, nuclei, and tubes form and interact via several processes, which cause changes in the segmented distribution of nanotube length. An overview of these processes is provided below, together with phenomenological expressions for the rates at which these processes occur. For each description, we identify an equivalent, phenomenological reaction that describes how tiles, nuclei, and nanotubes interact in our model, as well as reactions describing invasion and anti-invasion.

Nucleation Tile assembly is a cooperative process: there is a minimum number of tiles that need to bind simultaneously to form a nucleus, from which polymerization of a nanotube can be initiated. We assume that nucleation depends on the concentration of tiles, and proceeds with rate $k_{nucl}\,T^{n_{nucl}}$, where n_{nucl} is the critical nucleation size. The equivalent phenomenological reaction describing nucleation is:

$$n_{nucl}\,T \xrightarrow{k_{nucl}} L_0. \tag{4}$$

Polymerization and depolymerization Nuclei and nanotubes grow as tiles bind to accessible sites. The polymerization rate depends on the concentration of tiles as well as the availability of

binding sites: for tubes of length n, polymerization occurs at rate $k_p T L_n$. For nuclei, which are smaller patches of tiles, we hypothesize a different polymerization rate $k_{p_0} T L_0$. Tiles can also dissociate from tubes (and nuclei) at a rate that depends exclusively on the concentration of tubes: for tubes of length n, the depolymerization rate is $k_d L_n$; for nuclei, we consider a different depolymerization rate $k_{d_0} L_0$. Equivalent phenomenological reactions describing polymerization and depolymerization are:

$$n_b T + L_n \xrightarrow{k_p} L_{n+1}, \quad n \geq 1 \tag{5}$$

$$(n_b - n_{nucl})\, T + L_0 \xrightarrow{k_{p_0}} L_1 \tag{6}$$

$$L_1 \xrightarrow{k_d} L_0 + (n_b - n_{nucl})\, T \tag{7}$$

$$L_{n+1} \xrightarrow{k_d} L_n + n_b T \ , \text{ for } n \geq 1 \tag{8}$$

$$L_0 \xrightarrow{k_{d_0}} n_{nucl}\, T \tag{9}$$

Here, the stoichiometric coefficients indicate how many tiles need to be added or removed from a nanotube in a certain bin length so that it moves to an adjacent bin. These coefficients are however not related to the order of the reaction rate; for example, in reaction (5) it is not required that n_b tiles bind simultaneously to the tube, therefore this is a second order reaction.

End-joining Nucleated nanotubes diffusing in solution grow not only by polymerization, but also by end-joining, as demonstrated experimentally in [4]. We assume that the joining rate depends on the length of the nanotubes, on their diameter d, and on the concentration of nanotubes in the corresponding length bins. For example, if we consider length bins n and m, we postulate that the joining rate of nanotubes in these bins is $k_{join}(n, m) L_n L_m$. An estimate for $k_{join}(n, m)$ is given in expression (10). This expression assumes that DNA nanotubes are rigid rods, and that their end-joining is a diffusion controlled reaction [7].

$$k_{join}(m, n) = \frac{\alpha}{l_b}\left[\frac{1}{m}\ln\left(\frac{m l_b}{d}\right) + \frac{1}{n}\ln\left(\frac{n l_b}{d}\right)\right] \tag{10}$$

where $\alpha = \kappa \frac{12 k_B T d}{\eta}$, η is the dynamic viscosity of the liquid, k_B is the Boltzmann constant, T is the absolute temperature, d is the nanotube diameter, and κ is a factor accounting for the fraction of productive nanotube collisions. Note that each joining reaction can occur by joining of either end of each nanotube, so every reaction should be accounted for twice.

The concentration of nanotubes in a given bin n increases when shorter tube end-join; an example equivalent reaction is:

$$L_{n-m} + L_m \xrightarrow{k_{join}(n-m,\, m)} L_n \quad \text{for} \quad 1 \leq m \leq \min\{n_{max} - n, n - 1\}.$$

We observe that order of the reactants in the above reaction does not matter. For example, consider the bin of nanotubes having length $5 l_b$. The end-joining reactions that contribute to an increase in the concentration L_5 are:

$$L_1 + L_4 \xrightarrow{k_{join}(1,\,4)} L_5$$

$$L_2 + L_3 \xrightarrow{k_{join}(2,\,3)} L_5$$

Reactions $L_4 + L_1 \xrightarrow{k_{join}(1,\,4)} L_5$ and $L_3 + L_2 \xrightarrow{k_{join}(2,\,3)} L_5$ are redundant and should not be included in the mass balance. The concentration of tubes in bin of length $n l_b$ is therefore incremented by only $\lfloor \frac{n}{2} \rfloor$ end-joining reactions, where "$\lfloor\ \rfloor$" is the largest integer less than or equal to $\frac{n}{2}$.

The concentration of nanotubes in bin n also decreases due to end-joining events, as exemplified in this reaction:

$$L_n + L_m \xrightarrow{k_{join}(m,\,n)} L_{n+m} \quad \text{for} \quad 1 \leq m \leq n_{max} - n$$

Fragmentation Formed nanotubes can spontaneously break into shorter fragments. We assume that breakage rate of nanotubes of length $n\,l_b$ depends on the concentration of nanotubes in bin length n via a constant rate k_{break}. For simplicity, we also assume fragments can only form to fall into the given length bins, and that a nanotube can break into at most two fragments per unit time. For example, a nanotube of length $n\,l_b$ can break into two fragments of length ml_b and $(n-m)l_b$. The equivalent phenomenological reaction for fragmentation is:

$$L_n \xrightarrow{k_{break}} L_m + L_{n-m}.$$

The rate at which the concentration of nanotubes in bin n decreases due to fragmentation is $(n-1)k_{break}L_n$, because there are $n-1$ sites at which breakage may occur. For example, consider the concentration of tubes having length $5l_b$. In this bin, fragmentation occurs according to the following equivalent reactions:

$$L_5 \xrightarrow{k_{break}} L_1 + L_4, \quad L_5 \xrightarrow{k_{break}} L_2 + L_3,$$
$$L_5 \xrightarrow{k_{break}} L_3 + L_2, \quad L_5 \xrightarrow{k_{break}} L_4 + L_1.$$

We note that the concentration of nanotubes in bin n also increases due to breakage of longer nanotubes (bins $m \geq n+1$).

Invasion reactions The process of invasion of nanotubes with external toeholds is rapid and approaches completion within a few minutes, as shown in fluorimetry experiments (Fig. 4.11.3 D1 and D2). Therefore, we assume that invader molecules bind to formed nuclei and nanotubes causing them to immediately disassemble into individual tiles (via a non-cooperative process). In addition, we assume that invader interacts with free tiles (T), making them inactive (T^*). These phenomena are modeled using the following equivalent reactions:

$$T + I \xrightarrow{k_i} T^* \tag{11}$$
$$L_0 + n_{nucl}I \xrightarrow{k_{iL_0}} n_{nucl}T^* \tag{12}$$
$$L_n + n \cdot n_b I \xrightarrow{k_{iL}} n \cdot n_b T^* \tag{13}$$

We neglect the formation of "intermediate" complexes whereby nanotubes bind to invaders without breaking, or breaking into a finite number of fragments.

Anti-invasion reactions We model the anti-invasion process with two reactions, which respectively describe reactivation of inactive tiles (species T^* is converted to T), and titration of free invader:

$$T^* + A \xrightarrow{k_a} T + A \cdot I \tag{14}$$
$$A + I \xrightarrow{k_{ai}} A \cdot I \tag{15}$$

This modeling assumption is appropriate because we assume rapid disassembly of nanotubes into inactive tiles after addition of invader, and we neglect the dynamics of nanotube-invader complexes.

ODE model Using the law of mass action, we can derive a system of ODEs that models all the phenomena described above, and describes the evolution of our segmented nanotube length distribution. Equations (16)-(19) below describe the time derivative of the concentration of tiles (T), nuclei (L_0) and tubes in bin n (L_n):

$$\frac{dT}{dt} = -\underbrace{n_{nucl}k_{nucl}T^{n_{nucl}}}_{\text{nucleation}} - \underbrace{n_b k_p T \sum_{i=1}^{n_{max}-1} L_i \quad -(n_b - n_{nucl})k_{p_0}TL_0}_{\text{polymerization}} \tag{16}$$

$$+ \underbrace{n_b k_d \sum_{i=2}^{n_{max}} L_i + (n_b - n_{nucl})k_d L_1 + n_{nucl}k_{d_0}L_0}_{\text{depolymerization}} - \underbrace{k_i TI}_{\text{invasion}} + \underbrace{k_a T^* A}_{\text{anti-invasion}},$$

$$\frac{dL_0}{dt} = \underbrace{k_{nucl}T^{n_{nucl}}}_{\text{nucleation}} - \underbrace{k_{p_0}TL_0}_{\text{polymerization}} + \underbrace{k_d L_1 - k_{d_0}L_0}_{\text{depolymerization}} - \underbrace{k_{iL_0}L_0 I}_{\text{invasion}}, \tag{17}$$

$$\frac{dL_1}{dt} = \underbrace{k_{p_0}TL_0 - k_p TL_1}_{\text{polymerization}} + \underbrace{k_d L_2 - k_d L_1}_{\text{depolymerization}} - \underbrace{2\sum_{m=1}^{n_{max}-1} k_{join}(1,m)L_1 L_m - 2k_{join}(1,1)L_1^2}_{\text{end-joining}} \tag{18}$$

$$+ \underbrace{2\sum_{m=2}^{n_{max}} k_{break}(L_m \to L_1 + L_{m-1})L_m}_{\text{fragmentation}} - \underbrace{k_{iL}L_1 I}_{\text{invasion}},$$

$$\frac{dL_n}{dt} = \underbrace{k_p T(L_{n-1} - L_{n|_{n<n_{max}}})}_{\text{polymerization}} + \underbrace{k_d(L_{n+1|_{n<n_{max}}} - L_n)}_{\text{depolymerization}} \tag{19}$$

$$\underbrace{-2\sum_{m=1}^{n_{max}-n} k_{join}(n,m)L_n L_m - 2k_{join}(n,n)L^2_{n|_{n\le \frac{n_{max}}{2}}} + 2\sum_{m=1}^{\lfloor \frac{n}{2} \rfloor} k_{join}(n-m,m)L_{n-m}L_m}_{\text{end-joining}}$$

$$\underbrace{+2\sum_{m\ge n+1}^{n_{max}} k_{break}(L_m \to L_n + L_{m-n})L_m - (n-1)k_{break}(L_n \to L_m + L_{n-m})L_n}_{\text{fragmentation}} - \underbrace{k_{iL}L_n I}_{\text{invasion}},$$

$n = 2, ..., n_{max}$.

The differential equations describing the evolution over time of the concentration of inactive tiles, invader and anti-invader are:

$$\frac{dT^*}{dt} = -k_a T^* A + k_i TI + n_{nucl}k_{iL_0}L_0 I + n_b k_{iL} I \sum_{m=1}^{m=n_{max}} mL_m \tag{20}$$

$$\frac{dI}{dt} = -k_{ai}AI - k_i TI - n_{nucl}k_{iL_0}L_0 I - n_b k_{iL} I \sum_{m=1}^{m=n_{max}} mL_m \tag{21}$$

$$\frac{dA}{dt} = -k_a T^* A - k_{ai}AI \tag{22}$$

We clarify the presence of end-joining term $-2k_{join}(n,n)L_n^2$ in equation (19). This term is needed for two reasons: first, end-joining can occur at either end of a nanotube; second, when two nanotubes of length n end-join, two of them are lost from bin n. Thus, overall equation (19) should include a term $-4k_{join}(n,n)L_n^2$: we chose to split it between sum $-2\sum_{m=1}^{n_{max}-n} k_{join}(n,m)L_nL_m$ and the isolated term $-2k_{join}(n,n)L_n^2$.

5.4.2 Modeling cotranscriptional invasion and RNase H-mediated anti-invasion

We model the case where RNA invader is cotranscribed by a synthetic template T_G [10, 11, 6], and anti-invasion is mediated by RNase H degradation. We assume that there are no changes in the processes describing tile nucleation and nanotube polymerization, depolymerization, fragmentation, and end joining (see previous section).

Invader production The synthetic gene T_G is activated by species A_G, which binds to and complete the gene promoter region. The activator A_G is in turn displaced (via toehold-mediated branch migration) from the active gene by inhibitor species I_G. These processes are described by the following reactions:

$$T_G + A_G \xrightarrow{k_{TA}} T_G \cdot A_G \tag{23}$$

$$T_G \cdot A_G + I_G \xrightarrow{k_{TI}} T_G + A_G \cdot I_G \tag{24}$$

$$A_G + I_G \xrightarrow{k_{AI}} A_G \cdot I_G. \tag{25}$$

Transcription of RNA invader (I) is modeled by the following reactions [10], which include off-state transcription rate (inactive T_G exhibits a moderate transcription rate):

$$T_G \cdot A_G + RNAP \underset{k_{+,ON}}{\overset{k_{-,ON}}{\rightleftharpoons}} RNAP \cdot T_G \cdot A_G \xrightarrow{k_{cat,ON}} RNAP + T_G.A_G + I \tag{26}$$

$$T_G + RNAP \underset{k_{+,OFF}}{\overset{k_{-,OFF}}{\rightleftharpoons}} RNAP \cdot T_G \xrightarrow{k_{cat,OFF}} RNAP + T_G + I. \tag{27}$$

The ODEs modeling activation/deactivation of the gene producing invader are therefore:

$$\frac{dT_G}{dt} = -k_{TA}T_GA_G + k_{TI}T_G \cdot A_GI_G = -k_{TA}T_GA_G + k_{TI}(T_G^{tot} - T_G)I_G \tag{28}$$

$$\frac{dA_G}{dt} = -k_{TA}T_GA_G - k_{AI}A_GI_G \tag{29}$$

$$\frac{dI_G}{dt} = -k_{TI}T_G \cdot A_GI_G - k_{AI}A_GI_G = -k_{TI}(T_G^{tot} - T_G)I_G - k_{AI}A_GI_G \tag{30}$$

Finally we define $KM_{ON} = \frac{k_{-,ON}+k_{cat,ON}}{k_{+,ON}}$ and $KM_{OFF} = \frac{k_{-,OFF}+k_{cat,OFF}}{k_{+,OFF}}$ and we find the ODE describing production of RNA invader I.

$$\begin{aligned}\frac{dI}{dt} &= \frac{k_{cat,ON}}{KM_{ON}}RNAP^{tot}\frac{T_G \cdot A_G}{1+\frac{T_G \cdot A_G}{KM_{ON}}} + \frac{k_{cat,OFF}}{KM_{OFF}}RNAP^{tot}\frac{T_G}{1+\frac{T_G}{KM_{OFF}}} \\ &= \frac{k_{cat,ON}}{KM_{ON}}RNAP^{tot}\frac{(T_G^{tot} - T_G)}{1+\frac{(T_G^{tot}-T_G)}{KM_{ON}}} + \frac{k_{cat,OFF}}{KM_{OFF}}RNAP^{tot}\frac{T_G}{1+\frac{T_G}{KM_{OFF}}}\end{aligned} \tag{31}$$

By mass conservation: $\frac{dT_G \cdot A_G}{dt} = -\frac{dT_G}{dt}$ as $T_G + T_G \cdot A_G = T_G^{tot}$.

Invasion reactions As done in the previous section, we assume that RNA invaders deactivate free tiles, and cause disassembly of nuclei and nanotubes into individual inactive tiles.

$$T + I \xrightarrow{k_i} T^* \tag{32}$$

$$L_0 + n_{nucl} I \xrightarrow{k_{iL_0}} n_{nucl} T^* \tag{33}$$

$$L_n + n \cdot n_b I \xrightarrow{k_{iL}} n \cdot n_b T^* \tag{34}$$

Anti-invasion mediated by RNase H RNA invaders bound to tiles are degraded by RNase H, which therefore acts as an enzymatic anti-invader molecule responsible for reactivating inactive tiles via the following reaction:

$$T^* + RNaseH \underset{k_{+,a}}{\overset{k_{-,a}}{\rightleftharpoons}} T^* \cdot RNaseH \xrightarrow{k_{cat,a}} T + RNaseH \tag{35}$$

We define $KM_a = \frac{k_{-,a}+k_{cat,a}}{k_{+,a}}$, and we write the resulting dynamics of tile invasion and anti-invasion:

$$\frac{dT}{dt} = \frac{k_{cat,a}}{KM_a} RNaseH^{tot} \frac{T^*}{1 + \frac{T^*}{KM_a}} \tag{36}$$

$$\frac{dT^*}{dt} = -\frac{k_{cat,a}}{KM_a} RNaseH^{tot} \frac{T^*}{1 + \frac{T^*}{KM_a}} \tag{37}$$

Overall model The ODEs describing the evolution of the nanotube length distribution under the control of RNA invaders and RNase H anti-invasion are:

$$\frac{dT}{dt} = -\underbrace{n_{nucl}k_{nucl}T^{n_{nucl}}}_{\text{nucleation}} - \underbrace{n_b k_p T \sum_{i=1}^{n_{max}-1} L_i - (n_b - n_{nucl})k_{p_0} T L_0}_{\text{polymerization}} \tag{38}$$

$$+ \underbrace{n_b k_d \sum_{i=2}^{n_{max}} L_i + (n_b - n_{nucl})k_d L_1 + n_{nucl}k_{d_0}L_0}_{\text{depolymerization}} - \underbrace{k_i T I}_{\text{invasion}} + \underbrace{\frac{k_{cat,a}}{KM_a}[RNaseH]^{tot}\frac{T^*}{1+\frac{T^*}{KM_a}}}_{\text{anti-invasion}},$$

$$\frac{dL_0}{dt} = +\underbrace{k_{nucl}T^{n_{nucl}}}_{\text{nucleation}} - \underbrace{k_{p_0}TL_0}_{\text{polymerization}} + \underbrace{k_d L_1 - k_{d_0}L_0}_{\text{depolymerization}} - \underbrace{k_{iL_0}L_0 I}_{\text{invasion}}, \tag{39}$$

$$\frac{dL_1}{dt} = +\underbrace{k_{p_0}TL_0 - k_p T L_1}_{\text{polymerization}} + \underbrace{k_d L_2 - k_d L_1}_{\text{depolymerization}} - \underbrace{2\sum_{m=1}^{n_{max}-1} k_{join}(1,m)L_1 L_m - 2k_{join}(1,1)L_1^2}_{\text{end-joining}} \tag{40}$$

$$+ \underbrace{2\sum_{m=2}^{n_{max}} k_{break}(L_m \to L_1 + L_{m-1})L_m}_{\text{fragmentation}} - \underbrace{k_{iL}L_1 I}_{\text{invasion}},$$

$$\frac{dL_n}{dt} = +\underbrace{k_p T(L_{n-1} - L_{n|_{n<n_{max}}})}_{\text{polymerization}} + \underbrace{k_d(L_{n+1|_{n<n_{max}}} - L_n)}_{\text{depolymerization}} \tag{41}$$

$$- \underbrace{2\sum_{m=1}^{n_{max}-n} k_{join}(n,m)L_n L_m - 2k_{join}(n,n)L^2_{n|_{n\le\frac{n_{max}}{2}}} + 2\sum_{m=1}^{\lfloor\frac{n}{2}\rfloor} k_{join}(n-m,m)L_{n-m}L_m}_{\text{end-joining}}$$

$$+ \underbrace{2\sum_{m\ge n+1}^{n_{max}} k_{break}(L_m \to L_n + L_{m-n})L_m - (n-1)k_{break}(L_n \to L_m + L_{n-m})L_n}_{\text{fragmentation}} - \underbrace{k_{iL}L_n I}_{\text{invasion}},$$

$n = 2, ..., n_{max}$.

The ODEs describing the behavior of inactive tiles, of the invader and of the synthetic gene, its activator, and inhibitor are:

$$\frac{dT^*}{dt} = k_i T I + n_{nucl}k_{iL_0}L_0 I + n_b k_{iL} I \sum_{m=1}^{m=n_{max}} mL_m - \frac{k_{cat,a}}{KM_a}RNaseH^{tot}\frac{T^*}{1+\frac{T^*}{KM_a}} \tag{42}$$

$$\frac{dI}{dt} = \frac{k_{cat,ON}}{KM_{ON}}RNAP^{tot}\frac{(T_G^{tot} - T_G)}{1+\frac{(T_G^{tot}-T_G)}{KM_{ON}}} + \frac{k_{cat,OFF}}{KM_{OFF}}RNAP^{tot}\frac{T_G}{1+\frac{T_G}{KM_{OFF}}} \tag{43}$$

$$-k_i T I - n_{nucl}k_{iL_0}L_0 I - n_b k_{iL} I \sum_{m=1}^{m=n_{max}} mL_m$$

$$\frac{dT_G}{dt} = -k_{TA}T_G A_G + k_{TI}(T_G^{tot} - T_G)I_G \tag{44}$$

$$\frac{dA_G}{dt} = -k_{TA}T_G A_G - k_{AI}A_G I_G \tag{45}$$

$$\frac{dI_G}{dt} = -k_{TI}(T_G^{tot} - T_G)I_G - k_{AI}A_G I_G \tag{46}$$

5.4.3 Data fitting approach

The parameters for Model (16)-(19) were estimated by fitting the model to length distributions measured over time in invasion and anti-invasion experiments. First, we established parameters of our model that depend on the type of nanotubes we consider, and on the desired level of coarse graining. We choose the length bin: $l_b = 300$ nm; the maximum nanotube length is set as $l_{max} = 33\ \mu m$. These choices imply that we have a number of bins $n_{max} = 110$; thus the nanotube length distribution model includes 112 differential equations (including the ODEs for tiles and nuclei). The number of tiles in a tube chunk of length l_b is $n_b = 147$. (This follows from our assumption that the tubes have a 7-tile circumference, with ≈ 14 nm tile width). ODEs were integrated with in-house MATLAB scripts. We chose an integration step of 1 second. ODEs modeling the kinetics of invader and anti-invader, or of cotranscriptionally procuded invader and RNase H-mediated anti-invasion are integrated simultaneously with the nanotube length distribution ODEs.

Predicted nanotube distributions at time t are generated deterministically by integrating ODEs (16)-(19) (up to time t). Rather than comparing length histograms generated by the model to experimental histograms, we compare their cumulative distributions. This choice is motivated by the following observations: 1) Cumulative distributions are by definition scaled by the sample size (in our case, nanotube sample number). This implies that cumulative distributions of different samples can be immediately compared without requiring *ad hoc* normalization (which would be necessary to compare histograms). 2) Cumulative distributions do not require binning of data like a histogram, thus the fitting procedure is not biased by the choice of bin width.

To compare experimental and simulated cumulative distributions at the same points (nanotube length), we interpolated experimental cumulative length distributions. After interpolation, the model and experimental distributions at any given time are described by comparable vectors:

$$V_{sim}(t) = \frac{1}{\mathcal{L}_{sim}} \cdot \begin{bmatrix} L_{1,sim}(t) \\ L_{1,sim}(t) + L_{2,sim}(t) \\ \vdots \\ \sum_1^{n_{max}} L_{i,sim}(t) \end{bmatrix}, \quad V_{exp}(t) = \frac{1}{\mathcal{L}_{exp}} \cdot \begin{bmatrix} L_{1,exp}(t) \\ L_{1,exp}(t) + L_{2,exp}(t) \\ \vdots \\ \sum_1^{n_{max}} L_{i,exp}(t) \end{bmatrix},$$

where $\mathcal{L}_{sim} = \sum_{i=1}^{n_{max}} L_{i,sim}(t)$, and $\mathcal{L}_{exp} = \sum_{i=1}^{n_{max}} L_{i,exp}(t)$. These distributions are to be compared at the appropriate measurement times.

Fitting is done to identify several parameters in our model. Specifically, we fit the nucleation rate (k_{nucl}) and critical nucleation size (n_{nucl}), the polymerization and depolymerization rates for tubes and nuclei (k_p, k_{p_0}, k_d, and k_{d_0}), the breakage rate (k_{break}), and parameter α in the joining rate expression (10). These parameters can be stacked in a vector p, and we set up our fitting problem as the minimization of the objective function, which simultaneously compares the simulated distribution to the distributions of three separate experiments:

$$\min_p J = \sum_{j=1}^{3} \sum_t (V_{sim}(t) - V_{exp}^j(t))^\top (V_{sim}(t) - V_{exp}^j(t)). \tag{47}$$

Minimization was done using the `fmincon` routine in MATLAB. Initial conditions for the parameters were sampled uniformly in physically plausible intervals delimited by lower and upper bounds listed in Table 11; parameters were also constrained to fall within these bounds. We also imposed a lower bound of 10 nM on the admissible free tile concentration. Initial conditions for the model variables were chosen as $T(0) = 1\ \mu$M, $L_i(0) = 0\ \mu$M for $i = 0, ..., n_{max}$, *i.e.* we assumed that initially only free tiles

are present; this assumption is consistent with the experimental conditions that were fitted, because nanotube annealing was quenched quickly from 47°C to room temperature so the concentration of nuclei and tubes is negligible. This approximation is sensible, however it will be refined in the future by measuring the initial concentration of tiles, nuclei and short tubes using native gel electrophoresis or fluorescence spectroscopy.

Several fitting campaigns were launched and evaluated. Minimizing the objective function (47) is a non-convex problem, thus the fitting routine is likely to converge to local minima that depend on the randomly chosen initial conditions for the parameter vector. We report the best fitting results in Tables 11 and 12.

Table 10: Modeling constants

Parameter	Units	Value	Definition
ϵ	(s)	1	Integration time
n_b	NA	147	Number of tiles in the smallest nanotube
n_{max}	NA	110	Maximum number of bins
l_b	(μm)	0.3	Length of the smallest tube
d	(μm)	13×10^{-3}	Nanotube diameter

5.4.4 Fitted model parameters: Invasion and anti-invasion by DNA molecules

We fitted the experiments in Section 4.7.5. The fitted rate constants are listed in Table 11. Fitted rates are generally different than those obtained in earlier work [13], which focused on a different type of nanotubes. We attribute the discrepancies to the following reasons: a) nanotubes used for these experiments include a toehold domain (in contrast to the tiles considered in [13]), which affects stacking interactions among neighboring tiles and thus polymerization/depolymerization rates; b) here invader and anti-invader reactions are modeled and fitted simultaneously with the nanotube model; c) nanotube growth experiments in [13] were conducted on a two-tile system, in which nucleation can be controlled more precisely.

We compare the rates fitted here to prior results in the literature. The fitted polymerization rate (tiles binding to growing nanotubes) is roughly two orders of magnitude slower than rates estimated for individual tiles binding to a growing tube [5, 8]; however, if we factor into our fitted rate the number of tiles in a bin n_b, we obtain a rate that is comparable to the literature [5, 8, 29]. The fitted tube depolymerization rate is about one order of magnitude faster than the estimates in [5], and in [8] for DAO-O nanotubes measured at 33°C. The nucleation rate $n_{nucl}\, k_{nucl} \approx 2.8 \times 10^2$ $\mathrm{M}^{1-n_{nucl}}/\mathrm{s}$ is significantly slower than the previous estimate of 2×10^5 $\mathrm{M}^{1-n_{nucl}}/\mathrm{s}$ obtained in [29] (presumably because, unlike [29], we did not use annealed and gel-purified tiles; additionally, the model in [29] discriminates between unbound tiles, tiles bound to nanotubes, and nucleated nanotubes, but does not model nanotubes in a given length bin); our critical nucleation size is $\approx 50\%$ larger than the one estimated in [29]. Polymerization rates on growing nuclei are comparable to the corresponding rates of growing tubes. Our joining rate expression (10) depends on the fitted parameter α, and on the length of joining tubes: k_{join} peaks when $n = m = 1$, reaching $6.89 \times 10^8/\mathrm{M/s}$, and is a decreasing function of nanotube length. We evaluated the expression for k_{join} over its domain n, m, as shown in Fig. 70, and computed an average $k_{join} = 4.1348\,10^7/\mathrm{M/s}$. This reaction rate is three orders of magnitude higher than the joining rate estimate for DNA ribbons in [21], which is $3.5 \times 10^4/\mathrm{M/s}$, and is higher

than hybridization rates for DNA and RNA; this indicates that we may be overestimating the actual joining rate due to our choice of fitting constraints. Further, because we are simultaneously fitting numerous parameters with non stringent constraints, it is reasonable to expect fits falling in a broad range of values, as we showed in recent work on this model (but different nanotube type) by comparing the results of 350 fitting campaigns [13]. Finally, our fragmentation rate is in the order of 10^{-4}/s, suggesting that breakage events are rare. The fitted invasion rates (for individual tiles, nuclei, and nanotubes) and anti-invasion rates are in the order of 10^5/M/s, which is comparable to hybridization and strand displacement rates for oligos of similar length that can be found in the literature [10, 29].

We plot the cumulative distribution fits, concentration of important components (total, free, and inactive tile concentration, concentration of nuclei, invader and anti-invader), histogram fits, and mean length in Fig. 71. For an additional sanity check we also estimate nanotube density in a 100 μm $\times$ 100 μm area in Fig. 72; to estimate this number we assumed a 20X dilution factor (consistently with our experimental protocol), and that half the nanotubes in the imaging sample land on the imaged glass surface. We computed the sample volume of each experimental sample using the average measured thickness of an imaging sample (2.35 μm). The number of nanotubes generally falls in the same range as our experimental observations, however the estimate notably does not capture the initial burst in nanotube number measured post anti-invasion (Fig. 72).

Finally, we note that fitted rates depend on the chosen level of granularity of the model (number of bins) [13].

Table 11: Parameters fitted for model equations (16)–(22) *Parameters were fitted to data shown in Fig. 29*

Parameter	Units	L.B.	U.B.	Fitted value	Definition
k_p	$(/M/s)$	10^1	10^7	4.1045×10^4	Tube polymerization rate
k_d	$(/s)$	10^{-8}	10^4	2.161×10^{-1}	Tube depolymerization rate
α	$(\mu m/M/s)$	10^4	10^{10}	3.294×10^7	End-joining parameter
k_{break}	$(/s)$	10^{-6}	10^2	3.861×10^{-4}	Fragmentation rate
k_{nucl}	$(/M^{n_{nucl}-1}/s)$	10^{-2}	10^8	7.682×10^2	Nucleation rate
k_{p_0}	$(/M/s)$	10^1	10^7	3.704×10^4	Nuclei polymerization rate
k_{d_0}	$(/s)$	10^{-8}	10^1	1.988×10^{-2}	Nuclei depolymerization rate
n_{nucl}	NA	3	5	3.637	Critical nucleation size
k_i	$(/M/s)$	10^2	10^6	2.419×10^5	Invasion rate of tiles
k_{iL0}	$(/M/s)$	10^2	10^6	1.854×10^5	Invasion rate of nuclei
k_{iL}	$(/M/s)$	10^2	10^6	1.393×10^5	Invasion rate of nanotubes
k_{ai}	$(/M/s)$	10^2	10^6	5.333×10^3	Binding rate of invaders and anti-invaders
k_a	$(/M/s)$	10^2	10^6	2.314×10^3	Activation rate of inactive tiles

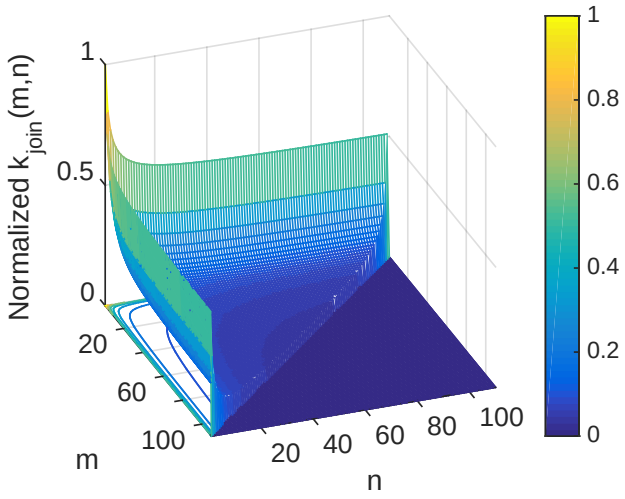

Figure 70: Normalized plot of the fitted nanotube joining rate k_{join}. *The rate was normalized with respect to its maximum value* $k_{join}^{max} = 20.92\,\alpha$.

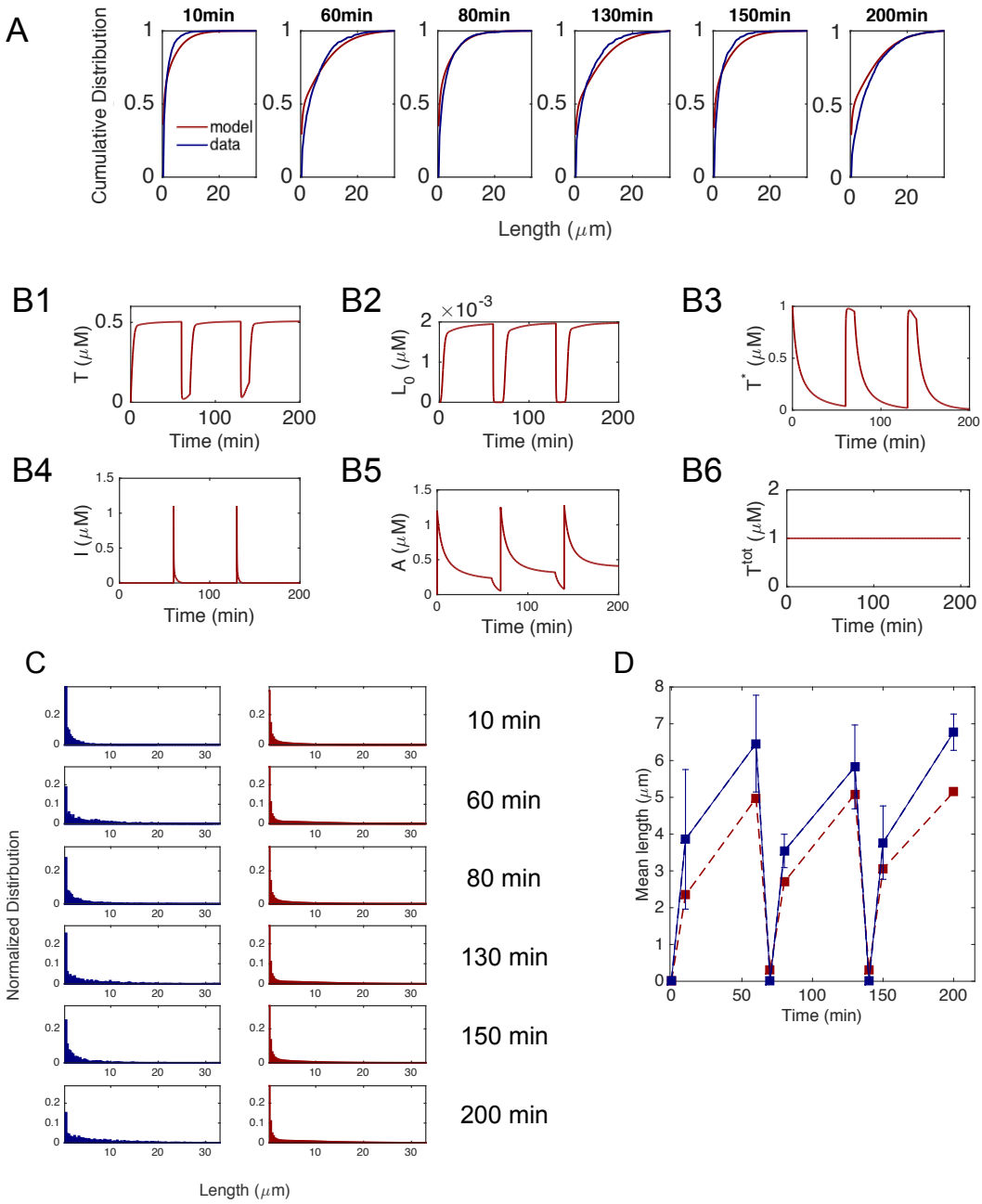

Figure 71: Numerical simulation reproducing the sequential invasion and anti-invasion experiments. *A: Comparison between a representative experimental (blue) cumulative length distributions gathered during nanotube growth and the cumulative distribution generated by our model (red). B1: Time course of free tile concentration. B2: Nuclei concentration. B3: Concentration of inactive tiles. B4: Concentration of free invader. B5: Concentration of free anti-invader. B6: The total tile concentration remains constant. C: Histograms of representative growth experiment (blue) and histograms generated by our model (red). D: Mean and standard deviation of the mean in our nanotube growth experiments, compared with the mean length predicted by our fitted model.*

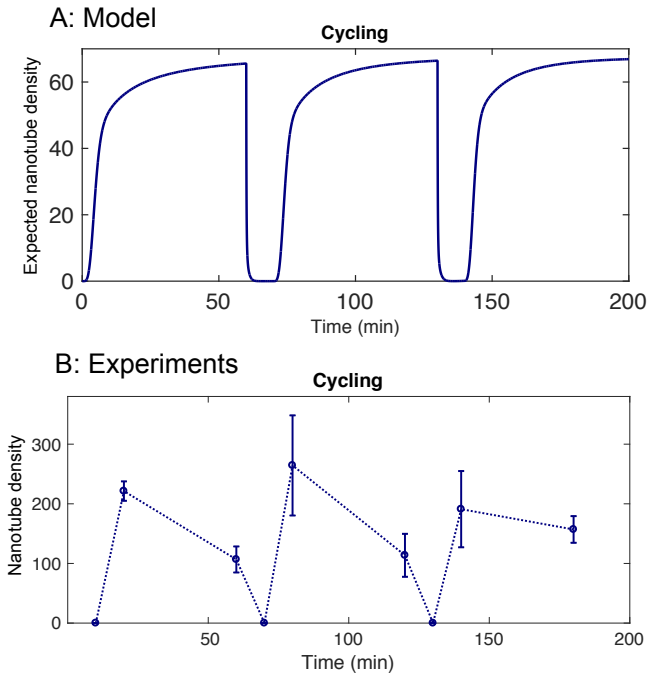

Figure 72: Estimated (A) and experimentally measured (B) nanotube density; sequential invasion/anti-invasion experimental scenario.

5.4.5 Fitted model parameters: Cotranscriptional invasion and RNase H-mediated anti-invasion

We fitted the data shown in Section 4.12, Figs. 41 and 42, where we used nanotubes assembling from the 8 nucleotide-long sticky end tile variant (Fig. 1 C), which are stable in the presence of RNAP at 37° C. The nanotube nucleation, polymerization, depolymerization, joining, and fragmentation rates are generally similar to those of nanotubes assembled from 5 nucleotide-long tiles (Table 11) discussed in the previous section. A notable difference is a significantly lower depolymerization rate, as well as lower invasion rate (binding of RNA invaders to tiles and nanotubes).

Figure 73 shows plots of the cumulative distribution fits, concentration of important components (total, free, and inactive tile concentration, concentration of nuclei, invader and anti-invader), histogram fits, and mean length compared to the data. We estimate the nanotube density in a 100 μm $\times$ 100 μm area in Fig. 74, which was computed as described in the previous section. The number of nanotubes is generally in the same order or magnitude as our experimental observations. However it appears that our estimate does not capture well the decrease of nanotube density over time that is attributed to end-joining [4].

Table 12: Parameters fitted for model equations (38)–(46)**.** *Parameters were fitted to data shown in Figs. 41 and 42.*

Parameter	Units	L.B.	U.B.	Fitted value	Definition
k_p	$(/M/s)$	10^1	10^7	3.498×10^4	Tube polymerization rate
k_d	$(/s)$	10^{-8}	10^4	7.877×10^{-4}	Tube depolymerization rate
α	$(\mu m/M/s)$	10^4	10^{10}	1.327×10^6	End-joining parameter
k_{break}	$(/s)$	10^{-6}	10^2	4.411×10^{-4}	Fragmentation rate
k_{nucl}	$(/M^{n_{nucl}-1}/s)$	10^{-2}	10^8	7.641×10^2	Nucleation rate
k_{p_0}	$(/M/s)$	10^1	10^7	4.057×10^1	Nuclei polymerization rate
k_{d_0}	$(/s)$	10^{-8}	10^1	1.356×10^{-5}	Nuclei depolymerization rate
n_{nucl}	NA	3	5	3.960	Critical nucleation size
k_i	$(/M/s)$	10^2	10^6	9.957×10^3	Invasion rate of tiles
k_{iL0}	$(/M/s)$	10^2	10^6	6.961×10^2	Invasion rate of nuclei
k_{iL}	$(/M/s)$	10^2	10^6	8.226×10^3	Invasion rate of nanotubes
$k_{cat,a}$	$(/s)$	0	0.2	0.1786	k_{cat} of RNase H
$k_{cat,ON}$	$(/s)$	0	5	0.1779	k_{cat} of RNAP (Genelet ON)
$k_{cat,OFF}$	$(/s)$	0	0.2	0.03392	k_{cat} of RNAP (Genelet OFF)
KM_a	(nM)	10	500	28.98	Michaelis constant for RNase H
KM_{ON}	(nM)	10	500	246.2	Michaelis constant for RNAP (Genelet ON)
KM_{OFF}	(μM)	0.5	3	2.965	Michaelis constant for RNAP (Genelet OFF)

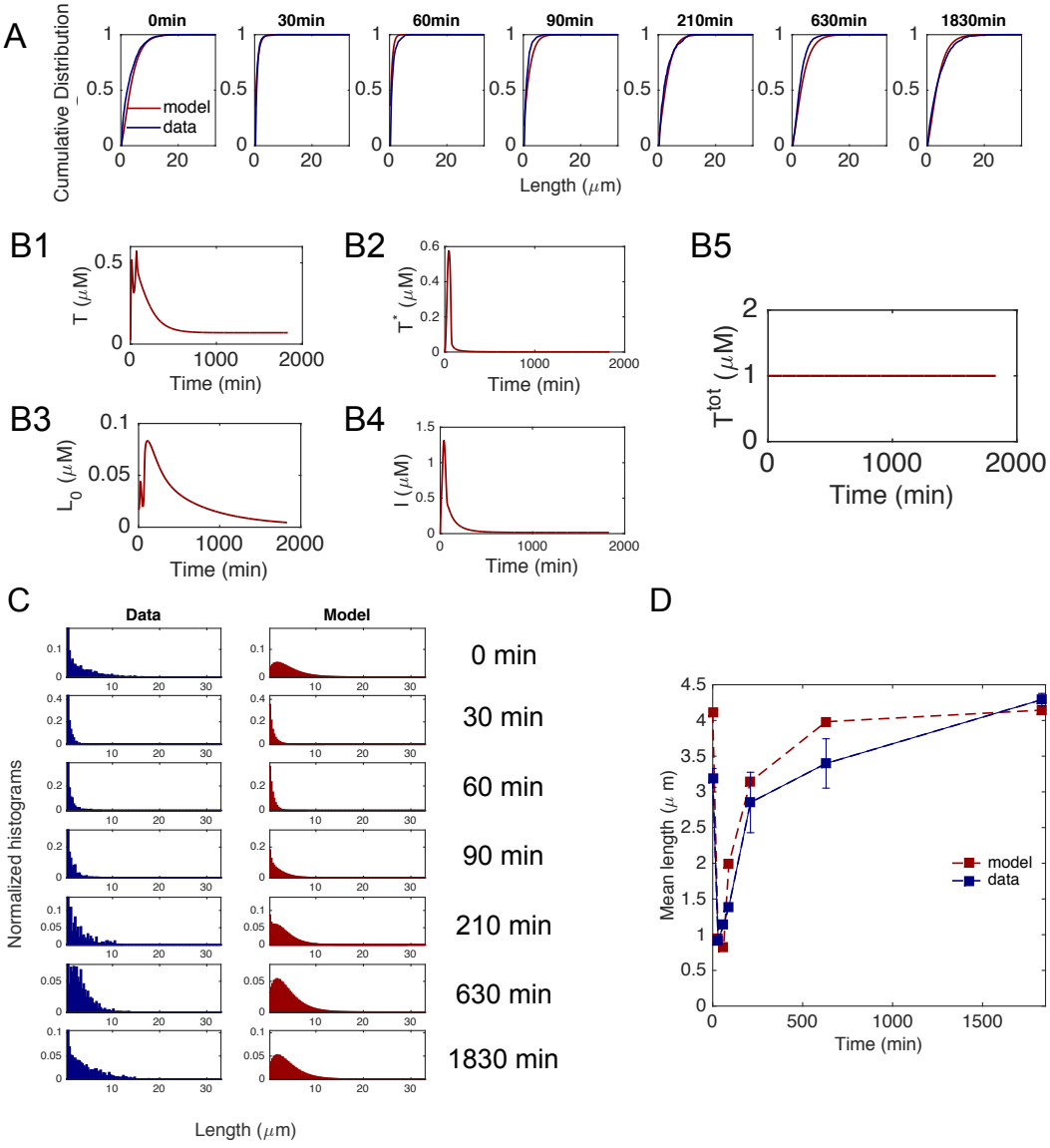

Figure 73: Numerical simulation reproducing the cotranscriptional invasion and RNase H-based anti-invasion experiments. *A: Comparison between representative experimental (blue) cumulative length distributions gathered during nanotube growth and numerically generated cumulative distribution (red). B1: Time course of free tile concentration. B2: Concentration of inactive tiles. B3: Nuclei concentration. B4: Concentration of free RNA invader. B5: The total tile concentration remains constant. C: Histograms of representative growth experiment (blue) and histograms generated by our model (red). D: Mean and standard deviation of the mean in our nanotube growth experiments, compared with the mean length predicted by our fitted model.*

Table 13: Non-fitted parameters for model equations (38)–(46)**.** *Parameters and estimates for enzyme concentration were determined from [6] (these experiments rely on the same enzyme vendors as in [6]).*

Parameter	Units	Value	Definition
T_G^{tot}	(nM)	87.5	Total gene concentration
$I_{G\|t=0}$	(nM)	150	Initial concentration of gene's inhibitor
$A_{G\|t=0}$	(nM)	125	Initial concentration of gene's activator
$[RNAP]^{tot}$	(μM)	$0.125 = \frac{1.25\times 7\mu L}{70\mu L}$	Total concentration of RNAP
$[RNaseH]^{tot}$	(μM)	$0.025 = \frac{1.25\times 1.4\mu L}{70\mu L}$	Total concentration of RNaseH
k_{TA}	$(/M/s)$	1.63×10^4	Gene activation rate
k_{TI}	$(/M/s)$	4.858×10^3	Gene inhibition rate
k_{AI}	$(/M/s)$	7.832×10^3	Binding rate of gene activator and inhibitor

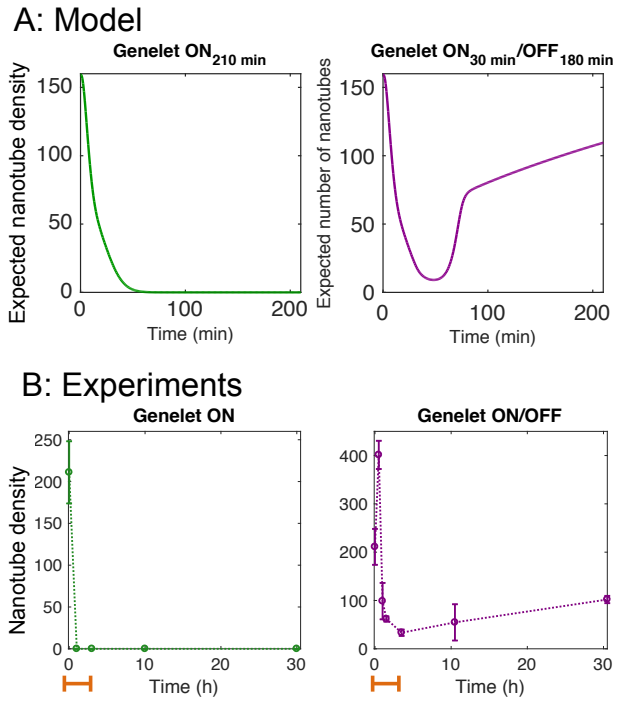

Figure 74: Estimated (A) and experimentally measured (B) nanotube density: cotranscriptional invasion and RNase H anti-invasion numerical simulations. *The simulation was done for 200 minutes, while we report data for the entire time measurements were taken (orange brackets indicate the simulated interval in (A)).*

5.5 Modeling the synthetic transcriptional oscillator

For the readers' convenience, we report the derivation of the ODE model for the transcriptional oscillator [11, 6, 25] and we describe how the model parameters were fitted to experimental data.

5.5.1 Model derivation

A detailed model for DNA and RNA hybridization reactions, branch migration reactions, and Michaelis–Menten enzyme reactions for the two node oscillator is as follows. Figs. 7, 8 and 9 should be used as a support to identify the relevance and role of each reaction.

DNA/RNA hybridization and branch migration reactions

$$
\begin{aligned}
\mathrm{T12} + \mathrm{A2} &\xrightarrow{k_{TA,12}} \mathrm{T12A2} && \text{(Activation)},\\
\mathrm{T21} + \mathrm{A1} &\xrightarrow{k_{TA,21}} \mathrm{T21A1} && \text{(Activation)},\\
\mathrm{A1} + \mathrm{dI1} &\xrightarrow{k_{AI,1}} \mathrm{A1dI1} && \text{(Annihilation)},\\
\mathrm{rA1} + \mathrm{dI1} &\xrightarrow{k_{rAI,1}} \mathrm{rA1dI1} && \text{(Annihilation)},\\
\mathrm{A2} + \mathrm{rI2} &\xrightarrow{k_{AI,2}} \mathrm{A2rI2} && \text{(Annihilation)},\\
\mathrm{T12A2} + \mathrm{rI2} &\xrightarrow{k_{TAI,12}} \mathrm{T12} + \mathrm{A2rI2} && \text{(Inhibition)},\\
\mathrm{T21A1} + \mathrm{dI1} &\xrightarrow{k_{TAI,21}} \mathrm{T21} + \mathrm{A1dI1} && \text{(Inhibition)},\\
\mathrm{rA1} + \mathrm{A1dI1} &\xrightarrow{k_{AIrA,1}} \mathrm{rA1dI1} + \mathrm{A1} && \text{(Release)}.
\end{aligned}
$$

Michaelis–Menten enzyme reactions

$$
\begin{aligned}
\mathrm{RNAP} + \mathrm{T12A2} &\underset{k_{-,ON,12}}{\overset{k_{+}}{\rightleftharpoons}} \mathrm{RNAP}\cdot\mathrm{T12A2} \xrightarrow{k_{cat,ON,12}} \mathrm{RNAP} + \mathrm{T12A2} + \mathrm{rA1},\\
\mathrm{RNAP} + \mathrm{T21A1} &\underset{k_{-,ON,21}}{\overset{k_{+}}{\rightleftharpoons}} \mathrm{RNAP}\cdot\mathrm{T21A1} \xrightarrow{k_{cat,ON,21}} \mathrm{RNAP} + \mathrm{T21A1} + \mathrm{rI2},\\
\mathrm{RNAP} + \mathrm{T12} &\underset{k_{-,OFF,12}}{\overset{k_{+}}{\rightleftharpoons}} \mathrm{RNAP}\cdot\mathrm{T12} \xrightarrow{k_{cat,OFF,12}} \mathrm{RNAP} + \mathrm{T12} + \mathrm{rA1},\\
\mathrm{RNAP} + \mathrm{T21} &\underset{k_{-,OFF,21}}{\overset{k_{+}}{\rightleftharpoons}} \mathrm{RNAP}\cdot\mathrm{T21} \xrightarrow{k_{cat,OFF,21}} \mathrm{RNAP} + \mathrm{T21} + \mathrm{rI2},\\
\mathrm{RNaseH} + \mathrm{rA1dI1} &\underset{k_{-,H,1}}{\overset{k_{+,H}}{\rightleftharpoons}} \mathrm{RNaseH}\cdot\mathrm{rA1dI1} \xrightarrow{k_{cat,H,1}} \mathrm{RNaseH} + \mathrm{dI1},\\
\mathrm{RNaseH} + \mathrm{A2rI2} &\underset{k_{-,H,2}}{\overset{k_{+,H}}{\rightleftharpoons}} \mathrm{RNaseH}\cdot\mathrm{A2rI2} \xrightarrow{k_{cat,H,2}} \mathrm{RNaseH} + \mathrm{A2}.
\end{aligned}
$$

Here, we do not consider side-reactions or incomplete production and degradation products. We use the superscript F to indicate template or substrate species not bound to enzymes. Thus, for instance, the total concentrations of ON-state switch is the sum of concentrations of free switch and enzyme-bound switch: $[\mathrm{T}_{ij}\mathrm{A}_j] = [\mathrm{T}_{ij}\mathrm{A}_j^F] + [\mathrm{RNAP}\cdot\mathrm{T}_{ij}\mathrm{A}_j]$. The Michaelis–Menten enzyme reactions are further simplified by the assumption that the concentrations of enzyme-substrate complexes are low compared to total substrate concentrations. Therefore, available enzyme concentrations are calculated in terms

of total enzyme concentrations and substrate concentrations as follows:

$$\begin{aligned}
[\mathrm{RNAP^{tot}}] &= [\mathrm{RNAP}] + \sum_{i,j} \left([\mathrm{RNAP} \cdot \mathrm{T}_{ij}\mathrm{A}_j] + [\mathrm{RNAP} \cdot \mathrm{T}_{ij}] \right), \\
&= [\mathrm{RNAP}] + \sum_{i,j} \left(\frac{[\mathrm{RNAP}][\mathrm{T}_{ij}\mathrm{A}_j^F]}{K_{M,ON,ij}} + \frac{[\mathrm{RNAP}][\mathrm{T}_{ij}^F]}{K_{M,OFF,ij}} \right), \\
&\simeq [\mathrm{RNAP}] + \sum_{i,j} \left(\frac{[\mathrm{RNAP}][\mathrm{T}_{ij}\mathrm{A}_j]}{K_{M,ON,ij}} + \frac{[\mathrm{RNAP}][\mathrm{T}_{ij}]}{K_{M,OFF,ij}} \right), \\
[\mathrm{RNaseH^{tot}}] &= [\mathrm{RNaseH}] + [\mathrm{RNaseH} \cdot \mathrm{rA1dI1}] + [\mathrm{RNaseH} \cdot \mathrm{A2rI2}], \\
&= [\mathrm{RNaseH}] + \frac{[\mathrm{RNaseH}][\mathrm{rA1dI1}^F]}{K_{M,H,1}} + \frac{[\mathrm{RNaseH}][\mathrm{A2rI2}^F]}{K_{M,H,2}}, \\
&\simeq [\mathrm{RNaseH}] + \frac{[\mathrm{RNaseH}][\mathrm{rA1dI1}]}{K_{M,H,1}} + \frac{[\mathrm{RNaseH}][\mathrm{A2rI2}]}{K_{M,H,2}},
\end{aligned}$$

where the superscript tot indicates that all complexes containing that species are considered. The Michaelis constants, the affinity of substrates to the enzymes, are calculated as $K_M = \frac{k_- + k_{cat}}{k_+}$. Thus, we express the available enzyme concentrations as follows:

$$[\mathrm{RNAP}] = \frac{[\mathrm{RNAP^{tot}}]}{1 + \sum_{i,j} \left(\frac{[\mathrm{T}_{ij}\mathrm{A}_j]}{K_{M,ON,ij}} + \frac{[\mathrm{T}_{ij}]}{K_{M,OFF,ij}} \right)}, \qquad [\mathrm{RNaseH}] = \frac{[\mathrm{RNaseH^{tot}}]}{1 + \frac{[\mathrm{rA1dI1}]}{K_{M,H,1}} + \frac{[\mathrm{A2rI2}]}{K_{M,H,2}}}. \tag{48}$$

The approximation used in equation (48) is reasonable for RNase H because a typical reaction mixture contains about 10 nM of RNase H, while its substrate concentrations are hundreds of nM. However, for RNAP, both the enzyme concentration and the switch concentrations are on the order of 100 nM such that the approximation method may not be valid. Thus, we calculate the available RNAP concentrations as follows:

$$\begin{aligned}
[\mathrm{RNAP} \cdot \mathrm{T}_{ij}\mathrm{A}_j] &= \frac{[\mathrm{RNAP}][\mathrm{T}_{ij}\mathrm{A}_j^F]}{K_{M,ON,ij}} = \frac{[\mathrm{RNAP}]([\mathrm{T}_{ij}\mathrm{A}_j] - [\mathrm{RNAP} \cdot \mathrm{T}_{ij}\mathrm{A}_j])}{K_{M,ON,ij}}, \\
[\mathrm{RNAP} \cdot \mathrm{T}_{ij}\mathrm{A}_j] &= \frac{[\mathrm{RNAP}][\mathrm{T}_{ij}\mathrm{A}_j]}{K_{M,ON,ij} + [\mathrm{RNAP}]}.
\end{aligned}$$

Similarly,

$$[\mathrm{RNAP} \cdot \mathrm{T}_{ij}] = \frac{[\mathrm{RNAP}][\mathrm{T}_{ij}]}{K_{M,OFF,ij} + [\mathrm{RNAP}]}.$$

So that

$$\begin{aligned}
[\mathrm{RNAP^{tot}}] &= [\mathrm{RNAP}] + \sum_{i,j} ([\mathrm{RNAP} \cdot \mathrm{T}_{ij}\mathrm{A}_j] + [\mathrm{RNAP} \cdot \mathrm{T}_{ij}]), \qquad (49) \\
&= [\mathrm{RNAP}] \left(1 + \frac{[\mathrm{T21A1}]}{K_{M,ON,21} + [\mathrm{RNAP}]} + \frac{[\mathrm{T12A2}]}{K_{M,ON,12} + [\mathrm{RNAP}]} \right. \\
&\quad \left. + \frac{[\mathrm{T21}]}{K_{M,OFF,21} + [\mathrm{RNAP}]} + \frac{[\mathrm{T12}]}{K_{M,OFF,12} + [\mathrm{RNAP}]} \right).
\end{aligned}$$

The available RNAP concentration in equation (49) was not solved analytically but was estimated numerically by Newton's method (see, for instance, reference [14], where RNA polymerase bound template concentration was solved analytically).

Thus, the dynamics of the two node oscillator is described by the following seven ordinary differential equations:

$$\frac{d[\mathrm{T21}]}{dt} = -k_{TA,21}[\mathrm{T21}][\mathrm{A1}] + k_{TAI,21}[\mathrm{T21A1}][\mathrm{dI1}], \tag{50}$$

$$\frac{d[\mathrm{A1}]}{dt} = -k_{AI,1}[\mathrm{A1}][\mathrm{dI1}] - k_{TA,21}[\mathrm{T21}][\mathrm{A1}] + k_{AIrA,1}[\mathrm{A1dI1}][\mathrm{rA1}], \tag{51}$$

$$\frac{d[\mathrm{dI1}]}{dt} = -k_{AI,1}[\mathrm{A1}][\mathrm{dI1}] - k_{rAI,1}[\mathrm{rA1}][\mathrm{dI1}] - k_{TAI,21}[\mathrm{T21A1}][\mathrm{dI1}] + \\ + \frac{k_{cat,H,1}}{K_{M,H,1}}[\mathrm{RNaseH}][\mathrm{rA1dI1}], \tag{52}$$

$$\frac{d[\mathrm{rA1}]}{dt} = -k_{rAI,1}[\mathrm{rA1}][\mathrm{dI1}] - k_{AIrA,1}[\mathrm{A1dI1}][\mathrm{rA1}] + \\ + \frac{k_{cat,ON,12}}{K_{M,ON,12} + [\mathrm{RNAP}]}[\mathrm{RNAP}][\mathrm{T12A2}] + \frac{k_{cat,OFF,12}}{K_{M,OFF,12} + [\mathrm{RNAP}]}[\mathrm{RNAP}][\mathrm{T12}], \tag{53}$$

$$\frac{d[\mathrm{T12}]}{dt} = -k_{TA,12}[\mathrm{T12}][\mathrm{A2}] + k_{TAI,12}[\mathrm{T12A2}][\mathrm{rI2}], \tag{54}$$

$$\frac{d[\mathrm{A2}]}{dt} = -k_{AI,2}[\mathrm{A2}][\mathrm{rI2}] - k_{TA,12}[\mathrm{T12}][\mathrm{A2}] + \frac{k_{cat,H,2}}{K_{M,H,2}}[\mathrm{RNaseH}][\mathrm{A2rI2}], \tag{55}$$

$$\frac{d[\mathrm{rI2}]}{dt} = -k_{AI,2}[\mathrm{A2}][\mathrm{rI2}] - k_{TAI,12}[\mathrm{T12A2}][\mathrm{rI2}] + \frac{k_{cat,ON,21}}{K_{M,ON,21} + [\mathrm{RNAP}]}[\mathrm{RNAP}][\mathrm{T21A1}] \tag{56}$$

$$+ \frac{k_{cat,OFF,21}}{K_{M,OFF,21} + [\mathrm{RNAP}]}[\mathrm{RNAP}][\mathrm{T21}]. \tag{57}$$

The system preserves the conservation relation, $[\mathrm{T}ij^{\mathrm{tot}}] = [\mathrm{T}ij] + [\mathrm{T}ij\mathrm{A}j]$, and similarly for $[\mathrm{A}j^{\mathrm{tot}}]$ and $[\mathrm{dI1}^{\mathrm{tot}}]$, where again the superscript tot indicates that all species involving the given strands are being counted. Using these conserved quantities, the remaining variables, [T21A1], [A1dI1], [rA1dI1], [T12A2] and [A2rI2], are directly calculated from the concentrations of other species.

Extended oscillator model The detailed model (50)–(55) is useful to develop the modeling framework and to search for desirable conditions within the parameter space, however two shortcomings were apparent after experimental observation of oscillator behavior [11, 6, 25]. First, the mean level of RNA concentrations kept increasing after each oscillation cycle in the gel measurements, while this phenomenon is not observed in the detailed model for a wide variety of parameter choices. Second, the experiments revealed an almost linear build-up of short degradation products, while the detailed model has no mechanism to produce short degradation products at all. To explain the experimental observation that the amount of RNA inhibitor in the oscillator increased after each cycle and that the short RNA products build up over time, we developed an extended model where an incomplete degradation product is included in the reaction dynamics. These sets of extended model equations were used to generate simulation results in the main text as well as in the supplementary information. We propose that the consideration of incomplete degradation products can potentially explain both the slowdown of oscillation frequency and the accumulation of RNA signals. We define an incomplete degradation product sI2 as a 5' partial sequence of rI2 produced upon degradation by RNase H of rI2 in the A2rI2 complex. Due to the binding requirements of RNase H, five to seven bases of the 5' RNA sequence in an RNA-DNA hybrid substrate cannot be degraded [12]. Thus, in our case, several bases of the toehold binding sequence within rI2 cannot be degraded and remain as part of the incomplete degradation product sI2.

Consequently, sI2 can reversibly bind to an activator A2 or an ON-state switch T12A2, and therefore,

we expect that a T12A2sI2 complex can exist. Moreover, a T12A2sI2 complex would not be efficiently inhibited by rI2 because the toehold binding sequence is not accessible. Therefore, we replaced one reaction for RNase H and added four hybridization reactions to the detailed model described earlier:

$$\begin{aligned}
\mathrm{RNaseH} + \mathrm{A2rI2} &\underset{k_{-,H,2}}{\overset{k_{+,H}}{\rightleftharpoons}} \mathrm{RNaseH \cdot A2rI2} \xrightarrow{k_{cat,H,2}} \mathrm{RNaseH} + \mathrm{A2sI2}, \\
\mathrm{A2} + \mathrm{sI2} &\underset{k_{s,-}}{\overset{k_{s,+}}{\rightleftharpoons}} \mathrm{A2sI2}, \\
\mathrm{T12} + \mathrm{A2sI2} &\xrightarrow{k_{TA,12}} \mathrm{T12A2sI2}, \\
\mathrm{T12A2} + \mathrm{sI2} &\underset{k_{s,-}}{\overset{k_{s,+}}{\rightleftharpoons}} \mathrm{T12A2sI2}, \\
\mathrm{rI2} + \mathrm{A2sI2} &\xrightarrow{k_{AI,2}} \mathrm{A2rI2} + \mathrm{sI2},
\end{aligned}$$

where $k_{s,+}$ is the association rate of sI2 to A2 or T12A2, $k_{s,-}$ is the dissociation rate of sI2 in A2sI2 or T12A2sI2 complex. The hybridization reaction between sI2 and A2 (or T12A2 complex) is assumed reversible because the binding site is expected to be short ($\approx$ 8 bases). On the other hand, the hybridization reaction between A2sI2 and T12 (or rI2) is assumed to be identical to that of A2 and T12 (or rI2) and that rI2 can displace sI2 from A2sI2 complex because a large part of A2 sequence is available for binding within A2sI2 complex. We also assume that for the ON-state switch with the incomplete degradation product, the T12A2sI2 complex, the production rate of output rA1 is as fast as that of an unencumbered ON-state switch itself, yet inhibition by rI2 does not take place. This required expanding the equations for switch SW12 to six dimensions as follows:

$$\begin{aligned}
\frac{d[\mathrm{T12}]}{dt} &= -k_{TA,12}[\mathrm{T12}][\mathrm{A2}] + k_{TAI,12}[\mathrm{T12A2}][\mathrm{rI2}] - k_{TA,12}[\mathrm{T12}][\mathrm{A2sI2}], \\
\frac{d[\mathrm{A2}]}{dt} &= -k_{AI,2}[\mathrm{A2}][\mathrm{rI2}] - k_{TA,12}[\mathrm{T12}][\mathrm{A2}] - k_{s,+}[\mathrm{A2}][\mathrm{sI2}] + k_{s,-}[\mathrm{A2sI2}], \\
\frac{d[\mathrm{rI2}]}{dt} &= -k_{AI,2}[\mathrm{A2}][\mathrm{rI2}] - k_{AI,2}[\mathrm{A2sI2}][\mathrm{rI2}] - k_{TAI,12}[\mathrm{T12A2}][\mathrm{rI2}] \\
&\quad + \frac{k_{cat,ON,21}}{K_{M,ON,21} + [\mathrm{RNAP}]}[\mathrm{RNAP}][\mathrm{T21A1}] + \frac{k_{cat,OFF,21}}{K_{M,OFF,21} + [\mathrm{RNAP}]}[\mathrm{RNAP}][\mathrm{T21}], \\
\frac{d[\mathrm{sI2}]}{dt} &= -k_{s,+}[\mathrm{A2}][\mathrm{sI2}] + k_{s,-}[\mathrm{A2sI2}] + k_{AI,2}[\mathrm{A2sI2}][\mathrm{rI2}] - k_{s,+}[\mathrm{T12A2}][\mathrm{sI2}] \\
&\quad + k_{s,-}[\mathrm{T12A2sI2}], \\
\frac{d[\mathrm{A2sI2}]}{dt} &= k_{s,+}[\mathrm{A2}][\mathrm{sI2}] - k_{s,-}[\mathrm{A2sI2}] - k_{AI,2}[\mathrm{A2sI2}][\mathrm{rI2}] - k_{TA,12}[\mathrm{T12}][\mathrm{A2sI2}] \\
&\quad + \frac{k_{cat,H,2}}{K_{M,H,2}}[\mathrm{RNaseH}][\mathrm{A2rI2}], \\
\frac{d[\mathrm{T12A2sI2}]}{dt} &= k_{s,+}[\mathrm{T12A2}][\mathrm{sI2}] - k_{s,-}[\mathrm{T12A2sI2}] + k_{TA,12}[\mathrm{T12}][\mathrm{A2sI2}].
\end{aligned}$$

The remaining variables for switch SW12, [T12A2] and [A2rI2], are calculated from the conservation relation. Furthermore, RNA activator rA1 is transcribed from T12A2sI2 in addition to T12A2 and T12:

$$\begin{aligned}
\frac{d[\mathrm{rA1}]}{dt} &= -k_{rAI,1}[\mathrm{rA1}][\mathrm{dI1}] - k_{AIrA,1}[\mathrm{A1dI1}][\mathrm{rA1}] + \\
&+ \frac{k_{cat,ON,12}}{K_{M,ON,12} + [\mathrm{RNAP}]}[\mathrm{RNAP}]\left([\mathrm{T12A2}] + [\mathrm{T12A2sI2}]\right) + \frac{k_{cat,OFF,12}}{K_{M,OFF,12} + [\mathrm{RNAP}]}[\mathrm{RNAP}][\mathrm{T12}].
\end{aligned}$$

The remaining variables for switch SW21 do not need adjustments after the introduction of sI2. Interestingly, the toehold-binding sequence of rA1 lies close to its 3' end where degradation of RNA can be complete. It is possible that the lack of interfering signal (short rA1 that binds to the toehold sequence) may keep the excitatory connection effective with a small amount of RNA activator rA1 throughout the reaction, although further experimental verification would be required.

5.6 Modeling the oscillator directing nanotube assembly and disassembly.

We modeled the dynamics of the oscillator directing disassembly and reassembly of the nanotubes by interconnecting and simultaneously integrating the ODEs described in the previous sections.

The extended oscillator model is augmented with a new template strand TIns, which produces RNA invader, and with the ODEs describing the dynamics of active and inactive tiles (equations (38) and (42)), nuclei (equation (39)), and nanotubes (equations (40)–(41)) in the different length bins. Four new reactions are needed for TIns, with 3 new binding rate constants and 6 new enzyme constants (since for each enzyme we use only K_M and k_{cat}).

Additional hybridization and branch migration reactions

$$\begin{aligned}
\mathrm{TIns} + \mathrm{A1} &\xrightarrow{k_{TA,Ins}} \mathrm{TInsA1} && \text{(Activation)},\\
\mathrm{TInsA1} + \mathrm{dI1} &\xrightarrow{k_{TAI,Ins}} \mathrm{TIns} + \mathrm{A1dI1} && \text{(Inhibition)},\\
\mathrm{Tile} + \mathrm{Inv} &\xrightarrow{k_{Tile}} \mathrm{TileInv} && \text{(Invasion)},
\end{aligned}$$

Additional enzyme reactions

$$\begin{aligned}
\mathrm{RNAP} + \mathrm{TInsA1} &\underset{k_{-,ON,Ins}}{\overset{k_{+}}{\rightleftharpoons}} \mathrm{RNAP}\cdot\mathrm{TInsA1} \xrightarrow{k_{cat,ON,Ins}} \mathrm{RNAP} + \mathrm{TInsA1} + \mathrm{Inv}\\
\mathrm{RNAP} + \mathrm{TIns} &\underset{k_{-,OFF,Ins}}{\overset{k_{+}}{\rightleftharpoons}} \mathrm{RNAP}\cdot\mathrm{TIns} \xrightarrow{k_{cat,OFF,Ins}} \mathrm{RNAP} + \mathrm{TIns} + \mathrm{Inv}\\
\mathrm{RNaseH} + \mathrm{TileInv} &\underset{k_{-,H,Tile}}{\overset{k_{+,H}}{\rightleftharpoons}} \mathrm{RNaseH}\cdot\mathrm{TileInv} \xrightarrow{k_{cat,H,Tile}} \mathrm{RNaseH} + \mathrm{Tile}
\end{aligned}$$

Thus, the dynamics of the oscillator with the DNA nanotubes can be described by ten ordinary differential equations where differential equations for the new species [TIns], [Tile], and [Inv] are added and appropriate adjustments for the differential equations for [A1] and [dI1] are made as follows:

$$\begin{aligned}
\frac{d[\mathrm{TIns}]}{dt} &= -k_{TA,Ins}[\mathrm{TIns}][\mathrm{A1}] + k_{TAI,Ins}[\mathrm{TInsA1}][\mathrm{dI1}],\\
\frac{d[\mathrm{Tile}]}{dt} &= -k_{Tile}[\mathrm{Tile}][\mathrm{Inv}] + \frac{k_{cat,H,Tile}}{K_{M,H,Tile}}[\mathrm{RNaseH}][\mathrm{TileInv}],\\
\frac{d[\mathrm{Inv}]}{dt} &= -k_{Tile}[\mathrm{Tile}][\mathrm{Inv}] + \frac{k_{cat,ON,Ins}}{K_{M,ON,Ins} + [\mathrm{RNAP}]}[\mathrm{RNAP}][\mathrm{TInsA1}]\\
&\quad + \frac{k_{cat,OFF,Ins}}{K_{M,OFF,Ins} + [\mathrm{RNAP}]}[\mathrm{RNAP}][\mathrm{TIns}],\\
\frac{d[\mathrm{A1}]}{dt} &= -k_{AI,1}[\mathrm{A1}][\mathrm{dI1}] - k_{TA,21}[\mathrm{T21}][\mathrm{A1}] - k_{TA,Ins}[\mathrm{TIns}][\mathrm{A1}] + k_{AIrA,1}[\mathrm{A1dI1}][\mathrm{rA1}],\\
\frac{d[\mathrm{dI1}]}{dt} &= -k_{AI,1}[\mathrm{A1}][\mathrm{dI1}] - k_{rAI,1}[\mathrm{rA1}][\mathrm{dI1}] - k_{TAI,21}[\mathrm{T21A1}][\mathrm{dI1}] - k_{TAI,Ins}[\mathrm{TInsA1}][\mathrm{dI1}]\\
&\quad + \frac{k_{cat,H,1}}{K_{M,H,1}}[\mathrm{RNaseH}][\mathrm{rA1dI1}].
\end{aligned}$$

The calculation of available RNAP concentration is adjusted as follows:

$$[\mathrm{RNAP^{tot}}] = [\mathrm{RNAP}]\left(1 + \frac{[\mathrm{T21A1}]}{K_{M,ON,21} + [\mathrm{RNAP}]} + \frac{[\mathrm{T12A2}] + [\mathrm{T12A2sI2}]}{K_{M,ON,12} + [\mathrm{RNAP}]} + \frac{[\mathrm{TInsA1}]}{K_{M,ON,Ins} + [\mathrm{RNAP}]} + \right.$$
$$\left. + \frac{[\mathrm{T21}]}{K_{M,OFF,21} + [\mathrm{RNAP}]} + \frac{[\mathrm{T12}]}{K_{M,OFF,12} + [\mathrm{RNAP}]} + \frac{[\mathrm{TIns}]}{K_{M,OFF,Ins} + [\mathrm{RNAP}]} + \frac{[\mathrm{Tile}] + [\mathrm{TileInv}]}{K_{M,Tile} + [\mathrm{RNAP}]}\right).$$

The Michaelis constants of switch SWIns are expected to be similar to those of switch SW21 due to their identical promoter structures. However, hybridization kinetics of switch SWIns was not assumed to be identical to that of SW21. Here, we also assumed that the active and inactive tile species can interact with RNAP weakly. The differential equations of [T21], [T12], [A2], and [rI2] do not need adjustments after the introduction of new species. As before, [T21A1], [A1dI1], [rA1dI1], [TInsA1], [T12A2], [A2rI2], and [TileInv] are calculated from the conservation relation.

5.6.1 Oscillator model fitting

The kinetic simulations and parameter fittings were implemented in MATLAB. Differential equations were solved using the *ode23s* function, while the cost function of model fits on experimental data was minimized using the *fmincon* function. We settled on a cost function using least-squared errors of experimental fluorescence trajectories of oscillator experiments and switch states in simulation. For parameter estimation related to tile species, we asserted that the free tile species concentration ([Tile]) approaches 500 nM for the first peak of oscillator traces that used 1000 nM total tile concentration and 65 or 70 nM insulators (Sections 4.13.1 and 4.13.2) based on the simulation results in Fig. 73.

During the fit, each parameter was constrained within a plausible range spanning about two orders of magnitude as shown below. For the Experiment series R1, the model was fitted to the oscillator traces of control experiments (uncoupled to nanotubes) reported in Section 4.13.1 and the oscillator traces coupled to nanotubes in Sections 4.13.1, 4.13.1, and 4.13.1. The fitted parameter set is shown in Table 14. For Experiments series R2, the model was fitted to the oscillator traces coupled to nanotubes in Sections 4.13.2 and 4.13.2, using the experimental conditions described therein. The result is shown in Table 15. For Experiments series R3, the model was simultaneously fitted to all oscillator data available, using the experimental conditions described therein. The results are shown in Tables 16. Parameters are generally consistent with those obtained in earlier work, and reproduce well the measurements. We also explored the exponential decay of enzyme activity by including time constants for RNAP and RNaseH enzyme activities as τ_P and τ_H i.e., $[\mathrm{RNAP}]=[\mathrm{RNAP}]_{t=0}\ \exp(-t/\tau_P)$ and $[\mathrm{RNaseH}]=[\mathrm{RNaseH}]_{t=0}\ \exp(-t/\tau_H)$. The fitted time constant τ_P for RNAP activity in Experiment series R2 and R3 traces were on the order of 4 hrs, making it potentially relevant to explain the damping of the oscillators.

Table 14: *Fitted parameters for Experiment series R1.*

Parameters	Lower limit	Upper limit	Value
$K_{M,ON,Ins}$ (nM)	10	316	13.914
$K_{M,ON,12}$ (nM)	10	316	92.085
$K_{M,ON,21}$ (nM)	10	316	124.98
$k_{cat,ON,Ins}$ (/s)	0.01	0.1	0.0522
$k_{cat,ON,12}$ (/s)	0.01	0.1	0.0971
$k_{cat,ON,21}$ (/s)	0.01	0.1	0.0987
$K_{M,OFF,Ins}$ (μM)	0.1	3	2.2531
$K_{M,OFF,12}$ (μM)	0.1	3	0.31959
$K_{M,OFF,21}$ (μM)	0.1	3	0.62593
$k_{cat,OFF,Ins}$ (/s)	0.001	0.03	0.0038
$k_{cat,OFF,12}$ (/s)	0.001	0.03	0.0073
$k_{cat,OFF,21}$ (/s)	0.001	0.03	0.002
$K_{M,H,1}$ (nM)	10	300	18.049
$K_{M,H,2}$ (nM)	10	300	13.878
$K_{M,H,Tile}$ (nM)	10	1000	100.19
$k_{cat,H,1}$ (/s)	0.01	0.3	0.0163
$k_{cat,H,2}$ (/s)	0.01	0.3	0.1567
$k_{cat,H,Tile}$ (/s)	0.01	1	0.994
$K_{M,Tile}$ (μM)	0.1	3	0.746
$k_{AI,1}$ (/M/s)	3×10^3	3×10^5	7.832×10^3
$k_{AI,2}$ (/M/s)	10^3	3×10^5	2.489×10^3
$k_{TA,Ins}$ (/M/s)	3×10^3	3×10^5	1.6299×10^4
$k_{TA,12}$ (/M/s)	3×10^3	3×10^5	4.5316×10^3
$k_{TA,21}$ (/M/s)	3×10^3	3×10^5	3.2137×10^4
$k_{TAI,Ins}$ (/M/s)	3×10^3	3×10^5	4.858×10^3
$k_{TAI,12}$ (/M/s)	3×10^3	3×10^5	3.2981×10^4
$k_{TAI,21}$ (/M/s)	3×10^3	3×10^5	1.3596×10^4
$k_{rAI,1}$ (/M/s)	3×10^3	3×10^5	3.1882×10^4
$k_{AIrA,1}$ (/M/s)	3×10^3	3×10^5	4.1678×10^4
$k_{s,+}$ (/M/s)	3×10^3	3×10^5	4.906×10^4
$k_{s,-}$ (/s)	0.01	1	0.078
k_{Tile} (/M/s)	3×10^3	3×10^5	2.9176×10^5
τ_P (s)	10^4	10^6	8.5696×10^4
τ_H (s)	10^4	10^6	3.2143×10^5

Table 15: *Fitted parameters for Experiment series R2.*

Parameters	Lower limit	Upper limit	Value
$K_{M,ON,Ins}$ (nM)	10	316	10
$K_{M,ON,12}$ (nM)	10	316	70.855
$K_{M,ON,21}$ (nM)	10	316	199.12
$k_{cat,ON,Ins}$ (/s)	0.01	0.1	0.0844
$k_{cat,ON,12}$ (/s)	0.01	0.1	0.0941
$k_{cat,ON,21}$ (/s)	0.01	0.1	0.0408
$K_{M,OFF,Ins}$ (μM)	0.1	3	1.3596
$K_{M,OFF,12}$ (μM)	0.1	3	1.1827
$K_{M,OFF,21}$ (μM)	0.1	3	1.9478
$k_{cat,OFF,Ins}$ (/s)	0.001	0.03	0.0161
$k_{cat,OFF,12}$ (/s)	0.001	0.03	0.0166
$k_{cat,OFF,21}$ (/s)	0.001	0.03	0.0157
$K_{M,H,1}$ (nM)	10	300	18.119
$K_{M,H,2}$ (nM)	10	300	151.06
$K_{M,H,Tile}$ (nM)	10	1000	205.8
$k_{cat,H,1}$ (/s)	0.01	0.3	0.0526
$k_{cat,H,2}$ (/s)	0.01	0.3	0.2638
$k_{cat,H,Tile}$ (/s)	0.01	1	1.2242
$K_{M,Tile}$ (μM)	0.1	3	3.151
$k_{AI,1}$ (/M/s)	3×10^3	3×10^5	7.3488×10^3
$k_{AI,2}$ (/M/s)	10^3	3×10^5	1.7932×10^4
$k_{TA,Ins}$ (/M/s)	3×10^3	3×10^5	1.6748×10^5
$k_{TA,12}$ (/M/s)	3×10^3	3×10^5	3.1624×10^3
$k_{TA,21}$ (/M/s)	3×10^3	3×10^5	1.1336×10^4
$k_{TAI,Ins}$ (/M/s)	3×10^3	3×10^5	1.6748×10^5
$k_{TAI,12}$ (/M/s)	3×10^3	3×10^5	2.8874×10^4
$k_{TAI,21}$ (/M/s)	3×10^3	3×10^5	8.131×10^3
$k_{rAI,1}$ (/M/s)	3×10^3	3×10^5	1.9473×10^4
$k_{AIrA,1}$ (/M/s)	3×10^3	3×10^5	8.5165×10^4
$k_{s,+}$ (/M/s)	3×10^3	3×10^5	2.5166×10^5
$k_{s,-}$ (/s)	0.01	1	0.0359
k_{Tile} (/M/s)	3×10^3	3×10^5	4.3233×10^5
τ_P (s)	10^4	10^6	2.1831×10^4
τ_H (s)	10^4	10^6	3.2201×10^5

Table 16: *Fitted parameters for Experiment series R3.*

Parameters	Lower limit	Upper limit	Value
$K_{M,ON,Ins}$ (nM)	10	316	10
$K_{M,ON,12}$ (nM)	10	316	35.55
$K_{M,ON,21}$ (nM)	10	316	29/13
$k_{cat,ON,Ins}$ (/s)	0.01	0.1	0.089
$k_{cat,ON,12}$ (/s)	0.01	0.1	0.085
$k_{cat,ON,21}$ (/s)	0.01	0.1	0.031
$K_{M,OFF,Ins}$ (μM)	0.1	3	55.14
$K_{M,OFF,12}$ (μM)	0.1	3	24.85
$K_{M,OFF,21}$ (μM)	0.1	3	1.5
$k_{cat,OFF,Ins}$ (/s)	0.001	0.03	0.0023
$k_{cat,OFF,12}$ (/s)	0.001	0.03	0.0085
$k_{cat,OFF,21}$ (/s)	0.001	0.03	0.0071
$K_{M,H,1}$ (nM)	10	300	40.35
$K_{M,H,2}$ (nM)	10	300	103.67
$K_{M,H,Tile}$ (nM)	10	1000	55.33
$k_{cat,H,1}$ (/s)	0.01	0.3	0.0159
$k_{cat,H,2}$ (/s)	0.01	0.3	0.0911
$k_{cat,H,Tile}$ (/s)	0.01	1	0.1087
$K_{M,Tile}$ (μM)	0.1	3	2.24
$k_{AI,1}$ (/M/s)	3×10^3	3×10^5	4.3638×10^3
$k_{AI,2}$ (/M/s)	10^3	3×10^5	4.7848×10^4
$k_{TA,Ins}$ (/M/s)	3×10^3	3×10^5	2.7057×10^5
$k_{TA,12}$ (/M/s)	3×10^3	3×10^5	3.4202×10^4
$k_{TA,21}$ (/M/s)	3×10^3	3×10^5	2.1250×10^4
$k_{TAI,Ins}$ (/M/s)	3×10^3	3×10^5	8.2708×10^3
$k_{TAI,12}$ (/M/s)	3×10^3	3×10^5	8.0071×10^4
$k_{TAI,21}$ (/M/s)	3×10^3	3×10^5	4.6054×10^3
$k_{rAI,1}$ (/M/s)	3×10^3	3×10^5	2.9956×10^4
$k_{AIrA,1}$ (/M/s)	3×10^3	3×10^5	1.8601×10^5
$k_{s,+}$ (/M/s)	3×10^3	3×10^5	1.3553×10^5
$k_{s,-}$ (/s)	0.01	1	0.0667
k_{Tile} (/M/s)	3×10^3	3×10^5	2.0864×10^5
τ_P (s)	10^4	10^6	7.0693×10^4
τ_H (s)	10^4	10^6	2.0395×10^5

5.6.2 Simulating oscillator and nanotube distribution model simultaneously

Approach To numerically reproduce the experiments in which the oscillator is used to direct nanotube assembly (Fig. 5 in the main paper), we composed the models for oscillator and nanotubes derived and fitted in the earlier sections. We used the oscillator fitted parameters shown in Tables 14, 15 and 16. To simulate the evolution of nanotube length distribution, we used the parameters fitted to cotranscriptional invasion and RNase H-mediated anti-invasion obtained in Section 5.4.5, where we replaced the RNAP and RNase H related rates with those obtained in the corresponding one-oscillation and two-oscillation fit (because different lots of enzymes were used in these assays). The simplified tile invasion reaction formulated in the oscillator model for data fitting purposes (driven at rate k_{Tile}) is replaced with the invasion reactions and corresponding rates k_i, k_{iL0}, k_{iL} in Table 12.

As noted in the main text, we observed exceptionally long nanotubes when grown in the presence of oscillator in Experiment rounds R1 and R2; our model was not adjusted to take into account this unusually high growth rate, which is a phenomenon we have not yet been able to elucidate. We conjecture that this may explain the inability of the model fitted in Section 5.4.5 to not accurately reproduce the mean nanotube lenght in oscillator-driven nanotube experiments.

Estimated nanotube density The estimated nanotube density (in a 100 μm $\times$ 100 μm area) in the tile titration and insulator titration experiments is shown in Figs. 75 and 76; the number was estimated as described in Section 5.4.4. The estimated nanotube density is comparable to the measured one. However, the simulations predict much lower nanotube counts than experimental observations. In addition, the model predicts transient and steady state increases in the nanotube population that are not measured in experiments.

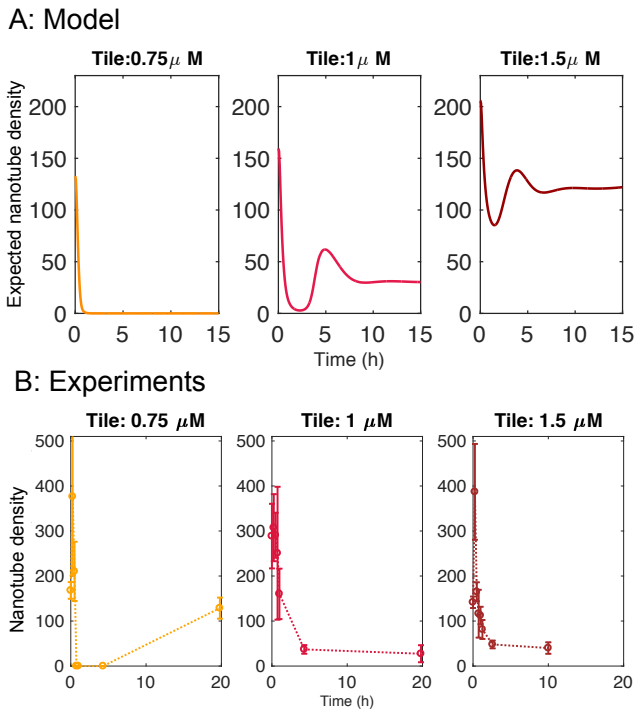

Figure 75: Estimated (A) and experimentally measured (B) number of nanotubes in the oscillator-driven tile titration experiments.

Sensitivity to insulator concentration in Experiment round R3 To capture the experimental behavior observed in Experiment round 3 shown in Fig. 5c and d, in which small changes in the

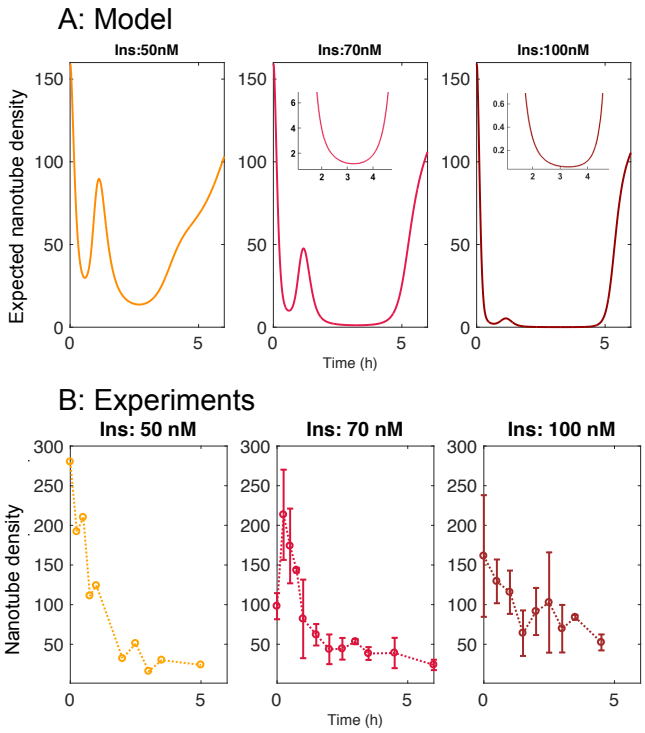

Figure 76: Estimated (A) and experimentally measured (B) number of nanotubes in the oscillator-driven insulator titration experiments. *Insets in (A) show a zoomed-in version of the nanotube number simulation at very low estimated nanotube density.*

insulator concentration (34–40 nM) cause major variation in the nanotube mean length, we introduced a phenomenological sequestration reaction for the RNA invader species. This reaction is meant to simplistically decrease the efficiency of invasion, which is caused by interactions between the insulator and tile toeholds with unknown transcripts produced by RNAP from the nanotubes. ODE (43), that models RNA invader kinetics, was updated as:

$$\frac{dI}{dt}_{new} = \frac{dI}{dt}_{(43)} - \frac{I^h}{KS^h + I^h} \sum_{m=n_{min}}^{m=n_{max}} mL_m. \tag{58}$$

The Hill term was chosen to capture the fact that there is a nonlinear response in the system, and invasion efficiency decreases rapidly near the threshold KS, with steepness that depends on the coefficient h. Further, the invasion efficiency decreases faster when a large number of long nanotubes is present, which is modeled by discounting short nanotubes ($n_{\min} > 1$).

We explored the effects of this sequestration term in a range of h, KS, and n_{min}, and we found that it best reproduces the experimental results when $h = 2$, $KS = 38$ nM, and $n_{min} = 21$. In the absence of this term, the simulated system does not capture the sensitivity with respect to small changes in insulator concentration, as shown in Fig. 77.

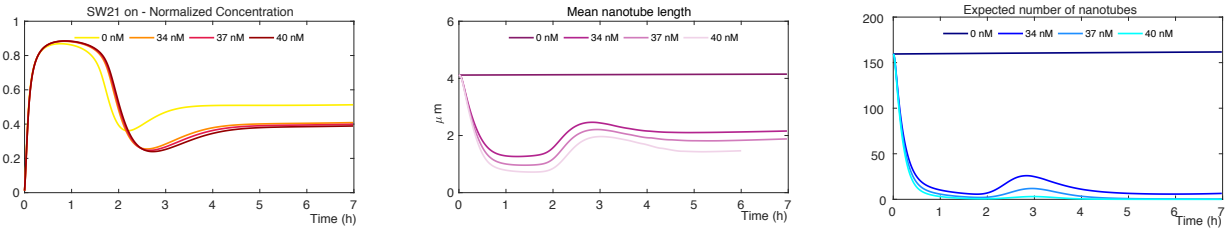

Figure 77: Simulation of molecular oscillator, mean nanotube length, and estimated number of nanotubes in Experiment round 3 without insulator titration without model reaction (58)**.** *This model does not capture the system's sensitivity to small changes in insulator concentration observed in the experiments (Fig. 5c and d of the main paper). By introducing the invader sequestration reaction showed in Equation* (58)*, the model reproduces better the data, as shown in Fig. 6 of the main paper.*

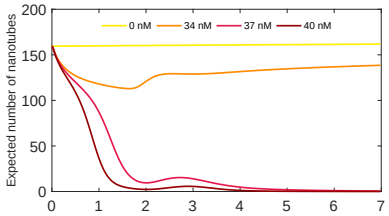

Figure 78: Simulation of estimated number of nanotubes in Experiment round 3 without insulator titration, including reaction (58)**.** *This simulation captures the sensitivity of the system to small changes in insulator concentration. Simulations of oscillator and nanotube mean length are shown Fig. 6 of the manuscript.*

References

[1] Nanoengineer. `https://sourceforge.net/projects/nanoengineer-1/`. Accessed: 2016-11-23.

[2] Robert M Dirks, Milo Lin, Erik Winfree, and Niles A Pierce. Paradigms for computational nucleic acid design. *Nucleic Acids Research*, 32(4):1392–1403, 2004.

[3] Gunther L Eichhorn and Yong Ae Shin. Interaction of metal ions with polynucleotides and related compounds. xii. the relative effect of various metal ions on DNA helicity. *Journal of the American Chemical Society*, 90(26):7323–7328, 1968.

[4] Axel Ekani-Nkodo, Ashish Kumar, and Deborah Kuchnir Fygenson. Joining and scission in the self-assembly of nanotubes from DNA tiles. *Physical review letters*, 93(26):268301, 2004.

[5] Constantine G Evans, Rizal F Hariadi, and Erik Winfree. Direct atomic force microscopy observation of DNA tile crystal growth at the single-molecule level. *Journal of the American Chemical Society*, 134(25):10485–10492, 2012.

[6] Elisa Franco, Eike Friedrichs, Jongmin Kim, Ralf Jungmann, Richard Murray, Erik Winfree, and Friedrich C Simmel. Timing molecular motion and production with a synthetic transcriptional clock. *Proceedings of the National Academy of Sciences*, 108(40):E784–E793, 2011.

[7] Rizal F Hariadi, Erik Winfree, and Bernard Yurke. Determining hydrodynamic forces in bursting bubbles using DNA nanotube mechanics. *Proceedings of the National Academy of Sciences*, 112(45):E6086–E6095, 2015.

[8] Rizal F Hariadi, Bernard Yurke, and Erik Winfree. Thermodynamics and kinetics of DNA nanotube polymerization from single-filament measurements. *Chemical Science*, 6(4):2252–2267, 2015.

[9] Jacob N Israelachvili. *Intermolecular and surface forces: revised third edition*. Academic press, 2011.

[10] Jongmin Kim, Kristin S White, and Erik Winfree. Construction of an in vitro bistable circuit from synthetic transcriptional switches. *Molecular systems biology*, 2(1):68, 2006.

[11] Jongmin Kim and Erik Winfree. Synthetic in vitro transcriptional oscillators. *Molecular systems biology*, 7(1):465, 2011.

[12] Walt F Lima and Stanley T Crooke. Cleavage of single strand RNA adjacent to RNA-DNA duplex regions by escherichia coli RNase H1. *Journal of Biological Chemistry*, 272(44):27513–27516, 1997.

[13] Vahid Mardanlou, Kimia C Yaghoubi, Leopold N Green, Hari KK Subramanian, Rizal F Hariadi, Jongmin Kim, and Elisa Franco. A coarse-grained model captures the temporal evolution of DNA nanotube length distributions. *Natural computing*, 17(1):183–199, 2018.

[14] Craig T Martin and Joseph E Coleman. Kinetic analysis of T7 RNA polymerase-promoter interactions with small synthetic promoters. *Biochemistry*, 26(10):2690–2696, 1987.

[15] Abdul M Mohammed and Rebecca Schulman. Directing self-assembly of DNA nanotubes using programmable seeds. *Nano letters*, 13(9):4006–4013, 2013.

[16] Adrien Padirac, Teruo Fujii, and Yannick Rondelez. Quencher-free multiplexed monitoring of DNA reaction circuits. *Nucleic acids research*, 40(15):e118–e118, 2012.

[17] John H Reif, Sudheer Sahu, and Peng Yin. Compact error-resilient computational dna tilings. In *Nanotechnology: science and computation*, pages 79–103. Springer, 2006.

[18] J Rizzo, L K Gifford, X Zhang, A M Gewirtz, and P Lu. Chimeric RNA-DNA molecular beacon assay for ribonuclease H activity. *Molecular and Cellular Probes*, 16:277–283, 2002.

[19] Paul WK Rothemund, Axel Ekani-Nkodo, Nick Papadakis, Ashish Kumar, Deborah Kuchnir Fygenson, and Erik Winfree. Design and characterization of programmable DNA nanotubes. *Journal of the American Chemical Society*, 126(50):16344–16352, 2004.

[20] Samuel W Schaffter, Leopold N Green, Joanna Schneider, Hari K K Subramanian, Rebecca Schulman, and Elisa Franco. T7 RNA polymerase non-specifically transcribes and induces disassembly of DNA nanostructures. *Nucleic Acids Research*, 46(10):5332–5343, 2018.

[21] Rebecca Schulman and Erik Winfree. Synthesis of crystals with a programmable kinetic barrier to nucleation. *Proceedings of the National Academy of Sciences*, 104(39):15236–15241, 2007.

[22] Matthaeus Schwarz-Schilling, Jongmin Kim, Christian Cuba, Maximilian Weitz, Elisa Franco, and Friedrich C Simmel. Building a synthetic transcriptional oscillator. *Cell Cycle Oscillators: Methods and Protocols*, pages 185–199, 2016.

[23] Claus AM Seidel, Andreas Schulz, and Markus HM Sauer. Nucleobase-specific quenching of fluorescent dyes. 1. nucleobase one-electron redox potentials and their correlation with static and dynamic quenching efficiencies. *The Journal of Physical Chemistry*, 100(13):5541–5553, 1996.

[24] David Soloveichik and Erik Winfree. Complexity of self-assembled shapes. *SIAM Journal on Computing*, 36(6):1544–1569, 2007.

[25] Maximilian Weitz, Jongmin Kim, Korbinian Kapsner, Erik Winfree, Elisa Franco, and Friedrich C Simmel. Diversity in the dynamical behaviour of a compartmentalized programmable biochemical oscillator. *Nature chemistry*, 6(4):295–302, 2014.

[26] Erik Winfree. Simulations of computing by self-assembly. Technical report, California Institute of Technology, 1998.

[27] Bernard Yurke and Allen P Mills Jr. Using DNA to power nanostructures. *Genetic Programming and Evolvable Machines*, 4(2):111–122, 2003.

[28] J. N. Zadeh, C. D. Steenberg, J. S. Bois, B. R. Wolfe, M. B. Pierce, A. R. Khan, R. M. Dirks, and N. A. Pierce. NUPACK: analysis of nucleic acid systems. *Journal of Computational Chemistry*, 32:170–173, 2011.

[29] David Yu Zhang, Rizal F. Hariadi, Harry M. T. Choi, and Erik Winfree. Integrating DNA strand-displacement circuitry with DNA tile self-assembly. *Nature Communications*, 4, 2013.